

DISS. ETH NO. 16903

**LASER MICROMACHINING: NEW CONCEPT FOR  
FABRICATION OF MICRO-OPTICAL ELEMENTS IN UV  
TRANSPARENT MATERIALS**

A dissertation submitted to the  
**SWISS FEDERAL INSTITUTE OF TECHNOLOGY ZURICH**

for the degree of  
Doctor of Natural Sciences

presented by  
**Giedrius Kopitkovas**

Master of Physics, Vilnius University, Vilnius  
born 07.04.1977  
citizen of Lithuania

accepted on the recommendation of

Prof./PD A. Wokaun, examiner

Prof./PD D. Günther, co-examiner

PD T. Lippert, co-examiner

2006

*Dedicated to my brother and to my family*

**"Das Schönste, was wir erleben können, ist das Geheimnisvolle"**

(Albert Einstein (1879-1955))

(The most beautiful thing what we can express is the most mysterious  
for us.)

(free translation to English)

## Acknowledgment

I wish to acknowledge a number of people who helped me and supported me during my studies and writing of my thesis.

First of all I would like to thank my supervisors PD Dr. Thomas Lippert and Professor Alexander Wokaun for their fruitful discussion, ideas, various help, lectures and financial support.

Many thanks go to Dr. Christian David and Dr. Jens Gobrecht for continuous help during my studies, financial support and for this interesting and successful collaboration between our group and the Laboratory for Micro-and Nanotechnology.

I wish to thank my co-referee Professor Detlef Günther for his corrections and suggestions. My thanks go to the Professor Hiroshi Fukumura and Professor Boris Lukyanchuk for their ideas for theoretical modeling of the temperature jump.

I would like to thank to Dr. Jonathan Hobley who supported me with the idea of the T-jump measurements. It was pleasure to work with him in our laboratory. These studies helped also to understand the LIBWE mechanism and temperature rise and decay processes. I also thank him for examining the Random Phase Plates with a Raman shifted Nd:YAG laser and his suggestions and corrections of my thesis. I wish to say thanks to Dr. Dave Funk who helped me to understand the shock wave phenomenon which occurs in solution after the excitation.

I would like to acknowledge Dr. Mark Hauer who supports me with the surface interference measurements and data evaluation as well as for the first shadowgraphy experiments.

It was a pleasure for me to meet and discuss with Professor Hiroshi Fukumura who also helped me to interpretate the results of the surface interference images.

I am grateful for the discussions about the LIBWE process with Dr. Vass, Dr. Rico Böhme and Dr. Hiroyuki Niino at various conferences. These discussions improved my understandings about the mechanisms of this complex processes that occur in solution during/after the excitation. It was pleasure for me to work together with Dr. Fabio Raimondi, who also supported me with the XPS measurements of quartz samples ablated by LIBWE. The discussions and experimental results helped me to understand the formation of carbon in solution and on the surface sample.

I wish to acknowledge Dr. Volker Deckert and his colleagues for the Infrared Spectroscopy studies on the quartz samples ablated by LIBWE and the fruitful discussions.

I wish to thank Dr. Phil Willmot for his idea about the Random Phase Plate which was successfully fabricated and which is installed in his experimental setup. I wish to send my acknowledge to Dr. Saulius Juodkazis for his measurements of the random phase plate with a femtosecond Ti:Sapphire laser.

I would also like to thank my colleagues for various help. Many thanks go to Stela Canulescu, Lukas Urecht, Sebastian Heiroth, Dr. Macarena Montenegro, Markus Kunhke, Dr. Naoki Murazawa and Dr. Thomas Dumont.

Finally I would like to express my appreciations to my brother and my family who supported me over all the time.

I would like also to thank PSI for the financial support of my studies.

## Table of contents

Acknowledgment.....	4
Table of contents .....	6
Zusammenfassung .....	8
Abstract.....	10
Abbreviations .....	12
1 Introduction .....	13
1.1 A brief history of techniques for fabrication of lenses and micro-optics .....	13
2 Fabrication methods for micro-optical elements.....	15
2.1 Lithography based techniques .....	15
2.2 Laser beam writing .....	18
2.3 Laser assisted etching of UV transparent materials.....	19
3 Laser Induced Backside Wet Etching: Mechanisms and Etching Behavior .....	21
3.1 LIBWE mechanisms: Temperature jump .....	23
3.2 LIBWE mechanisms: Pressure jump .....	43
3.3 LIBWE mechanisms: when etching occurs? .....	58
3.4 Etch rate, etch roughness and incubation effect of quartz by laser assisted wet etching .....	64
3.5 Surface analysis of the etched areas in quartz by LIBWE: study of atomic carbon..	70
3.6 Surface analysis of etched areas in quartz: chemical structural change.....	75
3.7 High fluence range: plasma assisted wet etching? .....	82
3.8 Influence of organic solvents on the LIBWE process. ....	86
3.9 Influence of the excitation wavelength on LIBWE processing .....	90
3.10 Influence of the laser pulse length on LIBWE processing. ....	92
3.11 Dependence of the etch rates and etch roughness on the etch area .....	95
3.12 Etching of different UV transparent materials by LIBWE.....	97
4 Fabrication of micro-optics in quartz .....	101
4.1 Concept of beam shaping with MLA and RPP.....	102
4.2 Fabrication of the Random Phase Plates .....	104
4.3 Fabrication of quartz micro-lens arrays.....	107
4.4 Fabrication of DGTPM.....	111

4.5 Fabrication of micro-lens arrays by LIBWE and DGTPM .....	115
4.6 Micro-lens test: measuring of the focal length .....	121
4.7 Laser beam shaping with Random Phase Plate: results.....	124
4.8 Laser beam shaping with micro-lens arrays: results.....	127
Outlook .....	134
Summary.....	136
References .....	140
Curriculum Vitae .....	146

## Zusammenfassung

In dieser Arbeit wird mit *Laser Induced Backside Wet Etching* eine neue Technik zur präzisen Strukturierung von Quarz und anderen im ultravioletten Spektralbereich transparenten Materialien vorgestellt. Die Methode eignet sich, komplexe dreidimensionale Strukturen, wie zum Beispiel beugende und lichtbrechende Mikrolinsen, Random Phase Plates, lichtbrechende optische Elemente und Beugungsgitter herzustellen. Diese Komponenten sind vielseitig einsetzbar, zum Beispiel in der optischen Telekommunikation, für Abbildungstechniken, Wellenfrontmessungen sowie dem Homogenisieren von Laserstrahlen.

Die bisher existierenden Techniken für die Herstellung von Mikrolinsen aus UV-transparenten Materialien basieren auf mehrstufigen oder langsamen rasternden Prozessen. Ein direkter, in einem Schritt erfolgender Herstellungsprozess für komplexe Strukturen in UV-transparenten Materialien ist daher erstrebenswert. Die wesentliche Zielsetzung dieser Arbeit bestand in der Entwicklung einer Methode, die es erlaubt, binäre lichtbrechende optische Komponenten oder komplexere Elemente (eine Anordnung von Mikro Fresnel und plano-convexen Linsen) in UV-transparenten Materialien (Quarz,  $\text{CaF}_2$ ,  $\text{BaF}_2$ , Saphir) herzustellen. Derartige Elemente könnten z. B. einer Verbesserung der Energieverteilung in Laserstrahlen dienen.

Um qualitativ hochwertige Mikrolinsen herzustellen, ist es notwendig den LIBWE Prozess zu verstehen. Der Materialabtrag während des LIBWE Prozesses basiert auf der Erzeugung starker Temperatur- ( $>2000\text{ }^\circ\text{C}$ ) und Druck- ( $>70\text{ MPa}$ ) Sprünge an der Grenzfläche zwischen dem zu strukturierenden Material und der das Laserlicht absorbierenden Flüssigkeit. Da der tatsächliche Temperaturverlauf nicht experimentell bestimmt werden konnte, wurde ein Modell entwickelt, das den Anstieg und Abfall der Temperatur an der Grenzfläche beschreibt. Die Entwicklung des Druckes wurde experimentell mittels Schlierenfotographie verfolgt. Der LIBWE Mechanismus erweist sich als sehr komplex und wird von einer Vielzahl an Parametern beeinflusst. Als wichtigste experimentelle Parameter sind die Wellenlänge des Lasers, die Konzentration des Absorbers in der Flüssigkeit, die

Energiedichte des Lasers und die ortsabhängige Anzahl an Laserpulsen zu nennen. Ein wichtiger Teil dieser Arbeit bestand daher darin, den LIBWE Prozess zu beschreiben um die optimalen Prozessparameter zu finden, und um den Ätzborgang UV-transparenter Materialien präzise kontrollieren zu können. Die ermittelten Abtragsparameter flossen dann in das Design *Gray Tone Phase Mask* ein, welche ein Schlüsselement in der *ein-Schritt*-Herstellung von Mikrolinsen in UV transparenten Materialien darstellt.

Die DTGPM wird benutzt um die Energieverteilung im einfallenden Laserstrahl in die gewünschte Linsenform zu modulieren. Die Anwendung einer solchen DGTPM im LIBWE Prozess ermöglicht das Herstellen grosser Anordnungen von Mikrolinsen. Die Mikrolinsenanordnungen können benutzt werden um das Strahlprofil von Hochleistungs-Excimer und Nd:YAG Lasern zu homogenisieren.

Alternativ zu den Mikrolinsenanordnungen finden *Random Phase Plates* (RPP) zur Strahlhomogenisierung von Hochleistungslasern Anwendung. Die RPP stellt eine binäre Struktur dar, die aus einer Anzahl zufällig und schachbrettförmig verteilter Quadrate besteht. Im Vergleich zu den Mikrolinsen sind die RPP relativ einfach aufgebaut und können mittels LIBWE direkt, d. h. ohne DGTPM erzeugt werden.

Beide Strukturen, RPP und Mikrolinsenanordnungen, führen zu einer deutlichen Verbesserung des Laserintensitätsprofils. Die RPP besitzt Vorteile in Form der einfachen Herstellung und Anwendbarkeit, sie ist jedoch lediglich für eine einzelne Laserwellenlänge ausgelegt. Die Herstellung von Mikrolinsenanordnungen ist komplexer. Sie können hingegen über einen breiten Wellenlängenbereich eingesetzt werden. Der Durchmesser des mittels RPP homogenisierten Laserstrahls ist stets kleiner als 1 mm, während der mittels Mikrolinsenanordnungen homogenisierte Strahl kontinuierlich von wenigen mm bis zu einigen Zentimetern variiert werden kann.

Mikrolinsenanordnungen und Random Phase Plates stellen die bisher anspruchvollsten Strukturen dar, die durch Anwendung des LIBWE Prozesses erzeugt wurden.



## Abstract

In this work a new technique for precise structuring of quartz and other UV transparent material is presented. The process is known as *Laser Induced Backside Wet Etching* and can be utilized to fabricate complex three dimensional structures, such as diffractive and refractive micro-lenses, random phase plates, diffractive optical elements and diffractive gratings in quartz and in other UV transparent materials. These components can be widely applied in optical telecommunications, imaging, wavefront measurements, and beam homogenizing, etc.

The existing technologies for fabrication of micro-lenses in UV transparent materials are based on a multistep approach or on a slow scanning process. It is therefore advantageous to create a technique for a *one step* fabrication of complex structures in UV transparent materials. The main goal of this project was to develop a technique which allows us to fabricate binary diffractive optical components and more complex elements, such as arrays of micro Fresnel and plano-convex lenses in different UV transparent materials (quartz,  $\text{CaF}_2$ ,  $\text{BaF}_2$ , sapphire) with a one process step. These elements must for example be applicable for example in the improvement of a laser beam profile.

In order to produce high quality micro-lenses in UV transparent materials it is necessary to understand the LIBWE process. The etching of the material by LIBWE is based on the generation of high temperature ( $>2000\text{ }^\circ\text{C}$ ) and high pressure ( $>70\text{ MPa}$ ) jumps at the interface between the quartz and the liquid, which absorbs the laser light. The actual temperature jump could not be measured experimentally, therefore a theoretical model was created to evaluate the temperature rise and decay at the interface between the material and liquid. The pressure jump was evaluated from the experimentally obtained shadowgraphy images. The mechanism of LIBWE is very complex and depends on many different parameters such as the laser excitation wavelength, the concentration of absorber in the solution, the laser energy density (fluence) and the number of applied laser pulses. Therefore a lot of attention in this work was paid to describe the LIBWE process and to define the parameters with which the etching of UV transparent materials will be precise, smooth and controllable. The etching parameters are included in the design of the *Diffractive Gray Tone Phase Mask*, which is a key element in *one step* fabrication of

micro-lenses in UV transparent materials. The DGTPM is used for modulating the incoming laser beam intensity into the desired lens shape. The combination of LIBWE and the projection of a DGTPM allows us to fabricate arrays of diffractive and refractive micro-lenses in quartz, which can be applied as beam homogenizers for high power excimers and Nd:YAG lasers.

An alternative beam homogenizer for high power lasers is the Random Phase Plate. The RPP is a binary structure, which consists of a number of randomly tessellating squares. The RPP is much more simple compared to micro-lens arrays and can be fabricated directly by LIBWE and requires no DGTPM.

Both RPP and micro-lens array beam homogenizers deliver clear improvements in the laser intensity profile. The RPP is simple to use and it is easy to fabricate, while fabrication of micro-lenses are more complex. However, an RPP is only suitable for a single designed laser wavelength, while micro-lenses can be used over a broad wavelength range. The diameter of the homogenized beam obtained with an RPP is less than 1 mm, while diameter of the homogenized laser beam with micro-lens arrays can be continuously varied from several mm up to centimeters.

The fabrication of micro-lenses and Random Phase Plates is up to now a *highlight* of the application of the LIBWE process.

## Abbreviations

ATR	Attenuated Total Reflection
CAD	Computer aided design
CCD	Charge coupled device
DGTPM	Diffractive Gray Tone Phase Mask
DC	Duty cycle
e-beam	electron beam
FTIR	Fourier Transformed Infrared Spectroscopy
ISR	Intersystem crossing
IR	Infrared (e.g. light or radiation)
LASER	Light amplification by stimulated emission of radiation
LIBWE	Laser Induced Backside Wet Etching
MLA	Micro-lens array
PVDF	Poly vinylidene fluoride
P-jump	Pressure jump
PMMA	Poly methylmethacrylate
RIE	Reactive Ion Etching
RMS	root-mean square
RPP	Random Phase Plate
SEM	Scanning Electron Microscope
THF	Tetrahydrofurane
T-jump	Temperature jump
QMB	Quartz microbalance
VIS	visible (e.g. radiation)
VUV	Vacuum Ultraviolet
UV	Ultraviolet (e.g. radiation)
XPS	X-ray Photoelectron Spectroscop

## 1 Introduction

Let us go back in history and look briefly on the most important developments in technologies for the fabrication of conventional lenses and micro-lenses in band gap materials (glass, quartz and others).

### *1.1 A brief history of techniques for fabrication of lenses and micro-optics*

The earliest written records of lenses date to Ancient Greece (424 BC) and mention a convex lens used to focus the sun's light to produce fire. Ancient writings also show that burning glasses were known by the Romans almost 2000 years ago [1]. The Romans were first to use lenses for correcting eyesight. The Arabian mathematician Abu Ali Ibn al-Haitham experimentally investigated the magnification of images using lenses, as well as reflection and refraction phenomenon of the light [2, 3]. He also gave a first accurate explanation of vision and describes how the lens forms the image on the retina. A number of theoretical and experimental investigations of light and the applications of lenses were made in 16<sup>th</sup> – 18<sup>th</sup> centuries. The most important applications of lenses were made by Galileo Galilei (in 1609) and Johannes Kepler (in 1611). They built the telescopes and described the principles of microscopes and telescopes. The law of refraction was a milestone for lens development. With it, Decartes derived the shape of a lens that would be needed to correct spherical aberration. In 1647, Cavalieri linked the focal length of a lens to the curvatures of the lens surface and the refractive index in what we now refer to as the lensmaker's formula. Finally, around 1670 Newton derived the imaging equation, a keystone in optical design that relates the focal length of a lens to the distance between it and its object and image plane [4]. The traditional methods for making lenses are grinding and polishing. These approaches have stood for several thousand years already. Grinding is a mechanical process used to remove material. It provides the surface shape as close as possible to the desired lens shape. Polishing is based on mechanical as well chemical processes [3]. By polishing a final surface is obtained with a tolerance of well below the wavelength of light. In the 1970's diamond turning was added to the list of lensmaker's useful tools and was used for the fabrication of "arbitrary" shaped surfaces [1]. Lens fabrication technology quickly changed over the past 20-30 years with the recent

development of the small semiconductor lasers, laser arrays and guiding of laser light into very thin fibers. Thus optical components started to shrink drastically, which lead to the development of new methods for fabricating of small dimension lenses, prisms, mirrors etc. The new era of optics began. Miniaturization of optical components creates a new branch of science which is known as micro-optics, which deals with the design, fabrication and application of micro-optical components, such as refractive and diffractive micro-lenses, micro-mirrors, micro-gratings and micro-prisms. New methods for the fabrication of micro-optics in quartz and other UV transparent materials have been developed, as will be discussed in the following chapter [5].

## 2 Fabrication methods for micro-optical elements

Fabrication of optical components with small dimensions requires a precise machining process and could not be achieved using mechanical grinding and polishing, therefore different technologies were developed for fabrication of micro-optical elements in UV transparent materials.

### 2.1 Lithography based techniques

One of the oldest methods for the fabrication of micro-optics in UV transparent materials is a combination of Lithography and Reactive Ion Etching (RIE) processes. Lithography is a major technology for the fabrication of micro-electronic devices. In the 1970s the planar lithographic process was adapted to the fabrication of micro-lens arrays in semiconductors and quartz.

Lithography is the name of a sequence of processing steps which are applied for the structuring of complex features with continuous profiles in a photoresist spin coated onto a quartz or  $\text{CaF}_2$  substrate [1, 6]. The principles for the fabrication of complex structures in quartz by the combination of mask lithography and Reactive Ion Etching is shown in Figure 1-1.

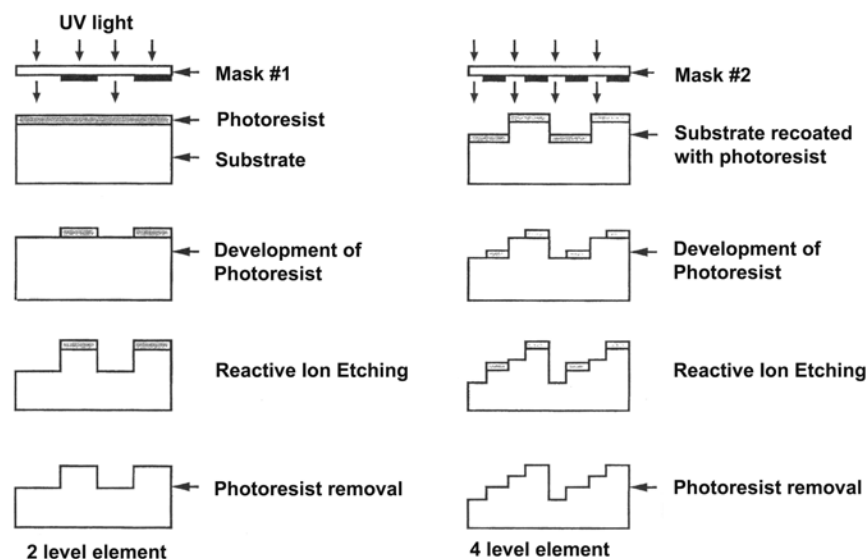


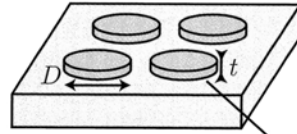
**Fig. 1-1 Fabrication of complex structures in quartz using Mask Lithography and Reactive Ion Etching.**

The first step in this approach is patterning of a phototresist spin-coated onto a substrate, such as quartz by using a chromium mask and Ultraviolet (UV) light. UV light changes the chemical properties of the photoresist in such a way that the areas which are irradiated with the UV light can be chemically removed by using organic solvents. After the development of the photoresist, Reactive Ion Etching is applied in order to transfer features from the polymer into the quartz. An RIE system consists of a small vacuum chamber, into which the substrate is placed. Etch gases, such as  $O_2$  and  $CHF_3$  (for etching quartz) are introduced into the chamber at low pressure (approx. 100 mTorr). A high power radio frequency (RF) discharge results in the generation of a plasma, which contains reactive chemical species from the gasses, that reacts with the substrate.

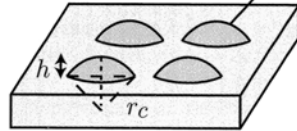
The use of the lithographic process offers a large amount of flexibility in the design of micro-optics. However, due to the large number of repetitive steps, this technique is tedious and slow and therefore is rarely used for large scale production of micro-optics.

The recent development of photoresists and improvements of their characteristics has reduced the number of steps required for the fabrication of micro-lenses in quartz by photolithography and RIE. An industrial process for the fabrication of plano-convex micro-lens arrays in quartz combines photolithography, resist melt-reflow and reactive ion etching techniques [1, 6]. A schematic of this approach is shown in Figure 1-2.

## 1) lithographic fabrication of photoresist cylinders



## 2) reflow: photoresist melting



## 3) reactive ion etching into the substrate



substrate material  
(e.g., glass)

**Fig. 1-2 Fabrication of plano-convex microlens arrays in quartz by the combination of photolithography, resist melt and reflow and Reactive Ion Etching.**

The first step in this technique is the creation of binary cylindrical structures in a photoresist which is coated on a quartz substrate, using photolithography. The two dimensional features on the sample are converted into three dimensional structures by heating the photoresist above the glass transition temperature ( $>200\text{ }^{\circ}\text{C}$ ). This results in a flow of the resist to yield the desired spherically shaped structures. Finally, the micro-lenses are transferred from the photoresist to the quartz by RIE using a proportional etching process. High quality refractive micro-lenses with good spherical shape and low etch roughness can be fabricated in quartz by using this technique [7, 8]. The drawbacks of this technique are that the RIE process is slow (20 nm/min for quartz and 5 nm/min for  $\text{CaF}_2$ ) and the requirements for the high control of the proportional etching and resist characteristics.

These drawbacks have led to the search for alternative techniques for structuring of UV transparent materials.



## 2.2 Laser beam writing

The development of ultrafast and Vacuum Ultraviolet lasers (VUV) offers a new method for direct structuring of quartz [9-18]. These allow a one step micromachining of quartz micro-lenses using sequential *direct* beam writing techniques (as shown in Figure 1-3). This approach has a large flexibility in the fabrication of refractive and diffractive micro-lenses, that are difficult to achieve by a combination of photolithography, resist melt-reflow and RIE.

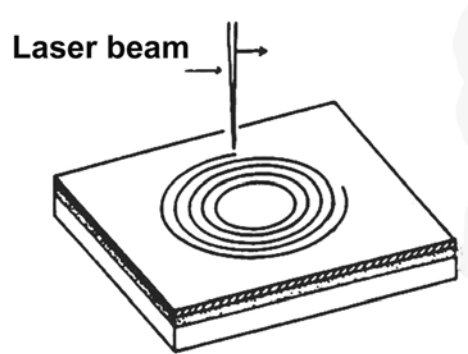


**Fig. 1-3 Laser beam writing setup.**

The mechanism of band gap material ablation with femtosecond lasers is different to nanosecond laser ablation, where thermal processes take place. The peak power density delivered by femtosecond lasers is from 3 to 5 orders of magnitude higher compared to nanosecond laser pulses. The high power density and short femtosecond laser-material interaction time means that multiphoton ionization and plasma formation processes are the key mechanisms in the ablation process [14, 15, 19-21]. Due to the fact that thermal processes are much less pronounced in the femtosecond laser ablation mechanism, the structured areas formed in quartz, using femtosecond lasers, are smooth and without any visible cracks. A very promising application of femtosecond laser beam writing is the three dimensional microstructuring inside UV transparent materials, which can be utilized to create photonic crystals, waveguides, Bragg gratings, etc [16, 22, 23].

Complex structures with sub-micrometer precision can be obtained in quartz by VUV laser ablation, if an F<sub>2</sub> excimer laser (157 nm, 11 ns) is used as the irradiation source [15, 17, 21]. The mechanism of efficient etching of quartz when irradiating with an F<sub>2</sub> excimer laser is still not clear, because the linear absorption coefficient of quartz at this wavelength

is only  $10 \text{ cm}^{-1}$ , which is too low to account for the smooth etching with etch rates of 150 nm per pulse. One explanation for the direct structuring of quartz with VUV lasers may be related to the generation of defects inside a material, which increases the absorption of the laser light. Well defined structures, e.g. submicron gratings can be fabricated by direct VUV laser ablation in quartz [18, 24].

Drawbacks of the direct laser structuring of UV transparent materials by femtosecond or VUV lasers are the high photon costs, the requirement of transparent gases for the beam path (for VUV laser ablation) and the relatively slow sequential scanning process for the fabrication of complex structures.

### ***2.3 Laser assisted etching of UV transparent materials***

Another approach for structuring of UV transparent materials is indirect laser assisted etching using a highly absorbing media, which is in contact with the material. The first application of this approach was the etching of semiconductors materials [25].

Zhang et al. developed a method in which structuring of quartz is assisted by a laser induced plasma [26, 27]. A conventional Nd:YAG laser is applied as an irradiation source, while a metal target, which is in contact with the quartz plate is used as an absorber. The laser light passes through the quartz and is strongly absorbed by the metal target where a plasma is generated. The removal of the quartz is assisted by the generated plasma. Well defined gratings can be prepared in quartz by using this method, however, the depth of the features is limited to  $2 \mu\text{m}$  [26, 27].

The structuring of sapphire and SiC ceramics by the combination of copper vapor laser (510 nm, 10 ns) induced ablation with 0.6 M aqueous  $\text{CrO}_3$  solution which is in contact with the sample was demonstrated by Dolgaev et al [28, 29]. This solution was used to increase the absorption of the laser photons. The key element in the mechanism of the etching process is a temperature jump at the thin sapphire–liquid interface which originates from the strong absorption of the laser light. The rapid temperature increase results in heating of the sapphire substrate and thermal decomposition of the solution, which generates non-soluble  $\text{Cr}_2\text{O}_3$  deposits [29]. These particles form a thin film on the substrate which results in a further increase of the laser induced temperature during the absorption of subsequent laser pulses. The removal of the sapphire is most probably achieved

mechanically, resulting from the difference in the thermal expansion coefficients between the  $\text{Cr}_2\text{O}_3$  film and sapphire substrate. The typical etch rate of sapphire with this method is 200 nm per pulse at a laser fluence of  $5 \text{ J/cm}^2$  [28, 29]. The roughness of the etched features is in the range of several micrometers. The major disadvantage of this method is the high roughness and the deposition of a  $\text{Cr}_2\text{O}_3$  layer on top of the etched features, which has to be removed by an additional cleaning process.

In 1999 Yabe and coworkers developed a method for precise micromachining of UV transparent materials [30, 31]. This technique is similar to the approach of Dolgaev, where an increase of the laser light absorption is achieved through the presence of a strong absorbing organic liquid, which is in contact with the material to be etched. This method has been termed *Laser Induced Backside Wet Etching* and has been applied for the structuring of quartz,  $\text{CaF}_2$ ,  $\text{BaF}_2$ , and sapphire [32-44]. Some of the materials, such as  $\text{CaF}_2$ ,  $\text{BaF}_2$  and sapphire are extremely difficult to machine with other techniques due to the mechanical and chemical properties of these materials. Different excimer lasers, such as ArF, KrF, XeCl, XeF can be used as irradiation sources and a number of organic solutions, such as pyrene in acetone (or THF), aqueous pyranine and naphthalene, pure toluene, and naphthalene in methyl-methacrylate have been tested as “etchants” [32-44]. The lowest etch roughness achieved in quartz using this method is 10 nm, while in the case of  $\text{CaF}_2$ ,  $\text{BaF}_2$  and sapphire the roughness of the etched features is much higher (400 nm) [42, 43, 45].

Another advantage of LIBWE compared to the femtosecond beam writing technique is use of excimer lasers. These lasers provide highly homogeneous irradiation energies (500 mJ/pulse) over large areas (20x15 mm), which makes them very suitable for imaging applications. Fast fabrication of submicron gratings and arrays of square patterns in quartz by LIBWE have been demonstrated by Wang et al. [31, 46]. Another approach for the fabrication of sinusoidal gratings in quartz is the combination of LIBWE with an interference technique, which was demonstrated by Zimmer et al. [43].

A different approach for the fabrication of three dimensional micro-structures with continuous profiles (such as Fresnel type microlenses) in polymers was developed by David et al. [47]. The key element in this process is the use of a *Diffraction Gray Tone Phase Mask* which is applied to modulate the incoming laser beam intensity. This

technique will be described in details in chapter 4. The combination of LIBWE with the projection of a DGTPM opens up a new way to fabricate well defined three dimensional structures, e.g. diffractive and refractive microlens arrays in quartz and in  $\text{BaF}_2$  or  $\text{CaF}_2$ , which can be used as the beam homogenizers (chapter 4).

### **3 Laser Induced Backside Wet Etching: Mechanisms and Etching Behavior**

Three different approaches for the fabrication of micro-optics in UV transparent materials were presented in chapter 2. One of the simplest method for the fabrication of micro-optical components in quartz and other UV transparent materials is a combination of LIBWE and projection of a DGTPM. This approach requires a UV laser and a solution which strongly absorbs the laser irradiation and which is in contact with quartz. The intensity profile of the UV laser, which is modulated by the DGTPM into the designed micro-lens shape, is projected into the interface between the material and liquid, where etching of the material takes place. Using this technique, a micro-lens can be formed in the quartz with a single UV laser pulse! No additional etching steps, such as structuring and development of the photoresist, etching of the material by RIE [1, 6] or complex scanning techniques [22, 23] are necessary in LIBWE. LIBWE can be also utilized for the precise and complex structuring of various UV transparent materials, such as  $\text{CaF}_2$ ,  $\text{BaF}_2$  and sapphire [30, 33, 42], which are difficult to achieve using other industrial methods.

The first goal in these studies is to understand the LIBWE process: what are the key elements in this approach? Only by knowing the mechanism of LIBWE is it possible to apply LIBWE for the fabrication of complex functional optical devices.

The LIBWE process is much more complex as could be seen in early studies. The pioneers and discovers of LIBWE suggested that a key element in LIBWE is an increase in the temperature at the interface between the solution and quartz that is due to the strong absorption and fast relaxation of the excited molecules. This temperature jump melts a quartz layer and results in an explosive evaporation and fast thermal expansion of the solution, which generates expanding and collapsing laser induced bubbles. This latter process creates a pressure jump which removes the molten surface. However, for long time

it was unclear whether it was the pressure jump generated due to the collapse of laser induced bubbles or the shock waves which removed the molten material and at which time scale after the laser pulse the removal of quartz takes place. First answers to these questions are discussed together with experimental results in this chapter.

Three major questions will be discussed in subchapter 3.1: i) the mechanism of light to temperature conversion, ii) modeling of temperature rise and decay, iii) possibilities of indirect measurements of the subsequent temperature decay using the fluorescence of the solution.

The subchapter 3.2 will describe the pressure jump in solution. Several questions in this subchapter will be discussed: i) the mechanism for generation of the pressure jump at the interface between material and solution, ii) an experimental investigation of the pressure jump using the technique of shadowgraphy. In subchapter 3.3 an idea for determining the time delay at which material removal takes place will be discussed.

The application of LIBWE for the fabrication of optical components in UV transparent materials requires a knowledge about the etch rates, which determines how much material can be removed with a single laser pulse. Therefore the etch rate, roughness of the etched features and the number of the pulses required to initiate the etching process were carefully studied. The discussion of experimental results is described in subchapter 3.4. The material for these studies was quartz, selected because of its low cost and high transparency in the UV range. The etching solution, which was also used by the pioneers of LIBWE, [30, 31, 46] was 0.4 M pyrene in acetone. The surface of the quartz that was etched by LIBWE was investigated by *X-Ray Photoelectron Spectroscopy* (XPS), *Raman Microscopy* and a novel technique, named *Fiber Tip Attenuated Total Reflection (ATR)-FTIR Spectroscopy*. The results of these studies clearly suggest that chemical surface modification occurs during the LIBWE process and this will be discussed in detail in the subchapters 3.5-3.6. We could prove that the mechanism of LIBWE strongly depends on the applied fluence range: at the fluences just above the etch threshold the etching starts with a very low etch rate and a very high etch roughness. At the intermediate fluences precise structures with very low etch roughness are observed. At high laser energy densities we observe a strong increase in the etch rates but also an increase of the etch roughness. Further studies (subchapter 3.7) suggest that plasma assisted etching occurs at these fluences.

At the end of subchapter 3.4 the LIBWE mechanism is summarized and the best conditions for structuring quartz with LIBWE by using 0.4 M pyrene in acetone as an etching medium and a XeCl excimer laser as the irradiation source, are defined. But the questions as to whether this etching medium and laser wavelength are the optimum conditions for the fabrication of complex micro-optical elements in quartz with low etch roughness will remain.

The answers to these questions are given in subchapters 3.8-3.11, where experimental studies on the etching parameters using different solutions and different laser wavelength are discussed. Finally, LIBWE has not only been applied for structuring quartz, but also for etching other UV transparent materials, which are chemically and physically different. The etch rates of BaF<sub>2</sub>, CaF<sub>2</sub> and sapphire were investigated experimentally using several etching conditions. The results of these experiments are discussed in subchapter 3.12.

### ***3.1 LIBWE mechanisms: Temperature jump***

Laser Induced Backside Wet Etching starts with the strong absorption of the laser light by a solution containing pyrene dissolved in acetone and which is in contact with the UV transparent material, as shown in Figure 3-1.

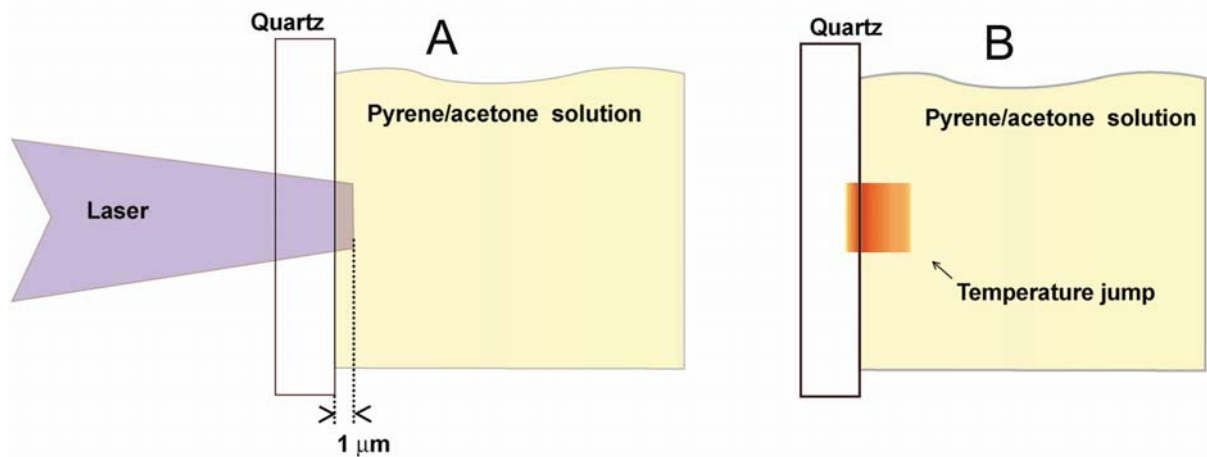


**Fig. 3-1 Absorption of the laser light in solution (A) and the generation of a temperature jump at the quartz-liquid interface (B)**

Quartz *does not absorb* UV laser light. In fact the laser light is absorbed by the pyrene molecules in a very thin  $\leq 1\mu\text{m}$  layer of the liquid. The peak power of the absorbed light in the LIBWE process corresponds to the combined power required to illuminate a 7

kilometer long road! It has already been mentioned that the idea of LIBWE is based on the generation of a high temperature jump at the quartz liquid interface due to the strong absorption and fast relaxation of pyrene molecules, as shown in Figure 1 B.

But how is the light converted to temperature? In order to answer this question it is necessary to understand the photochemical and photothermal processes of pyrene. Many organic molecules are strongly absorbing UV light. Absorption of UV and visible light occurs due to resonance with the bonding and non-bonding electron clouds of a molecule. When the light interacts with the bonding or non-bonding electron cloud the cloud is transformed into a higher energy anti-bonding orbital. This is a transformation from the ground state to the excited state. Light is strongly absorbed if the transition is "allowed" and weakly absorbed if it is "forbidden". An allowed transition is one in which the light can be in high resonance with the electron cloud, meaning that the energy, the symmetry and the spin of the transition all match the corresponding features of the light. For example, light cannot bring about a singlet to triplet transition directly, so we usually see Singlet to Singlet primary photochemical steps. The energy of the transition must match the energy of the photon bringing about the transition. Further, the light must be capable resulting in a change in symmetry associated with the transition.

The absorption coefficient of a material, the reciprocal value of which describes the light penetration depth, is high for allowed transitions. An absorption coefficient of given materials at different radiation wavelength is usually measured with a spectrophotometer. A UV absorption spectrum of a  $c=1.35 \cdot 10^{-5}$  M pyrene solution in methanol is shown in Figure 3-2. This spectrum was obtained with a Cary 5000 UV-VIS spectrophotometer.

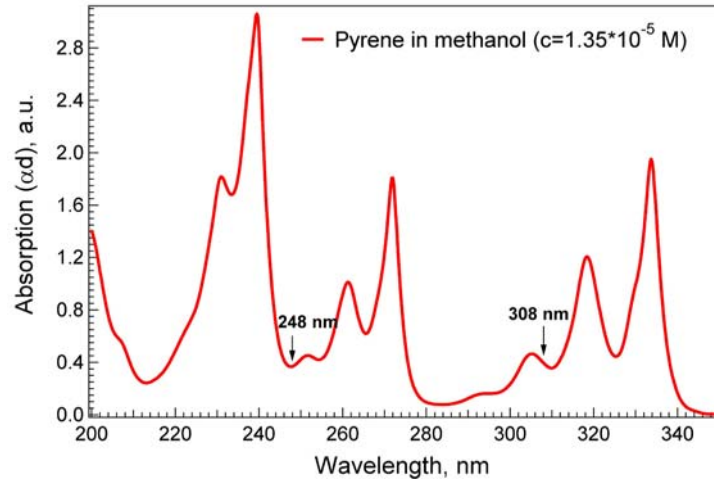


**Fig. 3-2 Absorption spectrum of a  $1.35 \cdot 10^{-5}$  M pyrene solution in methanol.**

The absorption coefficient of 0.4 M pyrene in acetone, which was typically used in this work, can not be measured using the spectrophotometer, due to the fact that in such highly concentrated solutions all of the light is absorbed in the first micrometer of the solution. Therefore the absorption coefficients, at the irradiation wavelengths used (marked as arrow in the Figure 4-2), for highly concentrated pyrene in acetone or THF solutions were evaluated from the lower concentration solution's absorption spectrum (shown in Figure 4-2) using equation 1:

$$\alpha_{highconcentration} = \frac{\alpha_{lowconcentration} \cdot Concentration}{1.35 \cdot 10^{-5}} \quad (1),$$

where  $\alpha_{highconcentration}$  and  $\alpha_{lowconcentration}$  are absorption coefficients [ $\text{cm}^{-1}$ ] of the high concentrated and low concentrated pyrene solutions at the applied irradiation wavelength and the *Concentration* is a concentration of a solution [M].

Two lasers were tested as irradiation sources in our experiments: one was a KrF excimer laser (248 nm) and the second one was a XeCl excimer laser (308 nm). However for most of the experiments, as well as for the fabrication of micro-optical elements in quartz, the 308 nm was chosen due to its good beam quality, high output energy and better working conditions (as will be shown in subchapter 3.9). Therefore, in all later discussion the XeCl excimer laser will be assumed to be the irradiation source. The absorption coefficient for 0.4 M pyrene in acetone solution at the XeCl excimer laser wavelength of 308 nm is  $11680 \text{ cm}^{-1}$ . This means, that the energy of the laser light is absorbed by the first micrometer of



the solution in contact with the quartz interface. Such strong absorption results in a high density of excited pyrene molecules. During and after the end of the laser pulse these excited molecules return to the ground state by losing energy either by emission of the photons (fluorescence) or by non-radiative relaxation. The latter of these mechanisms is one of the key elements in the LIBWE technique, because through this pathway the energy of the excited molecules is converted into heat. Without going into details about the transition of the molecules between the excited states and the ground state (this mechanism will be explained later) and assuming that the energy of all excited molecules is converted to heat, the temperature (T-jump) generated at the quartz liquid interface at an XeCl excimer laser fluence of  $1.5 \text{ J/cm}^2$  can be estimated. The maximum T-jump can be evaluated using equation 2, which was used by Wang et al [30]:

$$T = \frac{\alpha \cdot F}{\rho \cdot C} \quad (2),$$

where  $\alpha$  is absorption coefficient ( $11680 \text{ cm}^{-1}$ ),  $F$  is the laser fluence ( $1.5 \text{ J/cm}^2$ ),  $\rho$  is the density of acetone ( $0.82 \text{ g/cm}^3 @ 293 \text{ K}$ ) and  $C$  is heat capacity of acetone ( $2 \text{ J/(g·K)} @ 293 \text{ K}$ ).

The temperature rise at the quartz-liquid interface evaluated using this equation is  $T=9500 \text{ K}$ ! This value however is much too high, as will be shown later, because this evaluation does not include radiative relaxation of molecules and other energy losses as well as considering the effects of the laser pulse shape. A more sophisticated model for the evaluation of the temperature jump generated by the multiphotonic process of anthracene in polystyrene film was developed by Fukumura et al [48]. The authors claim, that below  $1 \text{ J/cm}^2$  anthracene does not decompose and transforms the light energy into heat. The key mechanism in this process is, according to the authors, a cyclic multiphotonic absorption and radiationless transition between the long living excited states. This idea can be used in theoretical modeling for the evaluation of the temperature rise at the quartz-liquid interface during LIBWE. However, before this can be done, the different excited states and transitions of the excited electrons between these states in pyrene molecule must be discussed.

The pyrene molecule has several electronic states. These are the ground state, the first, second and higher excited singlet and the excited triplet states, as illustrated in Figure 3-3.

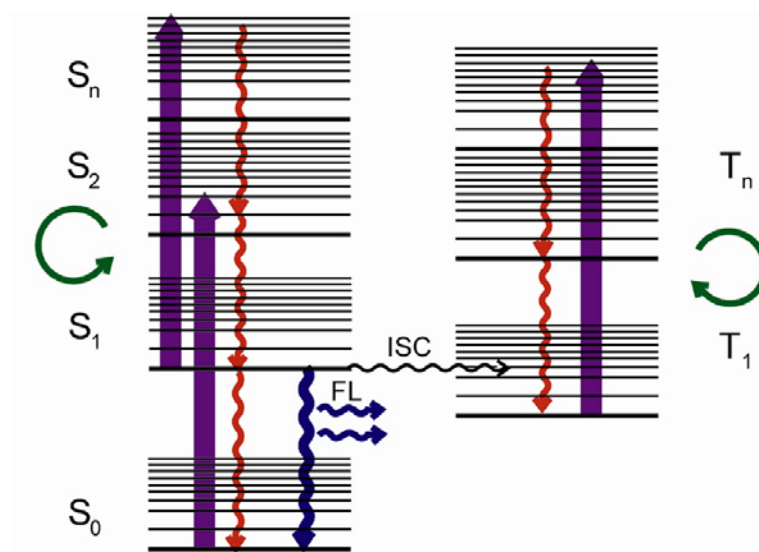


**Fig. 3-3 Diagram of light absorption and transition of the excited pyrene molecule between the states**

The ground state is marked as  $S_0$  (marked in Figure 3-3). The character  $S$  is used for the description of a singlet state, which consists of valence electron pairs with spin-up and spin-down orientation. Excited singlet states named as  $S_1$ ,  $S_2$ ,  $S_n$ , where  $n=3, 4$  and etc. (marked in Figure 3-3) are the states of the electrons, which have been excited from the ground state. These states are energetically higher than the ground state, however, the electronic spin configuration of the electrons is similar to that obtained in the ground state. In addition to the ground and excited singlet states pyrene also has excited triplet states (marked as  $T_1$ ,  $T_n$ , where  $n=2, 3$  and etc. in Figure 3-3) in which all of the unpaired electron's spins are oriented in the same way: either spin up or spin down. These states are found in many other organic molecules, such as anthracene, perylene, acetone, etc [49]. Triplet states ( $T_1$ ) are, in general long living states, which can survive milliseconds or even longer [49], while electron in the excited singlet state  $S_1$  exist for only a few hundred nanoseconds in the case of pyrene and usually for much less time for other organic molecules. Let's first analyze the conversion from light to the temperature in pyrene. During the laser pulse the electrons of the pyrene molecules absorb the UV radiation (marked as thick violet arrow in the Figure 3-3) and undergo a transition to the excited state. There are three major different absorption mechanisms which occur during the XeCl (308 nm) or KrF (248 nm) excimer laser pulses: pyrene molecules can be excited either

from their ground state ( $S_0$ ) to the higher vibrational levels of  $S_2$ , ii) absorption from the first excited singlet state ( $S_1$ ) to the higher excited singlet state ( $S_n$ ), iii) absorption from the first excited triplet state ( $T_1$ ) to the higher excited triplet state ( $T_n$ ). In principle the excitations from  $S_1 \rightarrow S_n$  or  $T_1 \rightarrow T_n$  occur when the states  $S_1$  and  $T_1$  are filled. Absorption of the UV laser light is described by an absorption cross section  $\sigma$ , which specifies a number of photons absorbed per unit area. The ground state absorption cross section  $\sigma_{S_0}$  depends on the linear absorption coefficient and on the concentration of pyrene in solution and can be described by equation 3:

$$\sigma_{S_0} = \frac{\alpha}{c \cdot N_A} \quad (3),$$

where  $\alpha$  is absorption coefficient ( $\alpha=11680 \text{ cm}^{-1}$  @ 308 nm (0.4 M pyrene/acetone)),  $N_A$  is Avogadro's number ( $N_A=6.022 \cdot 10^{23}$  molecules/mol) and  $c$  is pyrene concentration in solution in  $\text{mol/cm}^3$ .

The ground state absorption cross section value for XeCl excimer laser irradiation (308 nm) and 0.4 M pyrene in acetone solution, evaluated using equation 3, is  $4.8 \cdot 10^{-17} \text{ cm}^2$ . This value will be used latter in the evaluation of the conversion from light to the heat. As already mentioned above, the molecules, which absorb laser radiation, undergo a transition from the ground state to the second excited singlet state. But the lifetimes of high excited singlet ( $S_2$ ,  $S_n$ ) states are very short (10 ps) and therefore excited molecules rapidly relax to the first excited singlet state (marked as red arrows in Figure 3-3), which has a lifetime of 30 ns [49, 50]. This relaxation is non-radiative and therefore increases the temperature in the solution. Molecules from the first excited singlet state loose their energy either by emitting photons (this transition is marked as blue arrows in Figure 3-3), or by non-radiative relaxation, which also generates a heat. Emission from the first singlet state is called fluorescence and is marked as *FL* in Figure 3-3. The fluorescence efficiency (ratio between radiative and nonradiative relaxation) in pyrene is 0.6-0.9 and strongly depends on the solvent [51] and concentration. This means that only 10%-40% of the excited molecules from  $S_1$  transfer their energy to heat. In the case of an acetone solution the fluorescence efficiency of the solution is  $\approx 80\%$  [51]. Because of the fact that the first excited triplet state ( $T_1$ ) is energetically lower compared to the first excited singlet state (as shown in Figure 3-3) [49, 50, 52], some of the excited molecules from  $S_1$  are converted

into the metastable long living triplet state  $T_1$ . The transition from  $S_1$  to  $T_1$  is known as intersystem crossing and marked as *ISC* in Figure 3-3. The proposed mechanism of efficient generation of heat in pyrene and other organic molecules, such as anthracene, pyranine, etc. is based on the repeatedly excitation of the molecules from  $S_1$  to  $S_n$  and  $T_1$  to  $T_n$  (marked in Figure 3-3 as violet arrow). The higher excited states  $S_2$ ,  $S_n$ , as mentioned before, and also  $T_n$  have very short lifetimes. Rapid non-radiative relaxation from the  $S_n$  or  $T_n$  to the lower energetic states  $S_1$  or  $T_1$  also produce heat. These transitions are one of the most important transitions for understanding the light to temperature conversion in the LIBWE process and for modeling of temperature jump.

It is also noteworthy to mention, that the above described processes are well studied for "normal" photochemical conditions, with low concentration of pyrene in solution and much lower laser fluences. In our case everything is much more complex, i.e. high concentrations of absorber in solution, with a very pronounced formation of excimers and very high fluences, which may change some features. We also do not take in to account that the solvent and dissolved gasses such as oxygen have an influence on the transition of the excited molecules in the states (e.g. triplet-triplet or singlet-singlet annihilation) and that the model of Fukumura [48] was developed for polymer matrices doped with an absorber where the diffusion and mobility may be different. In spite of all these facts which show that our description is quite simplified the model, which is presented here, is still much further developed than other models which do not consider the photochemical features of pyrene at all.

In order to evaluate the laser induced temperature generated at the quartz -liquid interface during the laser pulse, it is necessary to know the number of molecules which loose their energy by non-radiative transition. Therefore it is necessary to solve a system of population dynamic equations, which describe all possible non-radiative and radiative transitions.

The population dynamics in the ground can be expressed by the following equation (4):

$$\frac{dN_{S_0}(t)}{dt} = -\frac{\sigma_{S_0} \cdot (1 - \Phi_{fluor}) \cdot F(t) \cdot \lambda_{exc}}{h \cdot c \cdot \tau_L} \cdot N_{S_0}(t) + \frac{N_{S_1}(t)}{\tau_S} + \frac{N_{T_1}(t)}{\tau_T} \quad (4),$$

where the first term describes ground state absorption ( $S_0 \rightarrow S_1$  transition), the second and third terms describe relaxation of the excited molecules from the first singlet and triplet states.

Population dynamics in the first excited singlet state can be evaluated by equation 5:

$$\frac{dN_{S_1}(t)}{dt} = -\left(\frac{1}{\tau_S} + \frac{1}{\tau_{isc}} + \frac{\sigma_S \cdot (1 - \Phi_{fluor}) \cdot F(t) \cdot \lambda_{exc}}{h \cdot c \cdot \tau_L}\right) \cdot N_{S_1}(t) + \frac{(N_{S_2}(t) + N_{S_n}(t))}{\tau_{S_n}} \quad (5),$$

where the first term characterizes the transitions  $S_1 \rightarrow S_0$ ,  $S_1 \rightarrow T_1$  and  $S_1 \rightarrow S_2$ , while the second term describes transitions from the higher excited states  $S_2$  and  $S_n$  to  $S_1$ .

The population dynamics in the second and higher excited states can be expressed by the following equations (6, 7):

$$\frac{dN_{S_2}(t)}{dt} = \frac{\sigma_{S_0} \cdot (1 - \Phi_{fluor}) \cdot F(t) \cdot \lambda_{exc}}{h \cdot c \cdot \tau_L} \cdot N_{S_0}(t) - \frac{N_{S_2}(t)}{\tau_{S_n}} \quad (6),$$

$$\frac{dN_{S_n}(t)}{dt} = \frac{\sigma_S \cdot (1 - \Phi_{fluor}) \cdot F(t) \cdot \lambda_{exc}}{h \cdot c \cdot \tau_L} \cdot N_{S_1}(t) - \frac{N_{S_n}(t)}{\tau_{S_n}} \quad (7),$$

where the first term in equation (6) describes the transition between  $S_0$  and  $S_2$  states (ground state absorption), while the first term in the equation (7) describes an absorption from the  $S_1$  to  $S_2$ . The second terms in equations (6) and (7) describe  $S_2 \rightarrow S_1$  and  $S_n \rightarrow S_1$  transitions, respectively.

The population dynamics in the first triplet state  $T_1$  can be expressed by following equation (8):

$$\frac{dN_{T_1}(t)}{dt} = \frac{N_{S_1}(t)}{\tau_{ISC}} - \left(\frac{1}{\tau_T} + \frac{\sigma_T \cdot (1 - \Phi_{fluor}) \cdot F(t) \cdot \lambda_{exc}}{h \cdot c \cdot \tau_L}\right) \cdot N_{T_1}(t) + \frac{N_{T_n}}{\tau_{T_n}} \quad (8),$$

where first term describes intersystem crossing of the singlet molecules, second term expresses losses of triplet molecules due triplet to ground state relaxation and excitation loss of molecules into higher excited triplet state  $T_n$ , and third term describes  $T_n \rightarrow T_1$  relaxation.

Finally, population dynamics in the higher excited triplet state  $T_n$  is expressed by the equation (9):

$$\frac{dN_{T_n}(t)}{dt} = \left(\frac{\sigma_T \cdot (1 - \Phi_{fluor}) \cdot F(t) \cdot \lambda_{exc}}{h \cdot c \cdot \tau_L}\right) \cdot N_{T_1}(t) - \frac{N_{T_n}}{\tau_{T_n}} \quad (9),$$

where the first term is associated with the triplet to triplet absorption ( $T_1 \rightarrow T_n$  transition) and the second term describes losses of molecules in the  $T_n$  state, due to the rapid relaxation into the first excited triplet state.

While the number of molecules in the higher excited singlet and triplet states is known, it is possible to evaluate temperature at the quartz liquid interface which is created during the laser pulse using equation (10):

$$\frac{dT}{dt} = \frac{1}{\rho \cdot C} \cdot \left[ \left( \frac{h \cdot c}{\lambda_{exc}} - \Delta E \right) \cdot \frac{N_{S_2}(t)}{\tau_{S_n}} + \frac{h \cdot c}{\lambda_{exc}} \cdot \left( \frac{1}{\tau_{S_n}} \cdot N_{S_n}(t) + \frac{1}{\tau_{T_n}} \cdot N_{T_n}(t) \right) \right] \quad (10),$$

In all above mentioned equations (4)-(10)  $\sigma_{S_0}$ ,  $\sigma_S$ ,  $\sigma_T$  are absorption cross sections of the ground state, of the first excited singlet state and of the first excited triplet state, respectively,  $\tau_S$ ,  $\tau_T$ ,  $\tau_{ISC}$ ,  $\tau_{T_n}$ ,  $\tau_{S_n}$ ,  $\tau_L$  are the lifetimes of  $S_1$  and  $T_1$  states, intersystem crossing of molecules time, lifetimes of the  $S_n$  and  $T_n$  states and the laser pulse duration, respectively,  $\Phi_{fluor}$  is fluorescence quantum efficiency,  $\Delta E = 5.8 \cdot 10^{-19}$  J is energy difference between  $S_2$  and  $S_1$  states,  $\lambda_{exc}$  is excitation wavelength,  $h = 6.62 \cdot 10^{-34}$  J·s is the Plank constant and  $c = 3 \cdot 10^8$  m/s is the speed of light.

The temporal intensity profile of the XeCl excimer laser is slightly more complex compared to other lasers, and consists of two peaks, as shown in Figure 3-4 (solid line): one of them has a similar shape to the temporal profile obtained for other lasers, while second feature, which is much lower in intensity, is only observed for this type of lasers.

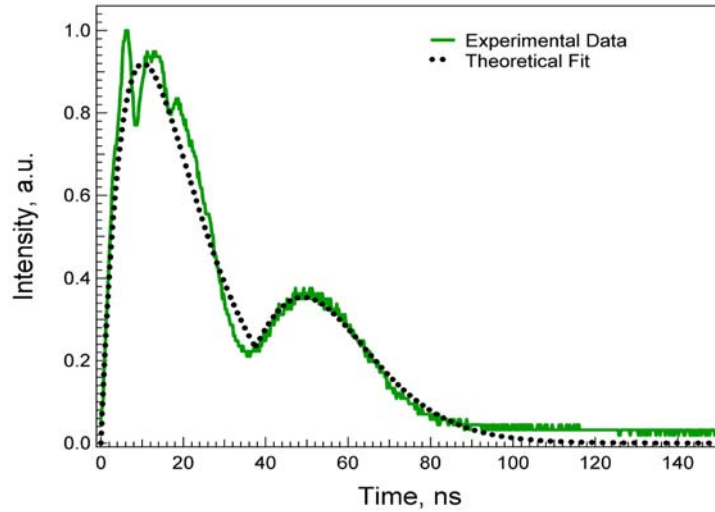


**Fig. 3-4 XeCl excimer laser temporal beam profile**

The temporal laser fluence profile is described therefore by the complex equation (11):

$$F(t) = \begin{cases} F_0 \cdot \left(\frac{t}{\tau_L}\right) \cdot \text{Exp}\left(-\frac{t}{\tau_L}\right), & \text{if } 0 < t < 36\text{ns} \\ \left(\frac{F_0}{816}\right) \cdot \left(\frac{(t-t_0) \cdot 1.75}{\tau_L}\right)^6 \cdot \text{Exp}\left(-\frac{(t-t_0) \cdot 1.75}{\tau_L}\right), & \text{if } 36 < t < 120\text{ns} \end{cases} \quad (11),$$

where  $F_0$  is the peak fluence,  $t$  is time,  $\tau_L$  is the peak laser pulse duration (24 ns),  $t_0$  is initial time variable, used to fit the experimentally obtained laser pulse profile (shown in Figure 3-4 as dotted line).

The parameters used for the simulation of the temperature jump at quartz-liquid interface for applying a XeCl excimer laser (308 nm) and 0.4 M pyrene in acetone solution are summarized in Table 1.

**Table 1.** Parameters used in temperature jump evolution model.

$\tau_L$ , ns	$\tau_S$ , ns	$\tau_{ISC}$ , ns	$\tau_T$ , ns	$\sigma_{S_0}$ , cm <sup>2</sup>	$\Phi_{\text{fluor}}$ , %
24	30 [53, 54]	160 [49, 50, 53, 54]	1000 [50, 54]	$4.8 \cdot 10^{-17}$	80 [51]

The values of the absorption cross sections for higher excited triplet and singlet states ( $\sigma_S$  and  $\sigma_T$ ) are difficult to find in the literature. These values are obtained experimentally by using a pump-probe technique [55]. However, the measured sample must transmit at least 10 % of the incoming laser beam intensity. In the case of 0.4 M pyrene in acetone solution the thickness of the liquid layer should be about 1  $\mu\text{m}$  in order to fulfill this requirement. This thickness, however, is not easy to achieve. Therefore it was assumed that the absorption cross section of  $S_1$  and  $T_1$  states are the same as  $\sigma_{S_0}$ .

The three major multi-cyclic non-radiative relaxations  $S_2 \rightarrow S_1$ ,  $S_n \rightarrow S_1$  and  $T_n \rightarrow T_1$  are contributed to the temperature rise at the quartz-liquid interface. It is therefore very interesting to investigate which of these relaxations have the highest impact in the formation of the temperature jump. For this reason the temperature jump during the 1.5 J/cm<sup>2</sup> XeCl excimer laser pulse at the interface between the quartz and 0.4 M pyrene in acetone solution was evaluated for three different relaxations (shown in Figure 3-5 A).

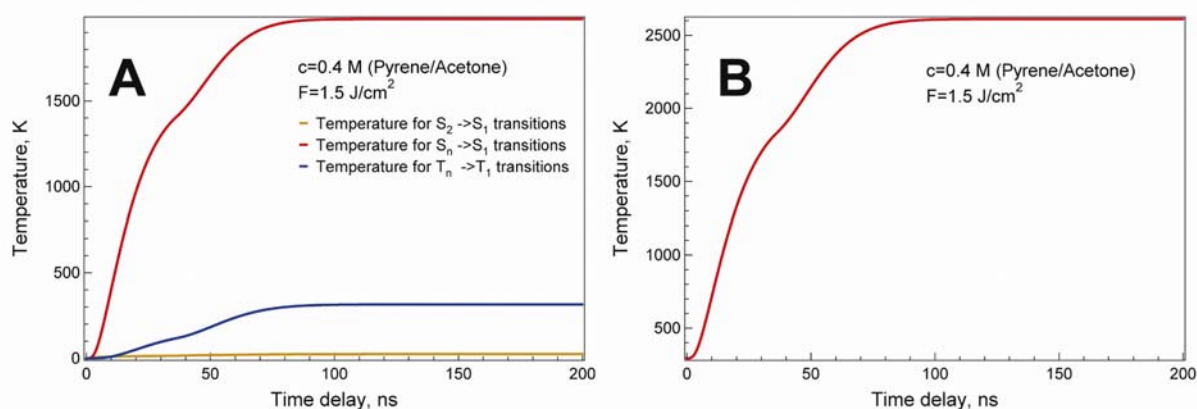


**Fig. 3-5 Evaluated temperature rise at the quartz liquid interface during the XeCl excimer laser pulse: influence of the non-radiative relaxation transitions on the T-jump (A) and complete T-jump (B).**

The major impact on the temperature formation process is obtained for non-radiative multi-cyclic transitions of the pyrene molecule from the highest excited singlet state  $S_n$  to the first excited singlet state  $S_1$ . The transition of  $T_n \rightarrow T_1$  is a bit less important than  $S_n \rightarrow S_1$ , but it still has a high impact in the temperature creation process. This result is contrary to the scheme proposed by Fukumura et al. [48] and Fujiwara et al. [54], which suggest that the cyclic non-radiative relaxation process between the triplet states is a key element in the temperature generation process. The explanation for the different results obtained by the above described theoretical modeling and results obtained in the literature [48, 54] can be ascribed to the higher absorption cross section of the triplet state compared to the singlet state absorption cross section. The values which were used in our model are the same. Nevertheless it can be concluded that the T-jump at the quartz-liquid interface is generated due to the multi-cyclic absorption and relaxation processes between the singlet and triplet states (transitions  $S_n \rightarrow S_1$  and  $T_n \rightarrow T_1$ , respectively). The value of the temperature jump is a sum of the temperatures generated by the non-radiative transitions between the singlet and triplet states as described above shown in Figure 3-5 B.

The temperature jump at the quartz liquid interface at a laser fluence of  $1.5 \text{ J/cm}^2$  with  $0.4 \text{ M}$  pyrene in acetone solution reaches a temperature of slightly above  $2500 \text{ K}$ . This value is much smaller compared to the temperature evaluated using the simple approach described by equation (2). The reason for this difference between the two models can be explained by the fact, that in the theoretical modeling of the laser induced temperature, expressed by



equations (4)-(10) the radiative energy losses between the states and pulse shape are taken into account. This model therefore represents a more real situation and temperature rise.

The modeled temperature jumps at the quartz-liquid interface at various XeCl excimer laser fluences for 0.4 M pyrene in acetone solution are illustrated in Figure 3-6.

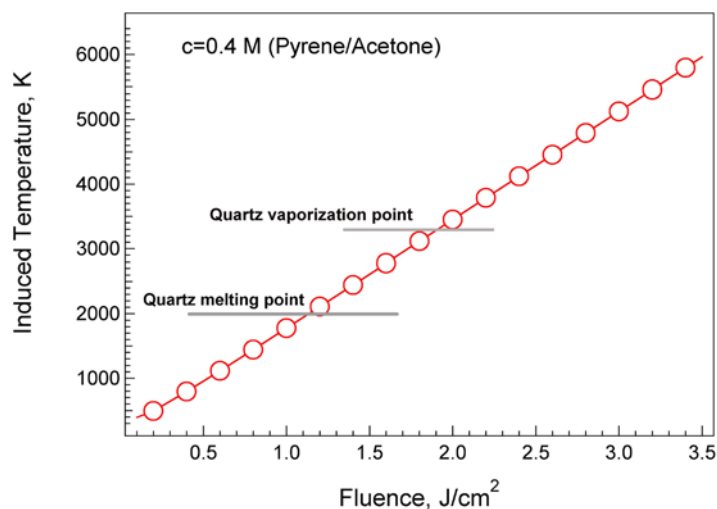


**Fig. 3-6 Laser induced temperature at quartz-liquid interface evaluated using theoretical model.**

It is important to mention, that these temperature jumps were evaluated *without taking into account the cooling processes*, which will be mentioned latter. The cooling of the temperature by dissipation to the surrounding solution also occurs during the laser pulse, however this is not included in this model.

The modeled laser induced temperature increases linearly with an increase of the laser fluence. An increase of the laser fluence also means a higher density of the photons, and a higher number of absorbed and relaxed molecules.

The etching mechanisms of LIBWE, as will be shown later, strongly depend on the applied laser fluence, i.e. on the laser induced temperature generated by the fast relaxation of pyrene molecules. Therefore it can already be concluded, that the temperature at the quartz-liquid interface plays a key role in LIBWE process.

The modeling also shows that the vaporization temperature of quartz is also exceeded for fluences above 2 J/cm². This suggests that direct vaporization is also possible and an important process. The fluence range between the melting and vaporization temperature coincides quite well with the "preferred" etching fluence (described later). In the fluence

range below the melting point of quartz other processes are important, i.e. incubation and the formation of carbon layers (discussed later in detail). At the high laser fluences, above 2 J/cm<sup>2</sup> etching mechanism is influenced by a number of processes, i.e. formation of plasma, or evaporation of quartz. The mechanism at this fluence range is again very different. The best etching conditions in terms of the etch roughness for quartz is achieved for 0.4 M pyrene in acetone solution at the fluence range of 1.2-2 J/cm<sup>2</sup>. This fluence range is used for the fabrication of micro-optical elements. Therefore the pressure jump behavior was studied in the detail for this fluence range.

The fast temperature rise at the quartz liquid interface does not remain constant for a long time, after the laser pulse has been absorbed by the solution. An efficient cooling process results in a fast decrease of the temperature with a *rate of several hundred thousands of K/s*! Such rapid cooling of the laser induced temperature jump in solutions has previously been reported in the literature [56-58]. The fast temperature increase and decrease at the interface between quartz and liquid results in several effects, which are mentioned above, but also other effects such as rapid boiling of the solution, which will be discussed in details in the following subchapter, chemical modification of the quartz, as will be described in subchapter 3-5, as well as others. All of those effects, such as the generation of shock waves due to the rapid boiling and thermal expansion of the solution or changes of the quartz composition, strongly depend on the rates of temperature increase and decrease. Rapid cooling also explains why high quality structures with the sharp etching edges can be obtained. Therefore, it is also important to investigate how fast the temperature at the quartz-liquid interface will decrease. Unfortunately up to now there have been no direct experimental methods for measuring temperature decays at this time scale and under these conditions, although some ideas for proving that there is a fast T-jump will be mentioned latter in this chapter. Initially an existing theoretical model for investigating the temperature decay at the quartz-liquid interface [48, 54] will be applied. The heat conduction equation which is used for modeling of temperature decay in materials is described by equation (12):

$$\frac{\partial T}{\partial t} = D_x \cdot \frac{\partial^2 T}{\partial x^2} + D_y \cdot \frac{\partial^2 T}{\partial y^2} + D_z \cdot \frac{\partial^2 T}{\partial z^2} \quad (12),$$

where  $t$  is the time,  $D_x$ ,  $D_y$ ,  $D_z$  are lateral and vertical thermal diffusivities, and  $x$ ,  $y$ ,  $z$  are the coordinates.

Taking into account that the lateral area irradiated by the laser is much bigger than the thermal diffusion length, equation 12 can be simplified to the one dimensional heat equation (13):

$$\frac{\partial T}{\partial t} = D_z \cdot \frac{\partial^2 T}{\partial z^2} \quad (13)$$

Even this equation is difficult to solve, because the two parameters time and space are interrelated. The solution of this equation is given in equation (14) [59]:

$$T(z, t) = T_{\max} + (T_0 - T_{\max}) \cdot \operatorname{Erfc}\left(\frac{z}{\sqrt{4 \cdot D_z \cdot t}}\right) \quad (14)$$

This form of the heat equation is derived from solving equation (12) by separating its variables and taking into account the boundary conditions, such as  $T(0)=T_{\max}$  and  $T(\infty)=T_0$ , where  $T_{\max}$  is the maximal temperature generated at the quartz-liquid interface during the laser pulse, while  $T_0$  is room temperature. The  $z$  represents the depth, which will be equal to the thermal diffusion length of fused silica, expressed by equation 15:

$$L_{th} = \sqrt{D_{silica} \cdot \tau} \quad (15),$$

where  $\tau$  is the time, at which the temperature reaches its maximum, which in most cases is equal to the laser pulse duration and  $D_{silica}=5.8 \cdot 10^{-7} \text{ m}^2/\text{s}$  is the thermal diffusivity of fused silica [60].

The thermal energy only penetrates  $250 \text{ nm}$  into the quartz during the XeCl excimer laser pulse, according to the equation (15). The temperature decay in the very thin  $250 \text{ nm}$  quartz layer at various times after the beginning of the XeCl excimer laser pulse at a fluence of  $1.5 \text{ J/cm}^2$  and for  $0.4 \text{ M}$  pyrene in acetone solution is shown in Figure 3-7.

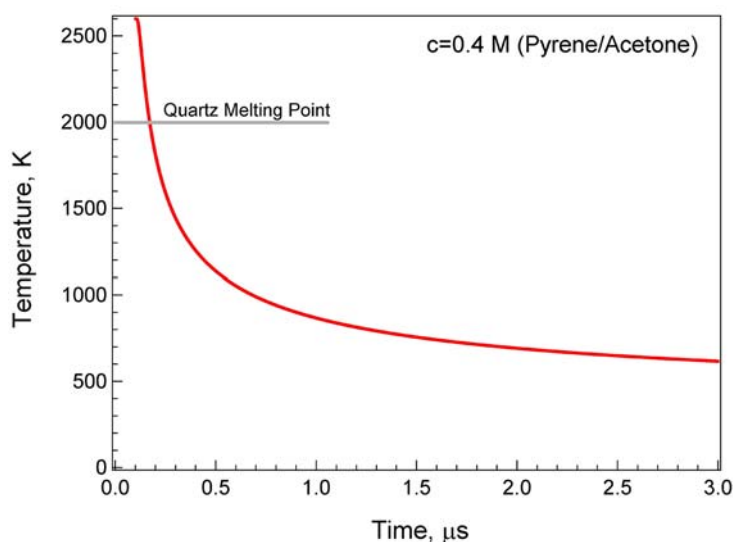


**Fig.3-7 Temperature decay at the quartz liquid interface.**

The temperature decrease from 2600 K down to 1000 K, suggested by this theoretical model, is very fast. A similar modeled temperature decay rate was also obtained at the interface between quartz and a naphthalene methyl methacrylate solution [60]. This suggests, that the cooling rate at the interface between the quartz and solution after the laser pulse is very fast. The theoretical modeling also affirms that the quartz surface stays molten for only a few hundred nanoseconds after the end of the laser pulse! This further suggests that the molten quartz must be removed in this short time scale. But the question still remains: is it really true that the temperature at the quartz-liquid interface is decreasing so fast? How could this be measured experimentally? The temperature decay could be obtained from the experimental data of pyrene emission. It was already mentioned that about 80% of the singlet excited pyrene molecules are losing energy through the emission of photons. In the literature several different types of pyrene fluorescence are described [49], including monomer and excimer emission. At a pyrene concentration in solution of about  $10^{-5}$  M or less the fluorescence of pyrene does not depend on the pyrene concentration in solution and is composed of single pyrene molecules fluorescence as shown in Figure 3-8 A. At higher pyrene concentrations ( $c > 10^{-3}$  M) in solution an excited pyrene molecule can form a short-lived molecule that bonds two molecules (one ground state and one excited state) in an electronic excited dimer state. Such a diatomic molecule is known as an excimer and is shown in Figure 3-B. Such molecules emit photons while

relaxing from the excited state to the ground state. However, excimer fluorescence emission is observed at a longer wavelengths range, compared to monomer fluorescence, as shown in Figure 3-8 A and B. This is because there is a small minimum in the potential energy surface of the excited  $S_1$ -pyrene and ground-state-pyrene system whereas no ground state dimer exists so that the energy of the potential energy surface is rising up at the same inter-atomic distances on the ground state surface. This makes the energy gap of excimer lower and therefore excimer fluorescence emission is shifted to the higher wavelengths.

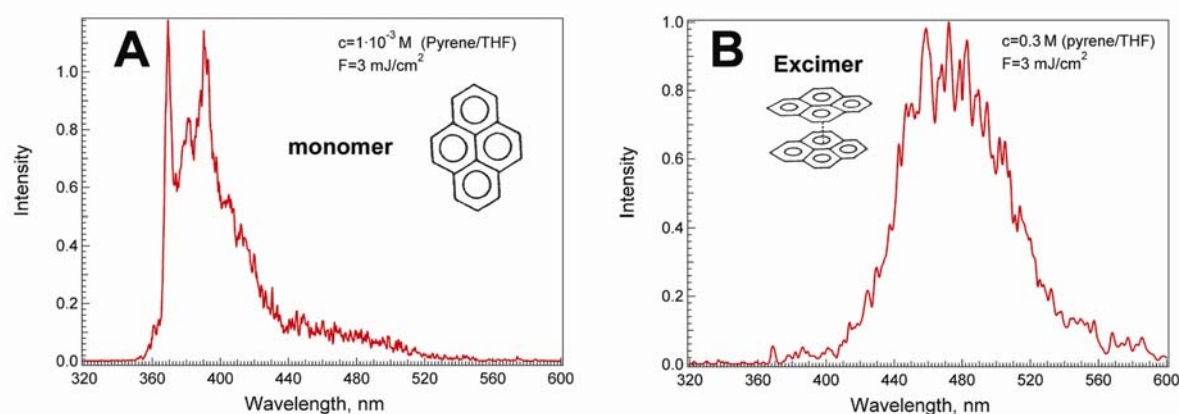


**Fig. 3-8 Monomer (A) and excimer (B) emission of pyrene.**

The monomer and excimer fluorescence of pyrene solution of two different concentrations, using an excitation wavelength of 308 nm, were measured using a time gated spectrometer. As expected, at pyrene concentrations of 0.3 M and with an excitation laser fluence of 3 mJ/cm<sup>2</sup> (500 times lower than the typical working fluence in LIBWE) pyrene rapidly forms the excimer and the monomer emission is barely detectable. However, with an increase of the laser fluence (above 80 mJ/cm<sup>2</sup>), the amount of monomer emission increases, as shown in Figure 3-9.

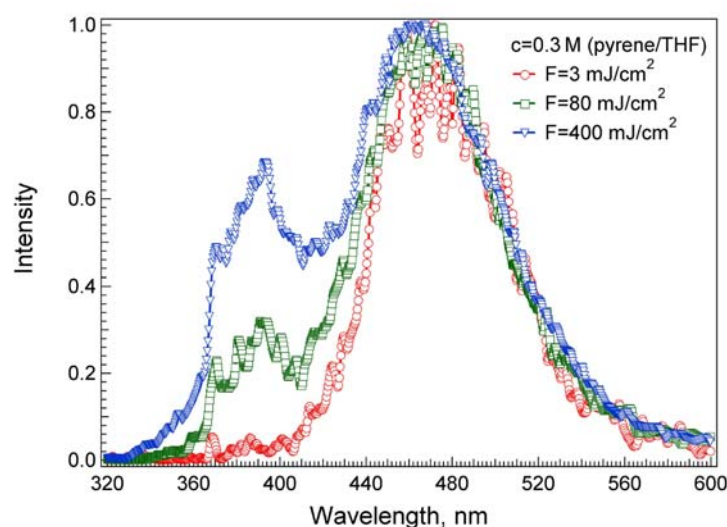


**Fig. 3-9 Monomer and excimer emission of pyrene at various XeCl excimer laser fluences.**

This phenomenon can be explained either by ground state monomer depletion [49] since excimer is formed from an excited and a ground state pyrene, or by the generation of a temperature jump in solution which causes a shift of the monomer-excimer equilibrium towards the monomer. This latter effect, if observable, suggests the interesting possibility to obtain a measure of the temperature by analyzing the change in the ratio of monomer to excimer emission. The ratio of the equilibrium constant between monomer to excimer should be related to the temperatures by the Van't Hoff isotherm:

$$\ln(K) = -\frac{\Delta H^0}{R} \cdot \left[ \frac{1}{T} \right] + \frac{\Delta S^0}{R} \quad (16),$$

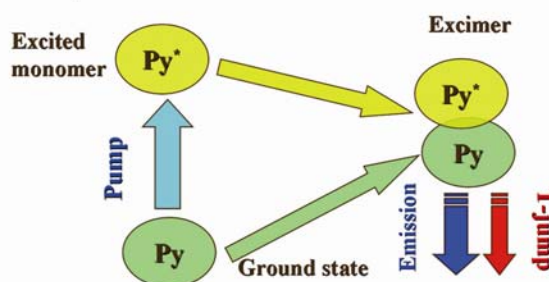
where  $\Delta H^0$  is the enthalpy change,  $\Delta S^0$  is the entropy change,  $R$  is the gas constant,  $T$  is the temperature.

The Van't Hoff equation in chemical thermodynamics relates the change in temperature to the change in the equilibrium constant given the enthalpy change. A detailed analysis of  $K$  and  $T$  could not be performed within the framework of this study. Therefore only a simplified analytical approach was used to get indications about the timescale of the temperature decay.

For this experiment two UV lasers pulses are required: one is an XeCl excimer laser (308 nm) for generating the temperature jump in solution, which will be referred to the pump laser pulse, and a second one, which is the 4<sup>th</sup> harmonic of a Nd:YAG laser (266 nm, 5 ns)

with a fluence of  $3 \text{ mJ/cm}^2$ , which will be referred to the probe laser pulse. This laser will be used for monitoring the changes in the excimer and monomer emission change after the absorption of the pump pulse. This means, that both lasers must be time synchronized and that the probe laser pulse is entering the sample at the time, when the pump pulse is over. The concept of this technique is illustrated in Figure 3-10.

### 1 Step:



### 2 Step:

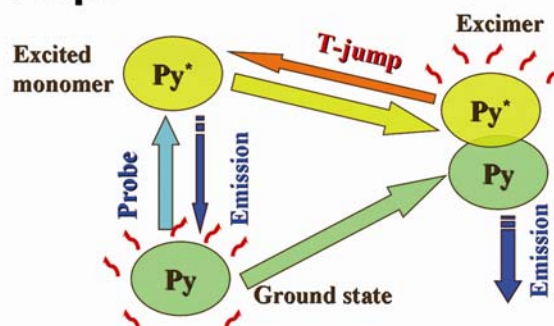


**Fig. 3-10 The concept of indirect measurement of temperature decay in solution using pyrene fluorescence.**

In the first step the pump laser pulse will excite the pyrene molecules from the ground state to an excited state. The excited pyrene molecules and the molecules from the ground state will form excimers due to the high pyrene concentration in solution, which will relax to the ground state either by emitting of photons (radiative relaxation) or by transferring their energy into heat (marked as Step 1 in Figure 3-10). At time delays of 100 nanoseconds to 100 microseconds after the end of the pump laser pulse a weaker probe pulse enters a hot solution (marked as Step 2 in Figure 3-10) when all pump-induced emission has ended. During the probe pulse, molecules from the ground state will be excited and together with

non excited molecules from the ground state will form excimers, similarly as in the case of the strong pump pulse. However, in the case of the probe pulse the excited pyrene molecules are surrounded by a hot solvent bath. The higher temperature in solution can shift the excimer-monomer equilibrium as indicated in Figure 3-10 by the arrow. For this reason we expect to detect not only the lower energy excimer emission but also an increased intensity of monomer emission. When the solution cools down, the ratio between the monomer to excimer emission should decrease due to a shift in the equilibrium towards the excimer.

Pyrene emission spectra in 0.3 M pyrene/THF solution with a  $3 \text{ mJ/cm}^2$  probe excitation laser pulse, which arrives at the time delays of  $1 \mu\text{s}$ ,  $10 \mu\text{s}$  and  $100 \mu\text{s}$  after the pump laser pulse with fluence of  $700 \text{ mJ/cm}^2$ , are shown in Figure 3-11.

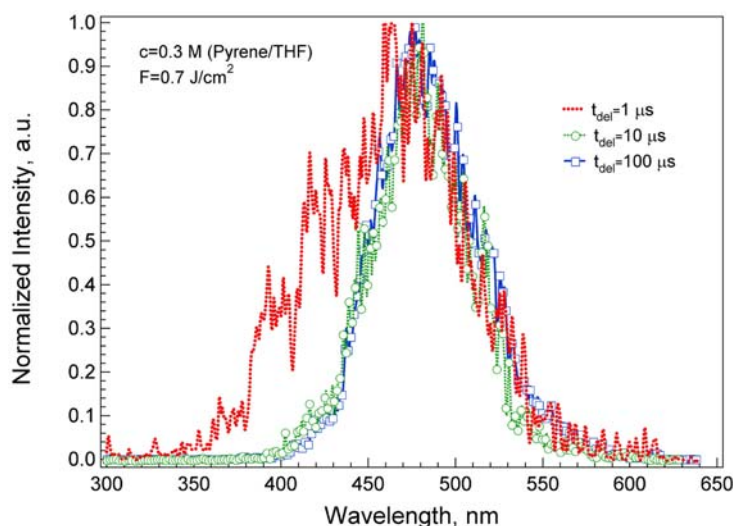


**Fig. 3-11 Emission of pyrene excimer irradiated with probe pulse at various delay time between pump and probe laser pulses.**

It is clearly visible that at the time delay of  $1 \mu\text{s}$  after the pump pulse, fluorescence of pyrene is significantly broadened and consists of both monomer and excimer emissions. Strong enhancement of the monomer emission is also visible at the time delays from 500 ns to  $1 \mu\text{s}$  after the pump laser pulse. However, already after a  $10 \mu\text{s}$  delay almost no monomer emission is observed. According to the simplified model described above, a fast decay of excimer suggests also a fast cooling process. The ratios of monomer to excimer emission intensities are integrated over 360-420 nm and 440-620 nm, respectively, for the various delays between the pump and probe pulses (shown in Figure 3-12 as open circles).



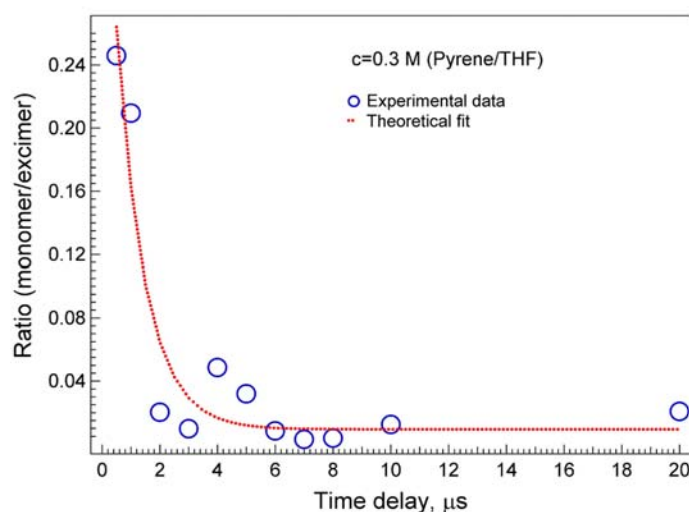


**Fig. 3-12 Ratio of integrated monomer to excimer emission intensities at various time delay between the pump and probe laser pulses.**

The experimental data suggest that the temperature jump at the quartz-liquid interface decays within the first microsecond. Initially it seems very rapid, but it needs to be considered, that the heated liquid layer is very thin (below  $1\ \mu\text{m}$ ) and that the thermal conductivity of the environment is high (much higher than in air). Therefore, fast temperature decays can be expected. This fast drop in temperature agrees quite well with the value obtained from the previously described theoretical modeling of the T-jump (shown in Figure 3-7) and is also similar to the temperature decay obtained in the work of Vass et al [60].

The fast temperature rise and cooling at the interface between the quartz and solution results, as discussed above, in several effects: depending on the irradiation fluence the T-jump can be high enough to melt or even boil the quartz surface. On the other hand it also results in the fast boiling and evaporation of the solution, which induces high pressure shock waves that travel through the solution. This pressure jump plays a key role in the process of removing of quartz and will be discussed in detail later. The combination of temperature and pressure jumps and their importance in the LIBWE process were mentioned in many papers describing the LIBWE process [30, 31, 33, 34, 38, 41, 42, 46, 60, 61]. Currently, however, there is no clear experimental proof that the temperature at the

quartz-liquid interface exceeds the melting point of quartz or rises even higher. However it is agreed, that the LIBWE process is based on the temperature jump at the material-liquid interface resulting from the strong absorption of laser radiation and rapid non radiative relaxation of molecules, which also causes a number of effects such as heating of the quartz surface and explosive boiling of the solution. The latter effect may be also as important as the T-jump especially in the previously described "preferred" fluence range and will be described in details in the following subchapter.

### ***3.2 LIBWE mechanisms: Pressure jump***

In the 3.1 it was described that the laser light is absorbed by the solution, which results in the enhancement in a T-jump. The increase in the temperature from 20°C up to 2500°C, within the ns laser pulse, results in rapid thermal expansion and vaporization of the solution. This effect could be imagined in the following way: if we take a hot metal plate, with a surface temperature of 400 °C and drop a bit of water on this plate. The water starts immediately boil and evaporate, resulting in a steam rising up and a "hissing" sound. This sound is produced because of the fast change from the liquid phase to the vapor, which also results in a change of pressure and volume which cases in generation of a sound wave. Similar effects occur in LIBWE at the thin interface between the liquid and material with the difference that in LIBWE the vapors are surrounded by incompressible liquid. The fast temperature rise results in the fast volumetric expansion of the vapors and liquid, which creates high pressure acoustic shock waves with a magnitude that is *thousands times higher than atmospheric pressure*. These high pressure shock waves move with a *velocity of several kilometers per second* in both directions: toward the solution and also toward the transparent material, as shown in Fig. 3-13.

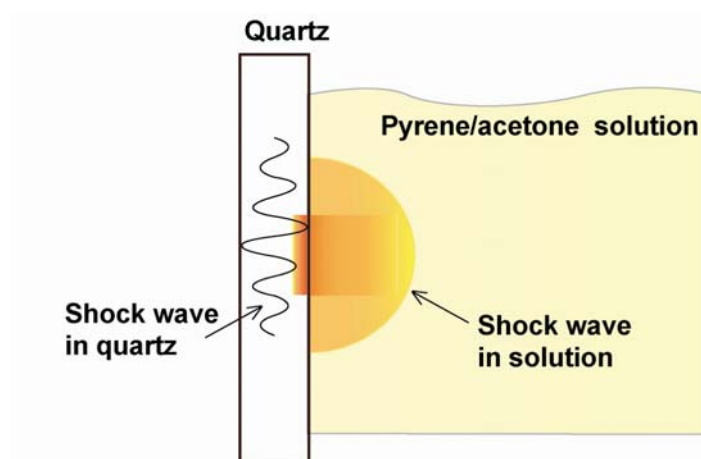


**Fig. 3-13 Formation and expansion of the shock wave in solution and in quartz.**

These pressure waves could easily move liquid away from the solid surface, because the liquid does not hold its form different to the solid. These pressure waves easily overcome the elastic limit of the liquid and generate photo-acoustic cavities. Further, it may be expected that a weak point in this system would be the interface between the quartz and the liquid as this has a finite surface energy. Solid materials, on the other hand, have a bigger Young's modulus and are much more resistant to pressure wave induced stress. Thus they can keep their form. This is true for many materials at room temperature. However, at temperatures close to the melting point of the solids, the mechanical stability of the material with respect to external pressure strongly decreases. This allows us to remove molten material from its surface with several times less pressure than is needed to structure the same cold material. It is therefore very likely that the pressure jump which is directed toward the material is a key element in the removal process when the quartz melts and is below the vaporization temperature.

The pressure jump which is directed toward the solution and its concomitant related processes, were proposed previously as a key element in the mechanical removal of UV transparent materials [31, 46]. Therefore it is also important to understand the processes that occur in the solution upon generation of these strong shock waves.

At temperatures and pressures above the critical point the liquid is transformed into supercritical liquid where no thermal equilibrium between the vapor and liquid phases exists. Therefore the solution does not boil and vapor bubbles are not seen. However as the temperature and pressure decrease from their highest values just after the T-jump the liquid

moves out from its supercritical state. At this time boiling occurs, which causes in the formation of the expanding bubble. This bubble grows and reaches a maximum size, as shown in Figure 3-14.

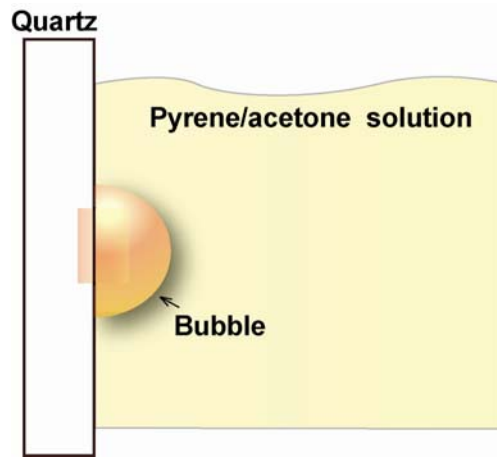


**Fig. 3-14 Formation of laser induced bubbles in solution.**

At this time the pressures and temperature inside the bubble and that those of the surrounding liquid are equalized. The bubble cannot increase in size further, unless additional thermal energy is supplied. Because of the very low laser repetition rate used in our experiments the time delay between the two laser pulses is larger than time scale of the entire LIBWE process and there is therefore no way for the bubble to get thermal energy from the second laser pulse. The pressure inside the bubble starts, therefore, to decrease. When the pressure inside the bubble is much lower than the surrounding liquid pressure the bubble can no longer keep its volume and collapses as shown in Fig. 3-15. The collapse of the bubble generates a liquid jet, which causes a pressure jump strong enough to remove molten material, and which is also directed toward the material surface. This effect is also known as cavitation [56-58, 62-66].

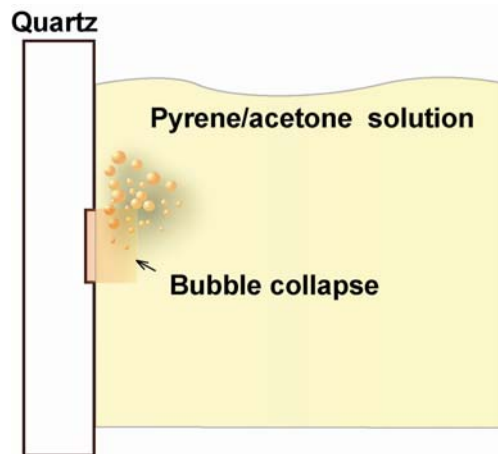


**Fig. 3-4 Collapse of the laser induced bubbles.**

This is the reason why this pressure jump was proposed as material removal mechanism in LIBWE process [30]. However, the formation of the bubble, its growth and its collapse are relatively long processes and the molten surface at this time may be already solidified. For this reason it is more likely that the acoustic pressure jump, which is generated just after the T-jump and directed toward the molten material surface is more important for the mechanical removal process [60, 67]. It is very important therefore to find a way for experimental investigation of all above described processes and the dynamics of the pressure jump. It is clear that conventional instruments for determining pressure, such as manometers will not be useful in the case of LIBWE, because they are too slow to respond. One of the techniques for directly monitoring a pressure jump in solution during and after the exposure to laser light is the application of poly-vinylidene fluoride (PVDF) needle hydrophones. This technique was successfully applied for determining of the pressure jump evolution at the quartz-liquid interface when pure toluene was used as etching media [38, 67]. However, this approach could not be applied for measuring of the pressure jump when acetone or THF solution is used as the “etchant”, because the PVDF is soluble in these solvents.

One technique that can be applied for monitoring all above described processes (formation of shock waves, generation of bubbles, bubble growth and collapse) is shadowgraphy. The pressure jump can be evaluated from the experimentally obtained bubble growth and collapse dynamics. The experimental setup for the shadowgraphy measurements is shown in Fig. 3-16.

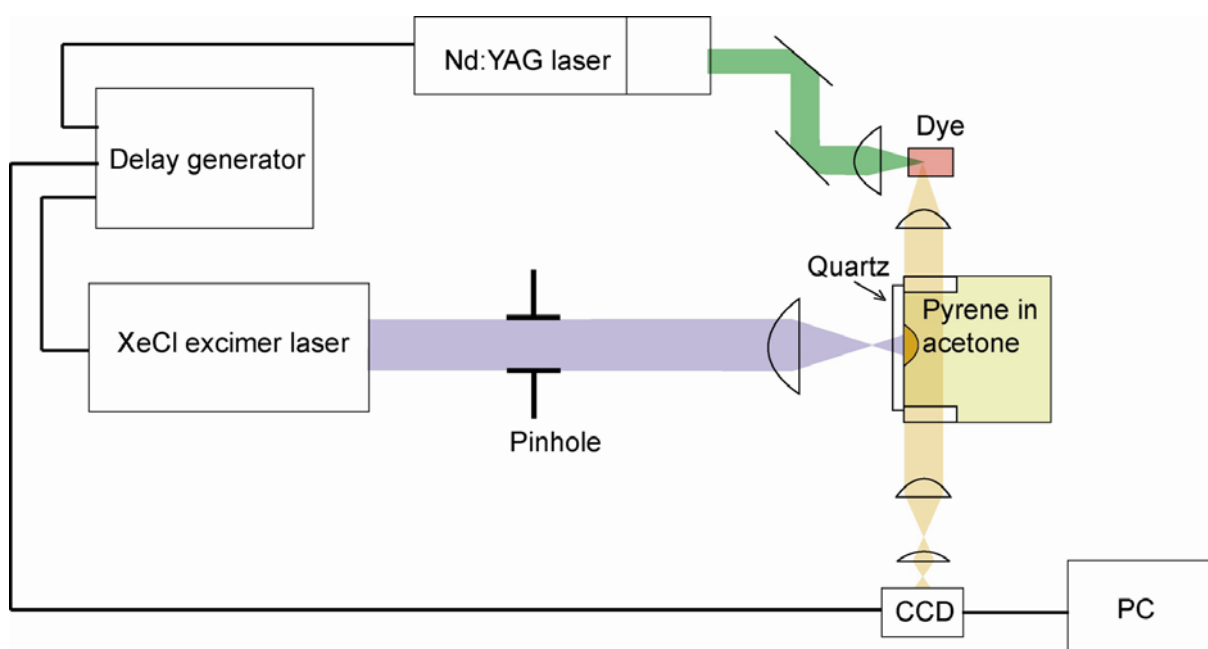


**Fig. 3-16 The experimental setup of time-resolved shadowgraphy technique.**

An XeCl excimer laser was applied as the pump laser. The most homogeneous part of the laser beam was selected using a pinhole and imaged onto the backside of the quartz, which was in contact with the 0.4 M pyrene in acetone solution. The irradiation area on quartz was  $500 \times 500 \mu\text{m}$ . The 2<sup>nd</sup> harmonic of a Nd:YAG laser (532 nm, 5 ns) was used as the probe pulse. The beam of the probe laser was focused into a quartz cuvette containing 3 mM aqueous dye (Rhodamin-6G) solution to generate a strobe light. In principle the 2<sup>nd</sup> harmonic of the Nd:YAG laser can be used directly as the strobe, however this laser is strongly coherent and the contrast between the bubble and the solution is therefore not so high. On the other hand, dye converts the coherent green laser light into incoherent yellow light ( $\lambda_{\text{emission}} = 580 \text{ nm}$ ). The cuvette and microscope with a CCD camera are mounted perpendicular to the quartz surface. The fluorescence light emitted from the dye solution was used to illuminate the backside of the quartz, where the shock wave and the generation of laser induced bubbles occurs. The changes at the quartz liquid interface that occurred during the laser wet etching process were monitored with the CCD camera. The time delay between the pump and probe laser pulses were varied by the delay generator (DG-535). The evolution of the hemispherical shock waves at the quartz-liquid interface, when using a laser fluence of  $1.5 \text{ J/cm}^2$  and 0.4 M pyrene in acetone solution as etching media, is shown in Fig. 3-17.

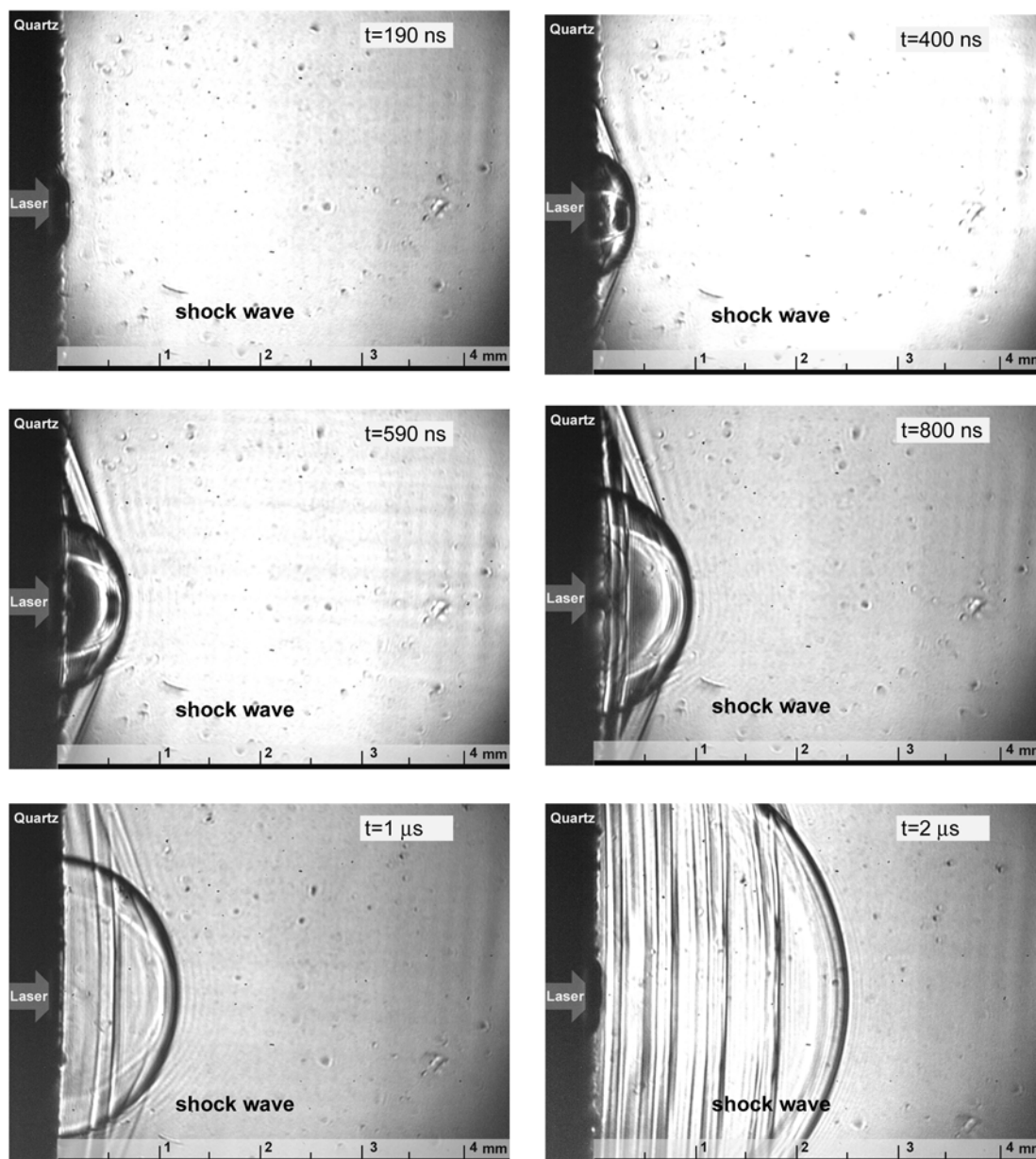


**Fig. 3-17 Evolution of shock wave in 0.4 pyrene/acetone solution at 1.5 J/cm<sup>2</sup> excitation fluence.**

The time delay between the pump and probe laser pulses,  $t$ , is defined as the difference between the beginning of the pump laser pulse  $t_{0\text{pump}}$  and beginning of probe laser pulse  $t_{0\text{probe}}$ . The beginning of the pump and probe laser pulse is defined as the time when the laser pulse intensity is equal to 3 % of its maximum, as shown in Fig. 3-18.

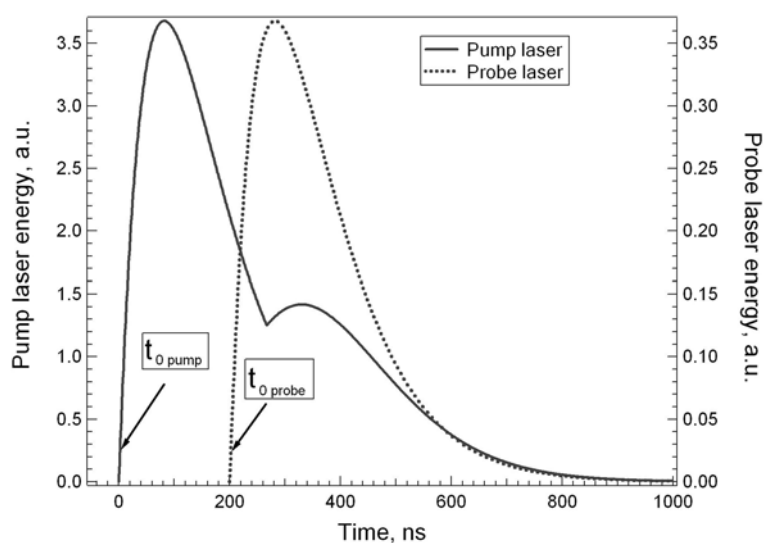


**Fig. 3-18 Temporal shape of pump and probe laser pulses.**

The shock waves occur, as discussed above, because of the rapid evaporation and thermal expansion of the liquid. About 200 ns after the arrival of the pump laser pulse a small liquid surface deformation is visible. A clear vaporization of solution and rapid expansion of the vapors are visible at 400 ns after the beginning of the laser pulse (shown in Figure 3-17). At this moment the formation of the acoustic waves is evident (shown in Figure 3-17). The shock wave expands in the solution almost hemispherically. The shock wave front radius evolution in 0.4 M pyrene/acetone solution using  $1.5 \text{ J/cm}^2$  excitation fluence is evaluated from the shadowgraphy images (shown in Figure 3-17) and is summarized in Fig 3-19.

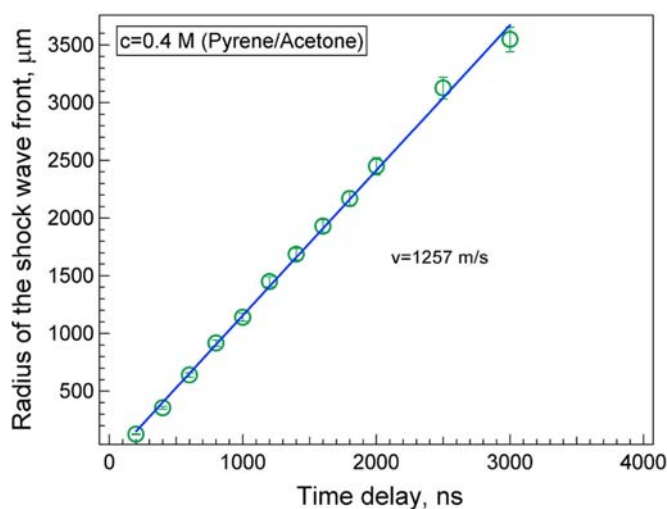


**Fig. 3-19 The radius of the shock waves at different time delays.**



The measurements of the shock wave propagation show that it expands linearly over the entire measured time range. The velocity of this acoustic wave in solution is evaluated by dividing the measured shock wave radius with the time delay between the pump and probe laser pulses and is in the range of 1250 m/s. This value is very similar to the speed of sound obtained for acetone (1200 m/s) [68]. Knowing the speed of sound we can roughly estimate a pressure jump at the beginning of the shock wave formation. This can be evaluated using equation 17, suggested by Kim et al. [58]:

$$P = \frac{v \cdot \beta \cdot F}{C_p \cdot \tau} \quad (17),$$

where  $v$  is the speed of sound in solution (1257 m/s),  $F$  is the laser fluence (1.5 J/cm<sup>2</sup>),  $C_p$  is the heat capacity of acetone (2.2 J·kg<sup>-1</sup>·K<sup>-1</sup>),  $\tau$  is the XeCl excimer laser pulse duration and  $\beta$  is the volumetric thermal expansion coefficient.

The latest parameter is a property of acetone which describes the volumetric fractional change of acetone at the given temperature which is expressed by the following equation (18):

$$\beta = \frac{1}{\rho} \cdot \left( \frac{\partial \rho}{\partial T} \right)_p \quad (18),$$

where  $\rho$  is the density of the liquid at constant pressure and  $T$  is the temperature.

Experimental data of density and heat capacity at various temperatures for acetone are very difficult to find in the literature. Therefore theoretical simulations of the thermodynamic properties of acetone at various temperatures [69] are shown in Figure 3-20 and will be used for the calculation of  $\beta$ .

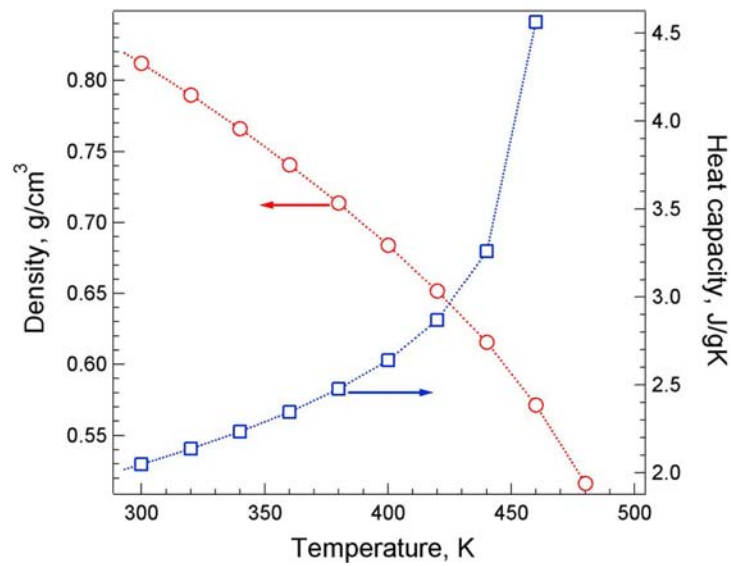


**Fig. 3-20 Theoretical simulation of the acetone density and heat capacity at different temperatures.**

Now it is possible to evaluate the volumetric expansion coefficient by using equation (18) using the theoretically obtained density values. This coefficient depends also on the temperature and is increasing with an increase of  $T$ , as shown in Figure 3-21 A. The shock wave pressure jump (shown in Figure 3-21 B) at the quartz-liquid interface is possible to estimate using equation (17), when the volumetric expansion and heat capacity of acetone as function of the temperature are known.

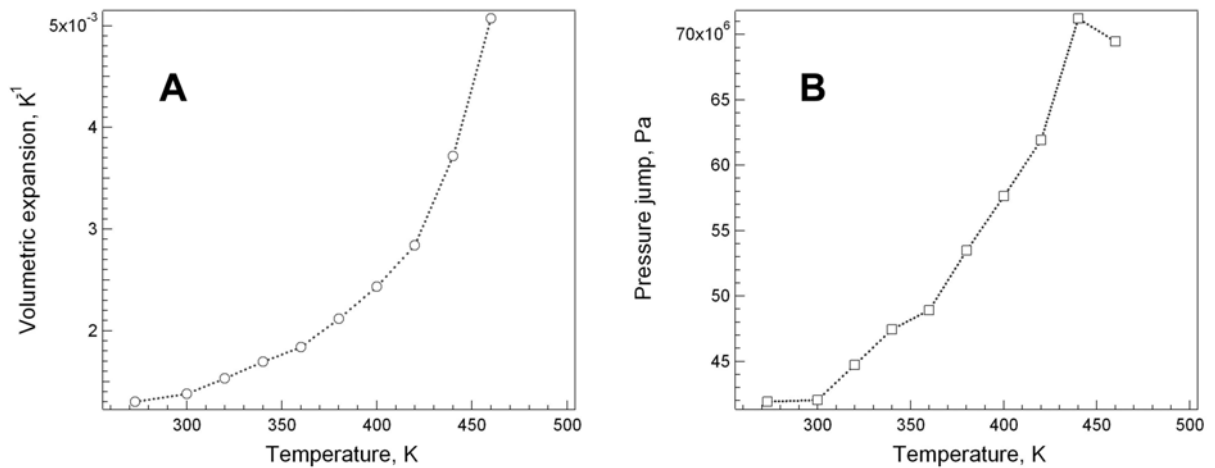


**Fig. 3-21 Volumetric expansion coefficient of acetone (A) and pressure jump at the interface between liquid and material (B)**

The evaluated pressure jump at the material-liquid interface is 70 MPa (700 times higher than the atmospheric pressure!). However the pressure jump obtained at 460 K is lower than the value for 450 K. This observation can be explained by the change from the liquid to the gas phase of the solution. This pressure jump was obtained for the surrounding liquid temperature of 230 °C and just at the very earlier stage of the shock waves, i.e. when the shock waves are only starting to expand. It is also important to remember, that this P-jump is expanding in both directions: towards the liquid and towards the hot/molten material surface. It is most probable that the magnitude of the P-jump which enters the material is similar to that obtained for the solution. Is this pressure jump high enough for removing the hot/molten material? Unfortunately, it is fairly difficult to find data for the dependence of mechanical properties of fused silica on temperature. It is known, however, that by pressing a quartz plate with a compressive strength of 1.1 GPa (or 11000 time higher than atmospheric pressure) at room temperature, the material breaks [68]. By heating the quartz surface, the mechanical properties of quartz change. This results, most probably, in a reduction of the compressive strength value, which is necessary to remove the hot/molten material from the surface. This is probably the reason why quartz can be structured by LIBWE at pressures well below the compressive strength of quartz at room temperature.

The pressure jump at the interface between the material and liquid, which has been evaluated from the shock wave expansion measurements, does not provide information about the dynamics of the pressure jump, which may help to understand the time scale at which etching of quartz by LIBWE occurs. It has already been discussed, that the LIBWE process does not end with the generation of the shock waves. After some time, when the pressure in solution is decreasing, a bubble starts to form. This process can also be monitored with the shadowgraphy measurements. The dynamics of the laser induced bubble at the quartz-liquid interface is shown in Fig. 3-22. An analysis of the growth and collapse of laser induced bubble can give also some useful information about the pressure jump evolution at the quartz-liquid interface.

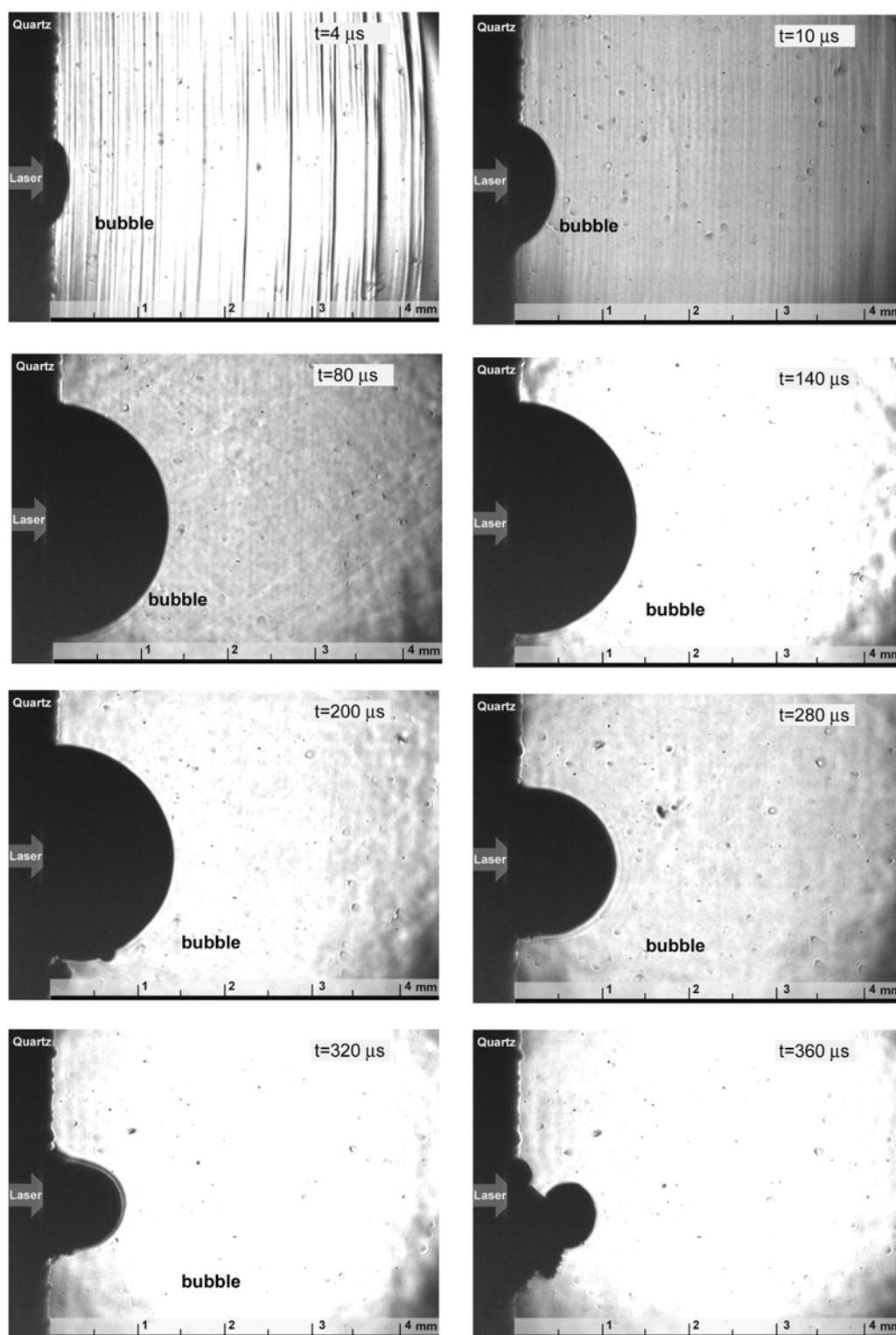


**Fig. 3-22 Evolution of a laser induced bubble in 0.4 M pyrene/acetone solution at 1.5 J/cm<sup>2</sup> excitation fluence.**

At the beginning of the bubble formation process, which is obtained around 2  $\mu\text{s}$  after the beginning of the pump laser pulse only a small, i.e. 50  $\mu\text{m}$ , bubble is observed. This bubble contains, most probably, many micro-bubbles, which can not be resolved by the shadowgraphy technique. At 6  $\mu\text{s}$  after the beginning of the pump laser pulse the bubble starts to grow, while the pressure and temperature at the quartz-liquid interface decrease due to the efficient cooling process and the further volumetric expansion of the bubble. The thermal energy which was used to heat the quartz surface does not disappear. It can only be converted from one type of energy into another. In the case of LIBWE, the thermal energy at the quartz-liquid interface is converted into shock wave energy and kinetic energy of the laser induced bubbles growth. The latter process results in rapid expansion of the bubble, as illustrated in Figure 3-22. The growth of the laser induced bubble in solution is strongly dependent on the absorbed laser energy and environmental conditions, i.e. the surrounding liquid pressure. When the kinetic energy of the bubble growth can constrain the pressure inside the bubble which is larger than surrounding liquid pressure, then the bubble grows. The bubble does not expand to infinite size due to the limited thermal energy input and relatively high surrounding liquid pressure. At some point in time the pressure inside the bubble and of the liquid are equalized. This happens at 220  $\mu\text{s}$  after the beginning of the pump laser pulse as shown in Figure 3-22. The maximum bubble size in this case is 1.4 mm. At this time scale the kinetic energy of the bubble growth is decreasing because of the decrease of thermal energy at the quartz-liquid interface so the bubble shrinks. At 360  $\mu\text{s}$  after the beginning of pump laser pulse the internal bubble pressure is not high enough to keep the form of the bubble and the bubble collapses. This result in the generation of a 2<sup>nd</sup> pressure jump which is, as discussed above, directed toward the quartz surface and may also play an important role in the LIBWE process.

As already mentioned before, it is possible to evaluate the pressure jump evolution from the experimental data of shadowgraphy (shown in Figure 3-22). The dependence of the experimentally obtained bubble radius at various times after the 1.5 J/cm<sup>2</sup> pump pulse is shown in Figure 3-23 with square symbols. The round patterns in Figure 3-23 represent the growth and collapse velocity of the laser induced bubble, which was evaluated from the experimental results of the laser induced bubble radius by using equation (19):

$$v = \frac{dR}{dt} \quad (19),$$

where  $R$  is the bubble radius and  $t$  is time.

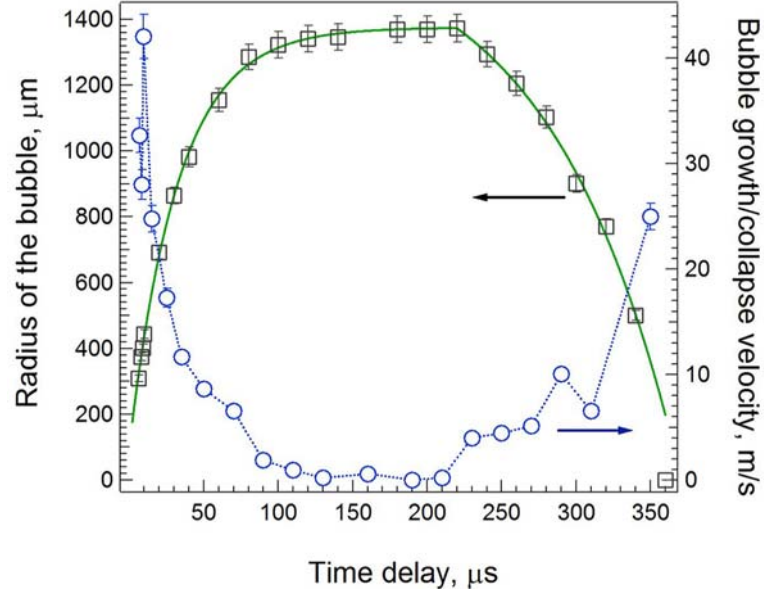


**Fig. 3-23 Laser induced bubble radius (square symbols) and bubble growth velocity (circle symbols) evolution.**

Now we can estimate the pressure jump at the quartz-liquid interface resulting from the collapse of the laser induced bubble, which is, as discussed above, directed towards the hot quartz surface. This pressure jump is described by equation (20):

$$P \approx \rho \cdot v \cdot v_c \quad (20),$$

where  $v_c=25$  m/s is the speed of the bubble collapse,  $v=1250$  m/s is the sound velocity in solution and  $\rho=870$  kg/m<sup>3</sup> is the density of acetone.

The collision of the laser induced bubbles induces a pressure jump of 27 MPa (this pressure is similar to that obtained at 2700 meters below the sea level!), which is directed towards the hot quartz surface. Although the value of pressure jump associated with the collapse of the laser bubble is 2 times less than the pressure created by the shock waves, it would still most probably be sufficient to remove the molten quartz from the surface. The other question is of course, whether the quartz still in its molten form at the time of bubble collapse. The temperature at the quartz liquid interface decays, as discussed above, from

the 2600°C to 1000°C within less than one microsecond (see Figure 3-7), while the collapse of laser induced bubble occurs at 360  $\mu$ s after the laser pulse.

In summary we have now two events which create a pressure jump: shock wave and the bubble collapse. It is also interesting to know the pressure jump evolution over the complete time scale of the LIBWE process. It is also interesting to know, whether the pressure jump decreases much faster than the temperature.

The analysis of the pressure evolution at the quartz-liquid interface starts with fitting the experimentally obtained bubble radius with the mathematical function [60, 66] described by equation 21:

$$R(t) = a - b \cdot c^t \quad (21)$$

where a, b and c are fitting constants which are equal to:

$$\begin{aligned} a &= 1374; \quad b = 1273; \quad c = 0.97; & \text{when } 6\mu\text{s} \leq t < 220\mu\text{s} \\ a &= 1635; \quad b = 21.3; \quad c = 1.012; & \text{when } 220\mu\text{s} \leq t < 360\mu\text{s} \end{aligned}$$

The theoretical fit is shown in Figure 3-23 as green solid line and agrees very well with the experimental data. The pressure jump dynamics at the quartz-liquid interface can be analyzed by equation 22 [60, 66]:

$$P\left(R(t), \frac{\partial R}{\partial t}\right) = \left(p_{stat} - \frac{2 \cdot \sigma}{R_{max}}\right) \cdot \left(\frac{R_{max}}{R(t)}\right)^{3 \cdot K} - \frac{2 \cdot \sigma}{R(t)} - \frac{4 \cdot \mu}{R(t)} \cdot \frac{\partial R}{\partial t} \quad (22),$$

where  $p_{stat}$ =101 kPa is the static pressure,  $\sigma$ =23·10<sup>-5</sup> N/m is the surface tension of acetone,  $R_{max}$ =1.4 mm is the measured maximum radius of the laser induced bubble,  $\mu$ =3.26·10<sup>-4</sup> Pa·s is acetone's dynamic shear viscosity,  $t$  is time,  $R(t)$  is bubble radius evolution, described by equation (20) and  $K = \frac{4}{3}$  is the polytropic exponent which represents the ratio of specific heat of vapors and non-condensable gases.

The pressure jump rise and decay evaluated by equation (22) is illustrated in Figure 3-24.

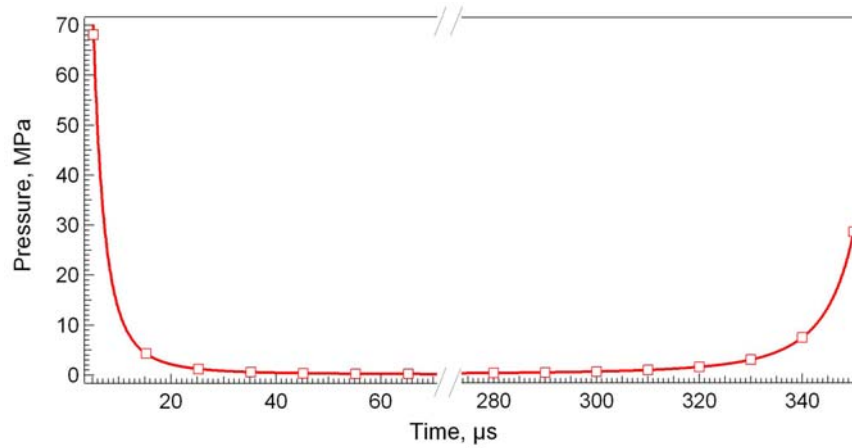


**Fig.3-24 Dynamics of the pressure jump during the shock wave formation and bubble growth/collapse for 1.5 J/cm<sup>2</sup> laser fluence and 0.4 M pyrene in acetone solution.**

The evaluated pressure jump at the beginning of the formation of the shock wave evaluated by equation (16) is 70 MPa. The pressure jump, which is evaluated by equation (22) and using bubble growth/collapse dynamics, is decreasing when the bubble starts to form, which is around 5 μs after the laser pulse. The next pressure jump at 360 μs corresponds, as discussed above, to the collapse of the laser induced bubble.

Combining the two facts of the fast temperature decay and bubble collapse time of 360 μs after the pump laser pulse one could conclude that the collapse of laser induced bubble plays only a minor role in removal process. A similar conclusion was also reached by Vass et al. [60] and Kawaguchi et al. [67].

There are three events that govern the pressure jump at the quartz-liquid interface during the LIBWE process: shock wave, laser induced bubble growth and bubble collapse. The pressure jump which is obtained during the formation of the shock wave reaches values of 70 MPa or more and is a key element in the process of mechanical removal of the molten material process. The pressure during the formation of the bubbles is much smaller, but can also have an influence on the removal process. The next pressure rise occurs at latter time scales and is caused by the collapse of the laser induced bubble. Although the value of this pressure is high enough to remove the molten material from the surface, this pressure jump, most probably, plays only a minor role in LIBWE process, because the quartz may be already solidified at these times.



### ***3.3 LIBWE mechanisms: when etching occurs?***

The question whether removal of molten quartz occurs within the first microsecond after the laser pulse is still open. The investigation of the time scale on which removal of quartz takes place can be achieved by surface interference measurement.

The experimental set up for surface interference measurements consists of one semitransparent mirror, which divides the incoming laser irradiation into two beams with equal intensities. One beam is transmitted through this mirror and passes onto a high reflective mirror from which the beam is reflected back. The other part of the beam which is reflected from the semitransparent mirror travels through the quartz sample, which is in contact with solution, and is reflected back from the quartz-liquid interface. The optical path from the semitransparent mirror to the reference mirror and to the sample must be equal.

The reflected beams from the reference mirror and from the sample create the interference patterns. The shift between the interference fringes strongly depends on the optical path difference between the quartz and the reference mirror. This technique is, therefore, very sensitive to the surface morphology of the sample, which can be measured with an accuracy that is in the range of several nm!

The alteration of the quartz surface after or during the XeCl excimer laser pulse can be detected by using a pump probe technique, i.e. similar to that which was applied in subchapter 3.1. This technique is called as *nanosecond surface interferometry* [70] and can provide an information about the surface modification in space and also in time! The application of this method for LIBWE requires several modifications: firstly, the contrast in the interference images strongly depends on the ratio between the light intensity reflected from the quartz-liquid interface with the light intensity reflected from the reference mirror. The intensity of the reflected light is proportional to the refractive index difference between the two media. The reflection from the quartz-liquid interface is proportional to the difference of the refractive indices of the quartz and solution. The refractive index of quartz is 1.41 at 532 nm, while the index of refraction of acetone and THF is 1.38 and 1.4 respectively. These small differences of refractive indices of quartz and solution result in a very weak intensity of the reflected beam from the quartz-liquid interface and results, therefore in a weak contrast between the fringes in the interference image. It is, therefore, necessary to reduce the intensity of the light, reflected from the reference mirror. This is achieved by inserting a neutral density filter with variable transmission in the reference beam path. It is also necessary to use wedged quartz samples to separate the reflection from the front and backside of the sample which is difficult to achieve in other ways.

The second important effect is the sudden change of the refractive index of the quartz-liquid interface due to the rapid temperature changes, evaporation of the solution, formation of the shock waves and laser induced bubbles. These effects result in an increase of intensity of the light reflected from the interface between the quartz and the solution which causes saturation of the CCD camera. For this reason the intensity of the laser light and neutral density filter must be continuously adjusted in a way to detect the best contrast in the interference image.

The experimental setup of nanosecond laser surface interferometry is shown in Figure 3-25.

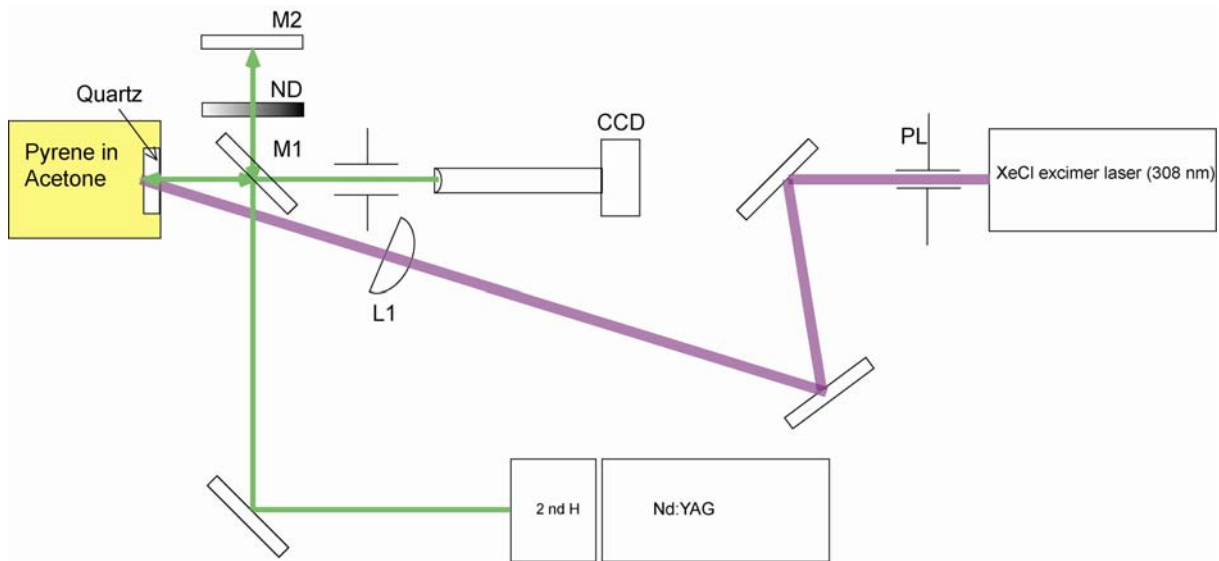


**Fig. 3-25 Nanosecond surface interference setup.**

A XeCl excimer laser beam passes through the square 5x5 mm pinhole (PL) and is imaged with a lens ( $L_1$ ) with the focal length of 250 mm onto the backside of the quartz, which is in contact with the 0.4 M pyrene in acetone solution. The diameter of the laser beam on the quartz is  $500 \times 500 \mu\text{m}$ , while the laser fluence is  $1.5 \text{ J/cm}^2$ . The beam of the 2<sup>nd</sup> harmonic Nd:YAG laser (532 nm, 6 ns) is split into two beams of equal intensity by a beam splitter  $M_1$ . The transmitted beam passes through the neutral density filter  $ND$  and is reflected back from the mirror  $M_2$ . The reflected beam passes through the wedge quartz plate, which is in contact with the solution and is reflected back from the backside of the quartz plate. The reflected beams create interference patterns which are imaged into the CCD camera. The Nd:YAG and XeCl excimer lasers are synchronized by the delay generator (DG-500). This allows us to change the time delay between the both lasers.

The surface interference image which is recorded at 800 ns after the pump laser pulse is shown in Figure 3-26 2.

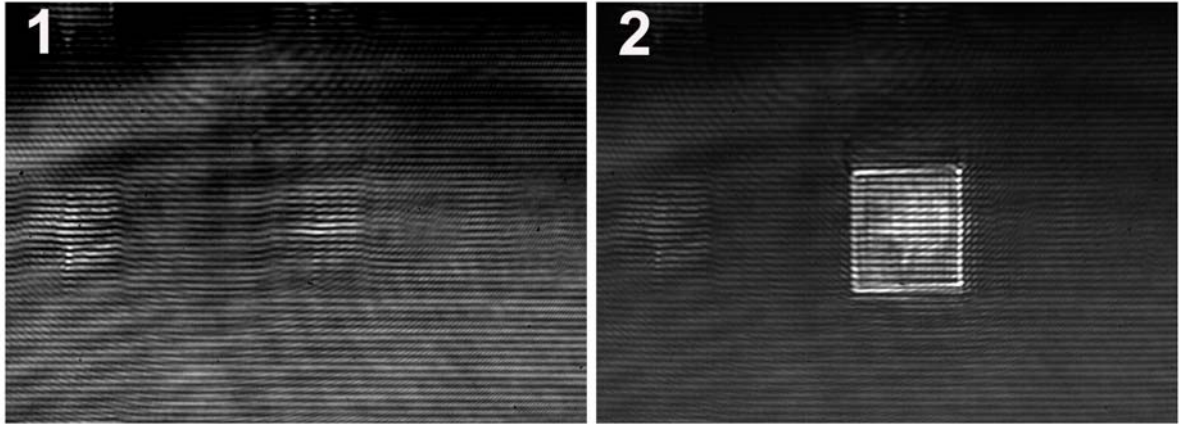


**Fig.3-26 The interference images before (1) and during (2) the pump laser pulse. The time delay between the pump and the probe pulses is 800 ns.**

The bright area in Figure 3-26 2 is equal to the size of the pump beam. The color change of this area from dark to white is due to the change in the index of refraction of the quartz surface at the interface between the material and liquid. The alteration of the refractive index of quartz depends on several effects: removing of the material, fast heating and cooling processes and boiling of the liquid. In order to clarify the possible time range for the structuring of quartz, the interference images recorded at various time delays between the pump and probe pulses have been analyzed by a mathematical model described in the literature [70]. This analysis is based on the fast Fourier analysis of the interference images, recorded without and with the pump pulse. The two events are obtained from this model: amplitude image and phase image. The amplitude images at various time delays after the pump pulse suggest the change of the intensity of the probe beam reflected from the quartz-liquid interface, while the phase images provide the information about the altering of surface morphology and the refractive index change. The change of the surface morphology is obtained by analyzing the phase shift in the images shown in Figure 3-26 and can be evaluated by using equation (23) [70, 71]:

$$\Delta d = \frac{1}{4 \cdot \pi} \cdot \frac{\Delta \varphi \cdot \lambda}{n_D} \quad (23),$$

where  $\Delta d$  is the change of the surface morphology,  $\Delta \varphi$  is the phase difference,  $\lambda$  is laser wavelength (532 nm) and  $n_D$  is the refractive index of quartz.

The change of the index of refraction of quartz surface can give the answer to the question when removal process takes place. The phase images which are recorded at the different time between the pump and probe laser pulse are shown in Figure 3-27.

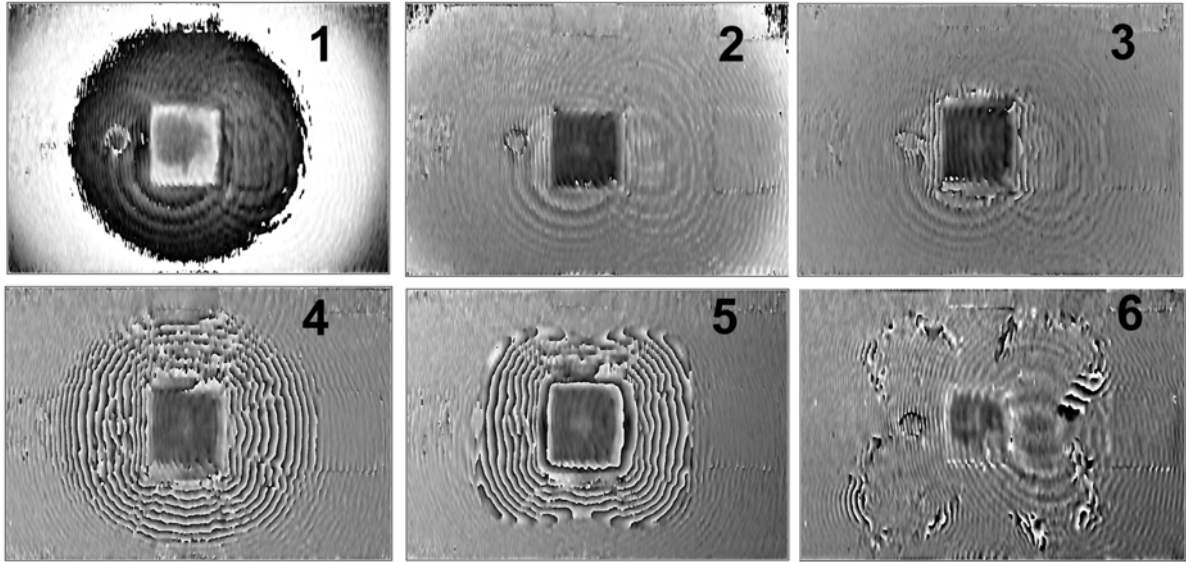


**Fig. 3-27 Phase shift images recorded at different time delays after pump pulse: 200 ns (1), 800 ns (2), 3  $\mu$ s (3), 30  $\mu$ s (4), 280  $\mu$ s (5) and 360  $\mu$ s (6).**

The first phase image is recorded at the time of formation of the shock wave in solution. The round black ring is associated with the phase jump larger than the dynamic range of  $2\pi$  which occurs due to the rapid shock wave expansion. The square bright pattern in the center of image agrees well with the size of the irradiated area in quartz. In this time delay, according to temperature and pressure models, which are described in subchapters 3.1 and 3.2, the temperature exceeds the melting point of quartz and the pressure jump at the quartz-liquid interface is reaching its highest values. The white color of the rectangular area in image 1 (shown in Figure 3-27) may be due to several effects: bending of the quartz surface due to the fast increase of the T-jump and P-jump and penetration of the temperature in solution and in quartz. At the time delay of 800 ns after the laser pulse the shock waves expands outside of the visible area and only a gray rectangular pattern in the image is visible. The size of this feature is similar to that obtained in the first image which is shown in Figure 3-27. The analysis of the phase change [70] obtained in the second image (shown in Figure 3-27) suggests that the refractive index of quartz is strongly changed in the first micrometer layer. This result, however, does not suggest that the first

micrometer of the quartz surface has been molten or removed. The reason for the refractive index change, as was already mentioned, can be related to the temperature generated at the quartz-liquid interface, which penetrates inside the material. The penetration depth of the T-jump in quartz, according to equation 15, is 680 nm at 800 ns after the pump pulse. This agrees well with the depth of the refractive index change obtained at this time scale. At 3  $\mu$ s after the pump laser pulse small ripples around the irradiated area are visible. These ripples are related to the formation of the laser induced bubble which grows and collapses (as shown in Figure 3-27 3-6). At the time delay of 360  $\mu$ s the bubble collapses. The clear rectangular pattern in the center of the phase image (shown in Figure 3-27 as 6) at this time delay is clearly visible. This area represents the etched feature in quartz, but the contrast of this structure is smaller compared to other images. This can be explained by the fact that the depth of this etched feature is only 5 nm.

The images of the phase change at the quartz-liquid interface recorded at the different time delays after the XeCl excimer laser pulse does not give a clear suggestion about the time scale at which the material removal takes place. However, analysis of the phase shift images suggest, that the irradiated areas stays almost the same in size over the complete measured time delay range. This result can not be explained only by the laser induced temperature and resulting change of the refractive index of quartz, because the temperature decays, according to the model (subchapter 3.1), rapidly within the first microseconds after the laser pulse. An explanation for the clear observation of the square pattern in the phase shift images at the delays above 10  $\mu$ s after the pump laser pulse is associated with the removal of the quartz. This confirms that the pressure jump generated by the formation of the shock waves or by the bubble growth removes the molten quartz. Again, this analysis is focused on the "preferred" laser fluence range where the quartz could exist in the molten phase.

Two major processes of LIBWE can be suggested from the above described measurements: a temperature jump and a pressure jump. The increase of the temperature at the thin interface between the quartz and liquid is due to the strong absorption process and results in heating/melting or boiling of the quartz surface, generation of high pressure shock waves and expanding/collapsing bubbles. The pressure jump created by the expansion of the shock waves or bubble growth removes the molten material mechanically.

The removal of quartz is a very fast process, which occurs at the first few microseconds after the laser pulse. The enhancement of the temperature at the quartz-liquid interface strongly depends on the applied laser fluences: at the low laser fluences the mechanism of LIBWE is influenced by the chemical decomposition of solution and formation of an absorbing layer, as will be shown later.

The temperature rise exceeds 4000 K when high laser fluences (above 2.2 J/cm<sup>2</sup> for 0.4 M pyrene in acetone solution and XeCl excimer laser) are used, which could result in boiling of quartz and in the formation of the plasma in solution, which will be discussed in details later.

### ***3.4 Etch rate, etch roughness and incubation effect of quartz by laser assisted wet etching***

One of the most important characteristics of laser ablation process is the etch rates of the material. This can be obtained using two different methods: measuring the weight of the material loses by using *Quartz Micro-Balance* (QMB) or by measuring the depth profile of the ablation crater.

Quartz Micro-Balance has been used for measuring the etch rates of the polymers, where the polymer is spin-coated on the quartz which oscillates at the fixed frequencies [72]. The frequency is changing when the polymer is removed by laser ablation. The amount of material which is ablated is evaluated from the frequency change. Unfortunately, this technique could not be applied for the LIBWE process.

The second method for measuring the etch rates is based on the examination of the etched features by profilometer. This method has been used to obtain the etch rates of UV transparent materials by LIBWE. This approach consists of several steps. Firstly, an array of square patterns in quartz is fabricated (shown in Figure 3-28).

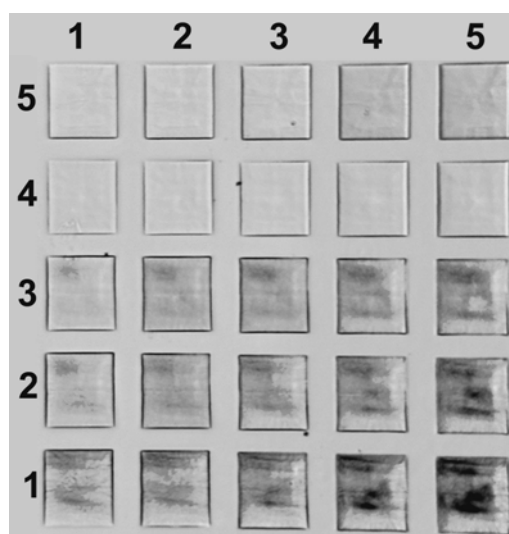


**Fig. 3-28** The part of the square patterns array etched in the quartz plate by LIBWE.

Each pattern was etched by using a set of different laser fluences and number of laser pulses. The parameters which were used for the fabrication of the pattern array (shown in Figure 3-28) are summarized in Table 2.

**Table 2.** Number of pulses and fluences which are used for the investigation of quartz etch rates by LIBWE

row/ column	1	2	3	4	5
1	F=1.0 J/cm <sup>2</sup>				
	400 pulse	500 pulse	600 pulse	700 pulse	800 pulse
2	F=1.1 J/cm <sup>2</sup>				
	350 pulse	400 pulse	500 pulse	600 pulse	700 pulse
3	F=1.2 J/cm <sup>2</sup>				
	250 pulse	300 pulse	350 pulse	400 pulse	500 pulse
4	F=1.27 J/cm <sup>2</sup>				
	200 pulse	250 pulse	300 pulse	350 pulse	400 pulse
5	F=1.52 J/cm <sup>2</sup>				



	60 pulse	70 pulse	80 pulse	90 pulse	100 pulse
--	----------	----------	----------	----------	-----------

The number of the applied laser pulses depends on the laser fluence, as shown in Table 2. The strong increase of the pulse number at the low laser fluences is related to the *incubation* effect, which will be explained in detail in the following section. On the other hand, a certain number of laser pulses ( $>200$ ) at laser fluences  $>1.5 \text{ J/cm}^2$  results in breaking of the quartz plate. This fact may be related to the structural changes of quartz which will be discussed later. An experimental setup for the fabrication of square patterns in quartz is illustrated in Figure 3-29.

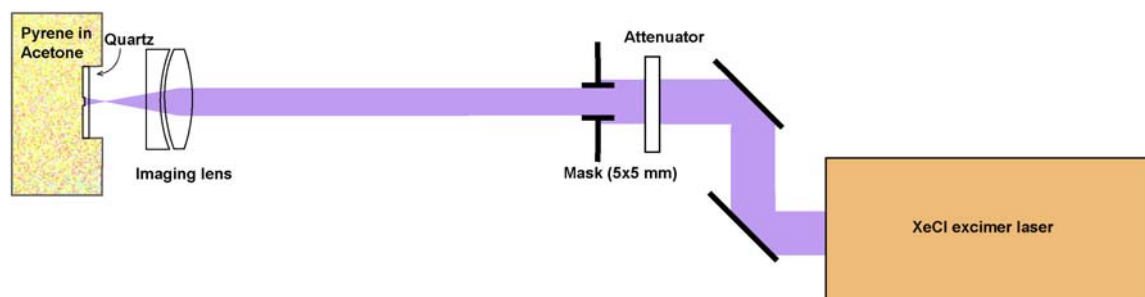


**Fig.3-29 Experimental setup for investigating of the etch rate of quartz by LIBWE.**

A XeCl excimer laser (308 nm) with a beam size of 15x20 mm passes through the dielectric attenuator plate, which is continuously reducing the incoming laser beam intensity. A 5x5 mm square aperture selects homogeneous part of the laser beam which is imaged with the lens ( $f_{\text{lens}}=100 \text{ mm}$ ) onto the backside of the 25x25 mm quartz plate. The quartz plate is in contact with a 0.4 M pyrene in acetone solution. The size of the square patterns which are etched in quartz is 350x350  $\mu\text{m}$  (as shown in Figure 3-29).

The second step is the determination of the depth of the etched features. These measurements were performed using the stylus instrument DEKTAK-8000. This instrument measures the depth of the structures with a resolution of better than 1 nm. The scan length can be varied from 50 micrometer to 200 mm. The stylus of this instrument is in physical contact with the sample surface. A stylus force of 30 mg was used for the surface scan of the structures fabricated in UV transparent materials by LIBWE, while the scanning rate was in the range of 10-100  $\mu\text{m/s}$ . The surface profiles of the square features (shown in Figure 3-29) are illustrated in Figure 3-30.

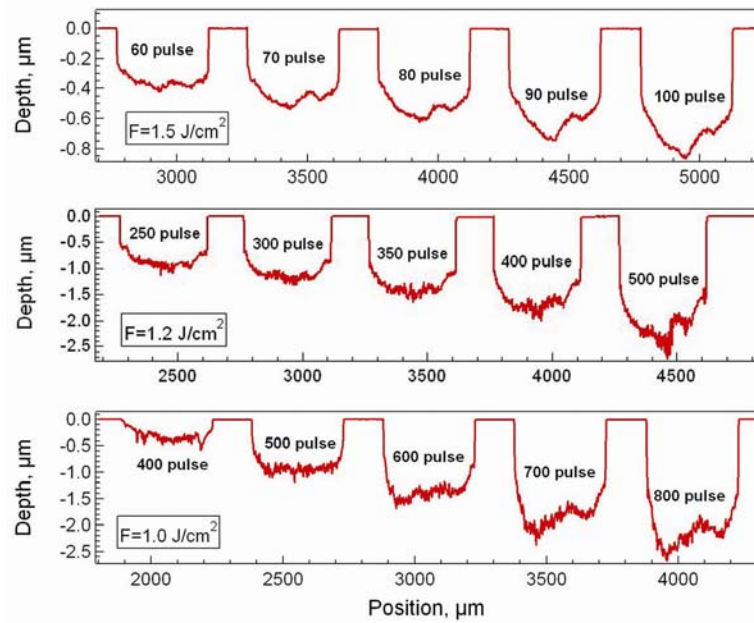


**Fig. 3-30 Surface depth profile of the structures etched in quartz using various laser fluences and pulse numbers.**

The non-homogeneous and slightly deformed profiles of the etched features in quartz may be due to energy fluctuations in the laser beam. The etch depth of quartz by LIBWE for various laser pulse numbers and laser fluences are shown in Figure 3-31.

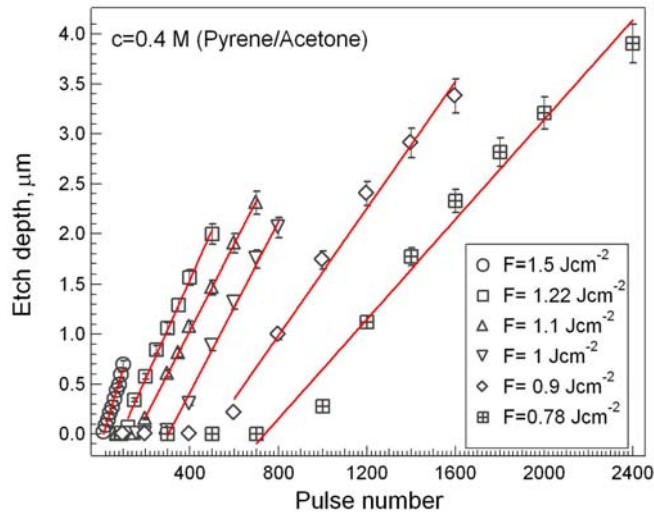


**Fig.3-31 The etch depth of quartz at various pulse numbers for different laser fluences.**

The etching at the low laser fluences does not start with the first laser pulse (shown in Figure 3-31). This phenomenon is known as *incubation* and is also obtained in the

femtosecond laser ablation process [73]. The etch depths (shown in Figure 3-31) are fitted by equation (24) in order to evaluate the etch rates and number of the incubation pulses:

$$d(N) = \text{erate} \cdot (N - N_{\text{inc}}) \quad (24),$$

where  $d$  is the etch depth,  $N$  is the number of the applied laser pulses,  $\text{erate}$  is the etch rate at the fixed laser fluence,  $N_{\text{inc}}$  is the number of incubation pulses.

The results of the analysis are shown in Figure 3-31 as solid lines.

The surface profiles of the structured areas measured with the DEKTAK provide also values for the etch roughness. The roughness of the etched features is defined as the root-mean-square of the deviation from the average depth, measured at the bottom of the etched patterns. The etch rates, etch roughness and the number of the incubation pulses for quartz structured at XeCl excimer laser (308 nm) fluences using 0.4 M pyrene in acetone solution are presented in Figure 3-32 (1) and Figure 3-32 (2).

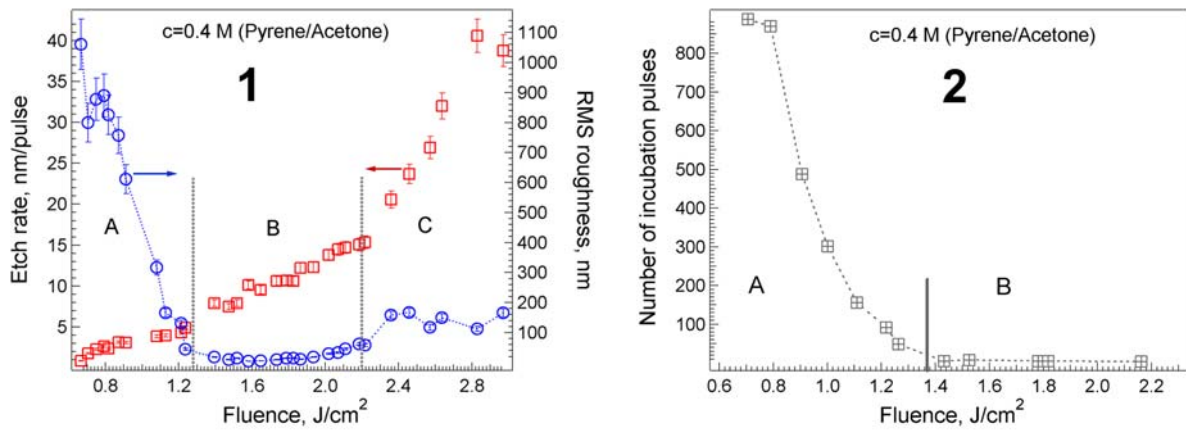


**Fig.3-32 The etch rate and etch roughness (1) and number of incubation pulses (2) for quartz by LIBWE using 0.4 M pyrene in acetone solution.**

One of the characteristic parameters of the LIBWE process is the threshold fluence which is defined as the lowest energy density below which no clear etching is observed. The threshold fluence cannot be detected from the etch rate slope shown in Figure 3-32 due to the strong incubation effect. The threshold fluence is, therefore, obtained experimentally by measuring the etch depth at various pulse numbers until the fluence is obtained at which no etching is detected even after 5000 cumulative laser pulses. The value of the threshold fluence for quartz by LIBWE using 0.4M pyrene in acetone solution is 0.66 J/cm<sup>2</sup> which is

well below the ablation threshold without solution ( $F=20 \text{ J/cm}^2$ ) [74]. The difference in the threshold fluences for quartz etched with and without solution is due to the different etching mechanisms. Ablation of the quartz without solution is assisted, as discussed above, by the formation of absorption centers (optical defects) inside the quartz [15, 17, 74]. These defects absorb the laser light and therefore initiate the damage of the quartz surface. The mechanism of LIBWE is based, as discussed above, on the creation of a very high temperature jump and the mechanical removal of molten material in a certain fluence range. The high quality structures in UV transparent materials without cracks can be produced due to the fast temperature rise, relative low pressures and fast cooling process.

The experimentally obtained etch rates of quartz reveal a complex behavior where several etching processes are involved (marked in Fig. 3-19 as A, B and C). However, the etch rates over each regions are linear. The lowest etch rates are observed at the low laser fluences (marked as A in Fig. 3-19). This can be due to the several effects: the laser induced temperature at the quartz liquid interface may be below the melting temperature of quartz, as discussed in subchapter 3.1, but high enough for softening the quartz surface. The pressure wave, generated by the shock waves and collapsing of the bubbles may not be strong enough to remove the heated (*but not molten!*) material from the surface. This may be one of the reasons why the etching at the low laser fluences does not start with the first laser pulse, but after a certain number of incubation pulses (as shown in Fig. 3-19 B). The temperature jumps at these fluences are high enough to decompose the organic solution, which results in the formation of the amorphous carbon layer on the quartz surface. The carbon layer will alter the absorption of the laser energy due to an increase of the absorption. The incubation process can be therefore assigned to the formation of a carbon layer that confines the absorption of the laser energy into a thinner layer, which increases the magnitude of the temperature jump. This causes the generation of the higher temperature jump, which now exceeds the melting temperature of quartz. Another effect which may influence the etching in this fluence range is associated with the different thermal expansion coefficient of the carbon layer compared to quartz, which will result in an additional mechanical stress [75]. The combination of different absorption layer (carbon and solution) and mechanical stress could also be the reasons for the high etch roughness detected at low laser fluences (shown in Figure 3-32 A).

The increase of the etch rates at the intermediate fluence range (marked as B in Figure 3-32) is due to the increase of the temperature jump, which exceeds the melting temperature of quartz (2000 K) but is probably below the vaporization temperature of quartz (Figure 3-6). The higher laser induced temperatures will also generate stronger pressure jumps, compared to the low laser fluences. This P-jump removes now the molten material from the surface. This mechanism yields smooth etching features in quartz with a roughness of  $\leq 20$  nm.

A change in the etch rates slope at the highest laser fluence range (marked as C in Figure 3-32) may be due to the generation of very high temperatures which may cause several effects: boiling of the quartz surface and plasma formation in solution. These effects result in an increase of the etch roughness (shown in Figure 3-32 A). The latter effect will be described in details later.

The experimental data of the etch rates, etch roughness and number of incubation pulses suggest that mechanisms of LIBWE consist not only of pure photothermal and mechanical removal processes, but also chemistry, i.e. carbon layer formation. The pyrolysis and the plasma formation in the solution play critical role in the LIBWE process. It is therefore very important to understand this phenomenon, which is discussed in detail in the following subchapters

### ***3.5 Surface analysis of the etched areas in quartz by LIBWE: study of atomic carbon***

The initial results of the surface analysis of the etched quartz by LIBWE suggested no significance carbon formation [31]. More systematic studies of the etched areas in quartz by LIBWE [61] showed, however, strong carbon formation on the quartz. The mechanism of LIBWE, as already mentioned above, is assisted not only by the thermal and mechanical processes, but also by the thermal decomposition of the solution and the generation of a plasma. Therefore it is not surprising, that the areas of quartz structured at various laser fluences reveal a different appearance, as shown in Figure 3-33.

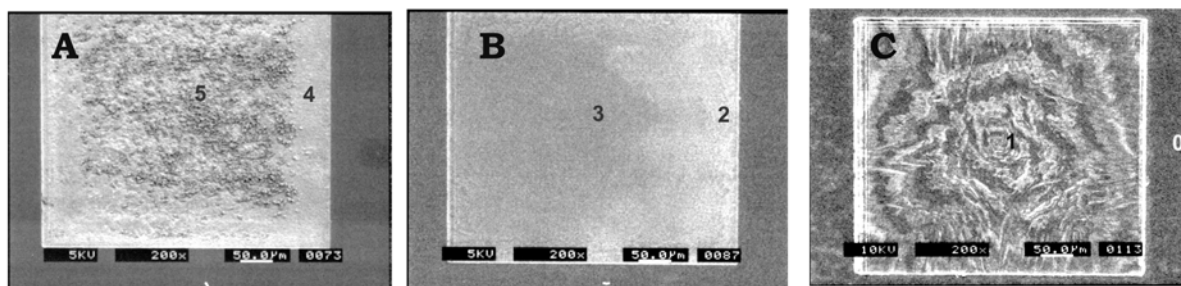


**Fig. 3-33 Scanning electron microscope images of the etched features surface in quartz by LIBWE using 0.4 M pyrene in acetone solution at different XeCl excimer laser fluences and different laser pulse numbers: 0.8 J/cm<sup>2</sup>, 3000 pulse (A), 1.5 J/cm<sup>2</sup>, 60 pulse (B) and 3 J/cm<sup>2</sup>, 10 pulse.**

The features etched in quartz at the low laser fluences (shown in Fig 3-33 A) reveal a granulated surface structure, which consist of carbon deposits. Optically smooth etched surfaces are obtained for the intermediate laser fluence range, while at the highest laser fluences the surfaces are tessellated with features, which are probably obtained in a fast melting/boiling and re-solidification processes.

The areas in quartz which are structured by various laser fluences were carefully investigated by Raman Microscopy and X-ray Photoelectron Spectroscopy. These techniques are very sensitive to the chemical surface modification.

Raman spectroscopy is used in condensed matter physics and chemistry to study vibrational, rotational, and other low-frequency modes obtained in various molecules. It relies on inelastic scattering, or Raman scattering of monochromatic light, usually from a laser in the visible, near infrared, or near ultraviolet range. Phonons or other excitations are absorbed by the molecules. The interaction of the molecules with the laser light results in the change of the photon energy of the applied laser light. This shift gives information about the vibrational modes in the molecule and provides chemical structure information of the material.

In our experiments confocal Raman microscope was applied. In a confocal microscope, the parallel laser light is focused to a very small spot on the sample with a microscope objective with a high numerical aperture. The light scattered from the sample is collected and collimated by the same objective and focused into the aperture. The light which is scattered from the focused area can penetrate trough the aperture, while the other scattered

light is blocked by the aperture. This event results in much better resolution as compared to a conventional Raman microscope. The best resolution in our case is  $1\ \mu\text{m}^3$ , which is about 100 times better compared to other Raman microscopes. The Raman spectra of the areas structured in quartz by LIBWE at various laser fluences (shown in Figure 3-33) are shown in Figure 3-34. The areas marked in Figure 3-33 and in Figure 3-34 correspond to: non-structured area marked as 0; the center of the structure obtained at  $3\ \text{J}/\text{cm}^2$  is labeled as 1; the corner and the center of the pattern etched by  $1.5\ \text{J}/\text{cm}^2$  and  $0.8\ \text{J}/\text{cm}^2$  are labeled as 2 and 3, and as 4 and 5, respectively.

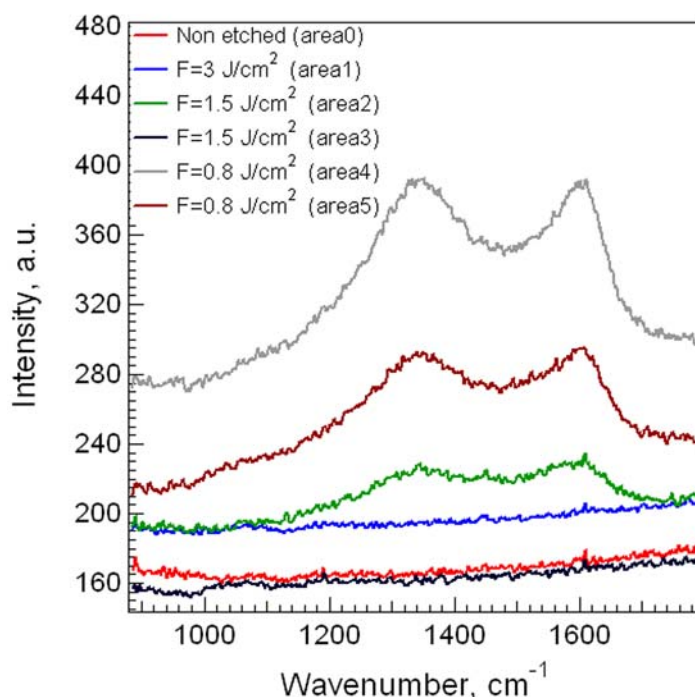


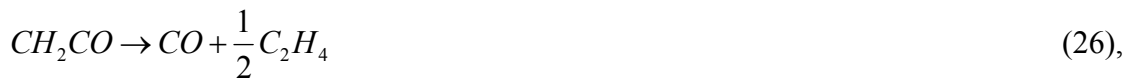
**Fig. 3-34** Raman spectra of the etched areas in quartz by LIBWE using 0.4 M pyrene in acetone solution.

The Raman spectrum of the area structured at  $3\ \text{J}/\text{cm}^2$  is similar to the spectrum obtained for the non-structured area with the slight increase of the baseline. This can be due to an enhancement of the scattered laser light, due to an increase surface roughness. The Raman spectrum measured in the center of the etched feature in quartz at the fluence of  $1.5\ \text{J}/\text{cm}^2$  (marked as *area3*) is similar to the spectrum of the non-ablated surface, while the spectrum of the structure corner etched at the same laser fluence (named as *area2* in Figure 3-34) reveals two Raman bands, i.e.  $1340\ \text{cm}^{-1}$  and  $1600\ \text{cm}^{-1}$ . The intensity of these bands is increasing in the spectrum of the etched areas at the lower laser fluence of  $0.8\ \text{J}/\text{cm}^2$

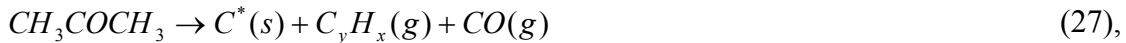
(marked as *area4* and *area5* in Figure 3-34). The Raman peaks at  $1340\text{ cm}^{-1}$  and  $1600\text{ cm}^{-1}$  are assigned to amorphous carbon with a high bond angle disorder and are normally assigned to the carbon *D* and *G* bands [76]. The carbon deposits which are strongly adhering to the quartz surface can therefore be assigned to amorphous carbon. The amorphous carbon is produced during the etching process due to the thermal decomposition of the solution, i.e. acetone and/or pyrene. The mechanism of thermal decomposition (pyrolysis) of acetone is described in the following [61, 77]:



The decomposition reaction of ketene is described as:



Methan ( $\text{CH}_4$ ) and ethene ( $\text{C}_2\text{H}_4$ ) can be decomposed further to solid carbon and gaseous hydrogen. The total reaction of acetone pyrolysis can be described as:



where (s) means solid and (g) gaseous products.

The temperature which is required for the pyrolysis of acetone is 825-940 K [77]. This temperature is easily achieved at the quartz-liquid interface during the LIBWE process.

Another source for the carbon deposits is the thermal decomposition of pyrene. The decomposition of pyrene is also probable, although pyrene is much more stable and can withstand higher temperatures than acetone. The decomposition of pyrene produces the solid carbon deposits and  $\text{C}_y\text{H}_x$  gaseous products, which can also be decomposed to solid carbon and can be described as:



The carbon deposits, as discussed above, play a very important role in the etching process at the low laser fluences. The roughness of the features etched at the low lasers fluences are very high due to the formation of the carbon films which alter the absorption of the laser light and produce an increase of the temperature and pressure jumps and mechanical stress.

Raman microscopy loses its sensitivity if the layer to be analyzed is very thin. Therefore XPS was used for a qualitative analysis of the etched quartz surface by LIBWE. XPS involves the removal of a single core electron with the X-ray radiation, e.g. with the Mg



K $\alpha$  source (1253.6 eV or  $\lambda=1$  nm). The binding energy (BE) which is the characteristic feature of the studied chemical compound can be obtained by measuring the kinetic energy of the ejected core electrons. The penetration depth of XPS is only 0.5-2 nm, which allows us to investigate the surface of the etched quartz and of this deposited carbon layer. The concentration of atomic carbon at the surface of the etched features in quartz by using 0.4 M pyrene in acetone solution examined by XPS is presented in Figure 3-35. Here, the dose is defined as the laser fluence multiplied by the number of the laser pulses.

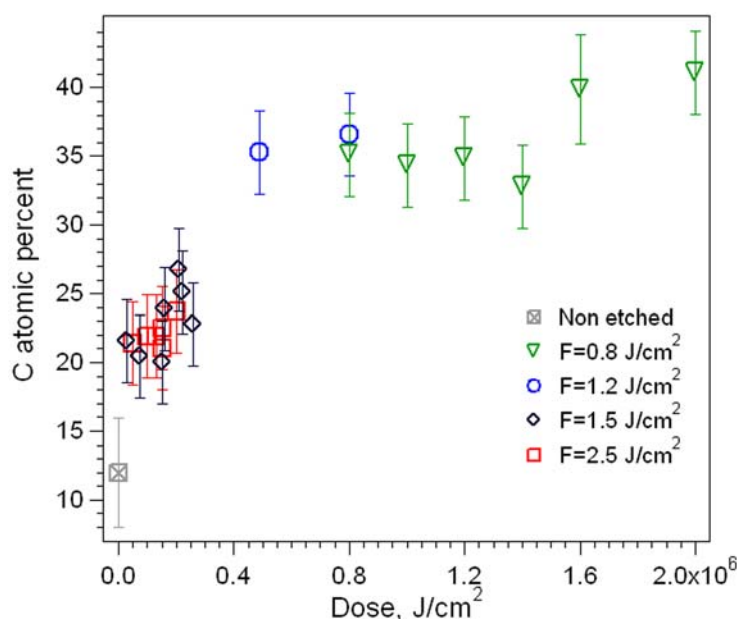


**Fig. 3-35** Concentration of carbon on the surface of the etched areas in quartz by LIBWE evaluated from the XPS measurements.

The concentration of the atomic carbon is higher over the all etched areas, compared to that obtained for the non-structured quartz plate. An enhancement of the carbon concentration on the areas etched with the laser fluences from the intermediate and higher fluence ranges suggest, that the thermal decomposition of the solution occurs over all applied laser fluences. The stronger increase of the amorphous carbon film is, however, observed at the surfaces of the features etched with the low laser fluences.

There are several plausible reasons why carbon films are obtained at the surface of structures etched with the fluences from the intermediate and high fluence range. The formation of the carbon deposits occurs over the all applied laser fluences due to the thermal decomposition of the solution. At the high and intermediate fluence ranges the

etching of quartz starts after several repetitive laser pulses (typical 3 to 5). The carbon films which are created during these incubation pulses are very thin and can be removed from the surface by the pressure jumps. The carbon deposits, however, are strongly adhering on the hot quartz surface when the pressure jump generated by the shock waves is decreasing. This may happen at the first microseconds after the laser pulse. At this time the temperature at the quartz liquid interface is, according to the model described in subchapter 3.1, still high enough to decompose the solvent.

The doses which were used for the structuring of quartz at the high laser fluences are, however, much smaller compared to those which are applied at the low laser fluences. The reason for the enhancement of the dose at low laser fluences is the strong incubation effect. On the other hand, only a limited amount of laser pulses can be applied at the high laser fluences, due to the possibility of the breaking the quartz sample. Despite the fact, that the doses for the low and high laser fluences are different, one could conclude, that the amount of atomic carbon obtained on the surface of the etched areas at the low laser fluence is higher compared to that observed at the intermediate and high laser fluences.

### ***3.6 Surface analysis of etched areas in quartz: chemical structural change.***

The fast melting, high pressures and the quick solidification processes during LIBWE can create structural changes inside the materials, which will be discussed in this subchapter.

Quartz reveals several phase transitions which are created during the slow heating of fused silica [78]. The transition from the  $\alpha$ -quartz (most popular quartz phase at room temperature and atmospheric pressure) to  $\beta$ -quartz occurs at 573 °C and at atmospheric pressure. The transition from the  $\beta$ -quartz to the high pressure (HP) tridymite phase is observed at 867 °C. This quartz phase exist for temperatures up to 1470 °C. This phase is followed by the  $\beta$ -cristabolite which is stable up to the melting point of quartz (1727 °C). In the case of the laser assisted wet etching process the temperature increase is extremely fast (up to  $10^9$  °C/s), which make it extreme difficult to detect the phase transitions of quartz during the laser heating. The most important question is related to the solidification process. At the conventional cooling rates (100 °C/min) quartz stabilizes in the  $\alpha$ -quartz phase, however, metastable silica phases are also common. For instance, both cristabolite and tridymite phases occur as metastable modifications at room temperature. The different

phases of quartz have a unique bond energy and the bonding angle between the silicon and the oxygen atoms. The structural changes of silica in the etched areas by LIBWE are also investigated by XPS. The XPS spectra of the Si 2p binding energy at various laser fluences are shown in Figure 3-36.

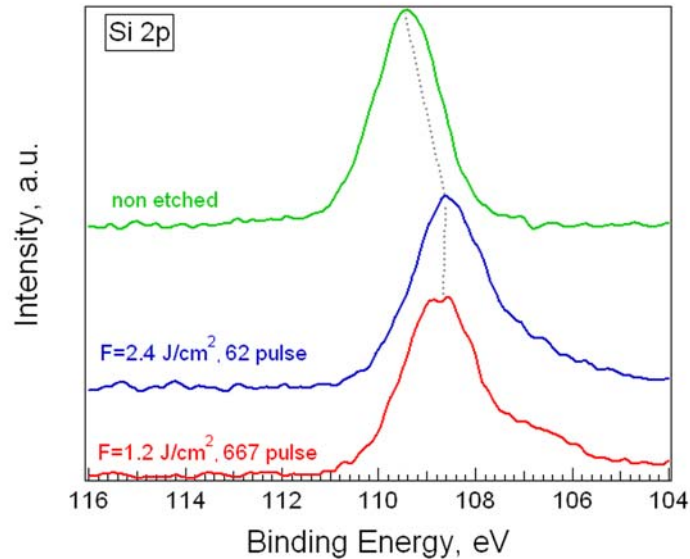


**Fig. 3-36 Si 2p spectra of the etched areas in quartz by LIBWE.**

The shift of the Si 2p peak to the lower binding energies suggests that structural changes of quartz during the LIBWE process occur. The results of the binding energies changes for different Si/O stoichiometries have been published [79, 80]. This shift is probably associated with a reduction of the oxygen content [79, 80].

The atomic oxygen to silica ratios of the etched areas in quartz by LIBWE at various laser fluences and numbers of laser pulses are shown in Figure 3-37.

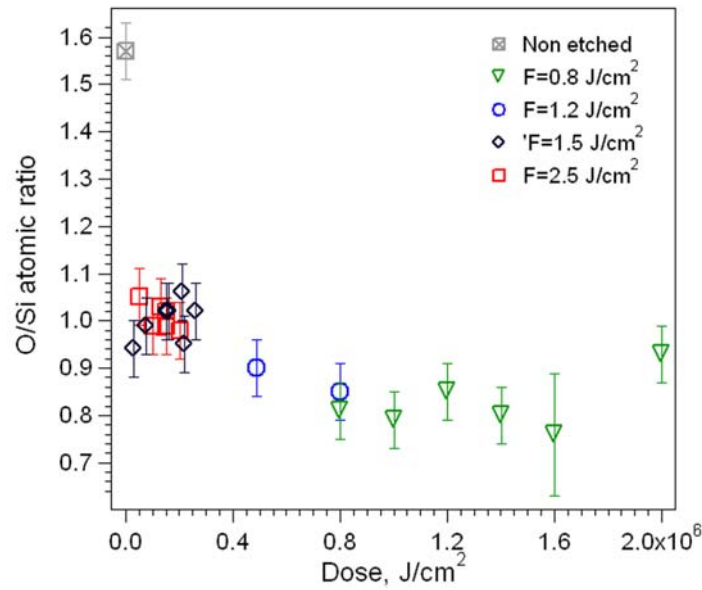


**Fig. 3-37. O/Si atomic ration of quartz structured by LIBWE.**

The O/Si ratio is strongly decreasing over all applied laser fluences (shown in Figure 3-37). The structures, etched with the low laser fluences, reveal a more pronounced reduction of the oxygen content, compared to the structures which are etched at the intermediate and high laser fluences. The decrease of the O/Si ratio at the low laser fluence may be associated with the formation of the carbon deposits on the quartz surface, while the different quartz polymorphs can be created at the high laser fluences. The various quartz polymorphs, as discussed above, consist of a various number of SiO<sub>4</sub> tetrahedral units which are joined together via Si-O-Si bonds. The bond angles depend on the configuration of the polymorphs and can be in the range from 143 degrees (e.g.  $\alpha$ -quartz) to 180 degrees (e.g. HP-tridymite), as illustrated in Figure 3-38.

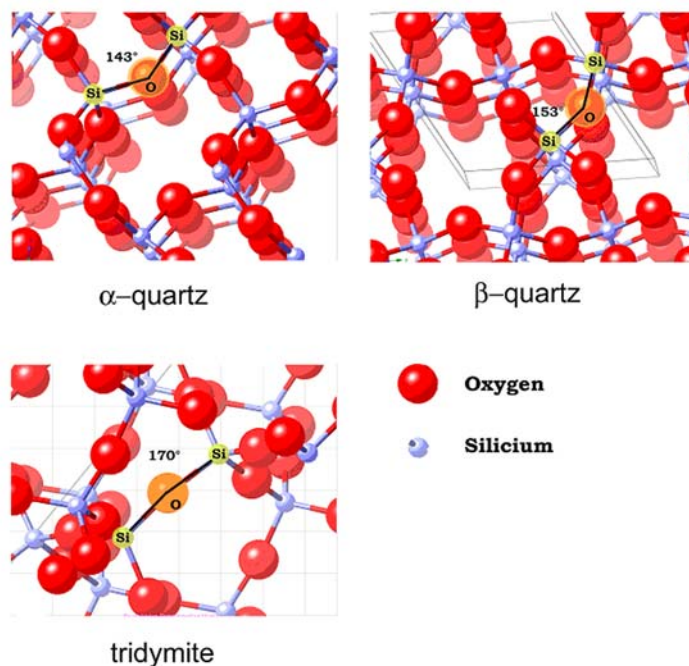


**Fig. 3-38. The structure of different quartz polymorphs.**

The highest density from all quartz polymorphs has  $\alpha$ -quartz. The  $\beta$ -quartz is less dense, but has a higher symmetry, compared to  $\alpha$ -quartz. The change in the symmetry results in an increase of the bond angle, which is enhanced from 143 degrees ( $\alpha$ -quartz) to 153.4 degrees ( $\beta$ -quartz). The tridymite and cristobalite phases of quartz have very high symmetry and therefore much larger Si-O-Si bond angles. They are also less dense compared to  $\alpha$ -quartz (as also shown in Figure 3-38). The change of the bond angle of silica is reflected in the Si 2p XPS spectrum. A clear trend of the shift in the binding energy of the Si 2p peak measured at various areas in the structured quartz can not be detected. This is due to the strong charging of fused silica surface which shifts the Si 2p peak randomly to lower binding energy values, resulting in misinterpretation of the measured results. Therefore, the binding energy difference between Si 2p and O 1s was analyzed. The binding energy of O 1s shifts in the same direction as the Si 2p peak due to the charging of the silica surface. The analysis of the binding energy difference between Si 2p and O 1s leads to the more reasonable results. The O1s-Si2p binding energy differences of the etched areas in quartz by LIBWE are shown in Figure 3-39.

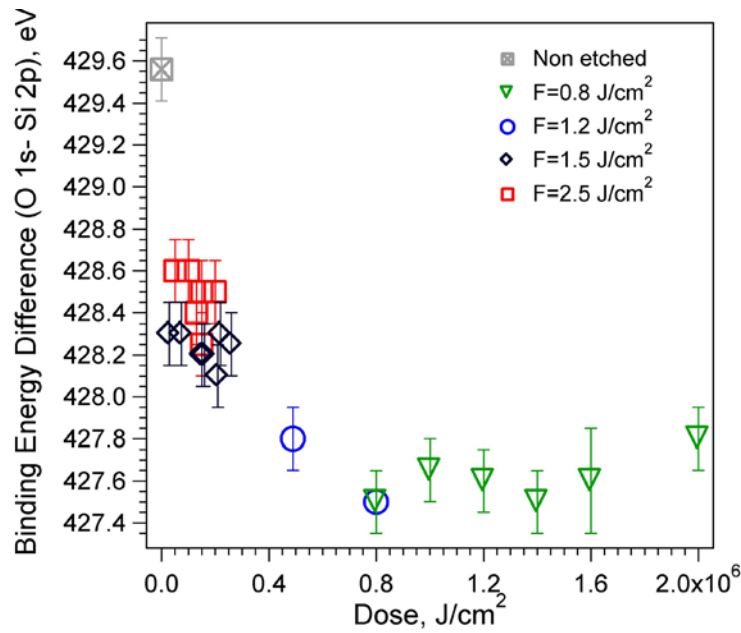


**Fig. 3-39.** The (O1s-Si2p) binding energy difference of the etched areas in quartz by LIBWE.

The change of the (O1s-Si2p) binding energy difference by -1.8 eV between the etched areas and non-structured quartz surface could correspond to an increase of the Si-O-Si angle from 144 to 170 degrees [80]. The XPS analysis of the etched areas suggests the chemical changes of the structured surface in this layer. Another method for the qualitative chemical analysis of a material is *Infrared Spectroscopy*, but only very thin silica layers ( $\approx 10 \mu\text{m}$  thickness) can be analyzed by conventional IR absorption spectroscopy due to the high absorption of quartz in the IR.

A new technique for the diagnostic of tissues was developed by Heise et al. [81]. This method has been termed as *Fiber Tip Attenuated Total Reflection -FTIR Spectroscopy*. The key element in this approach is a flexible silver halide optical fiber, which is coupled with a *Fourier Transform Infrared* (FTIR) spectrometer. The optical fiber probe has a shaft containing one fiber for transmitting and one fiber for receiving the infrared radiation. These two fibers are connected with the short U shaped silver halide fiber. This U shaped fiber is attached to the surface of the etched area in quartz. The schematic of the ATR measurement system is described in details elsewhere [81]. Due to the higher penetration depth of the IR ( $\approx 5 \mu\text{m}$  for silica) in ATR spectroscopy, the chemical composition is obtained for a 1000 times thicker quartz layer as compared to the XPS measurements. The ATR IR spectra of the features etched in quartz by LIBWE at low laser fluences ( $0.8 \text{ J/cm}^2$

and  $1.2 \text{ J/cm}^2$ ) are shown in Figure 3-40. The number of applied laser pulses was selected in a way that the irradiation dose will be equal for both laser fluences.

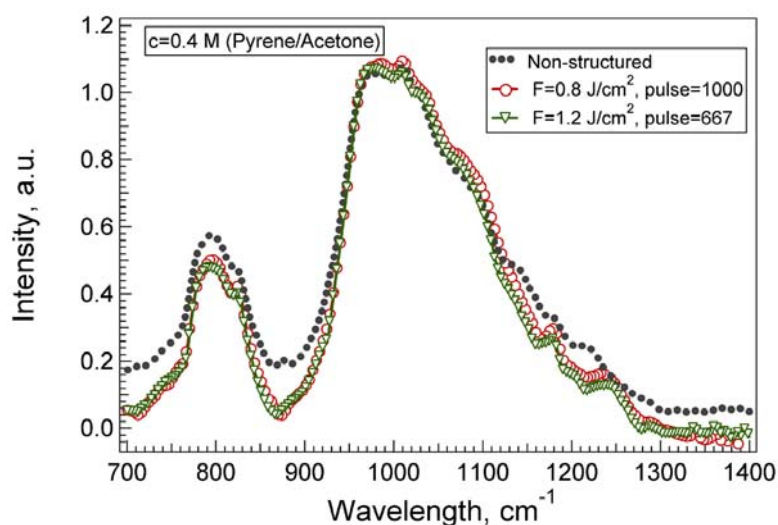


**Fig. 3-40 ATR IR spectra of the etched areas in quartz by LIBWE at the low laser fluences.**

The IR spectra of quartz structured at the low laser fluences are similar to that obtained for the non-structured area. The IR spectrum provides, as discussed above, the information about the chemical composition of quartz over 5 micrometer thick layer. The similar IR spectra obtained for the non-ablated area and for the features etched with the low laser fluences (shown in Figure 3-40) suggest that there is no structural changes within this quartz layer, although XPS measurements indicated clear chemical modifications at the quartz surface.

The shape of the IR spectra around the main peak ( $1000 \text{ cm}^{-1}$ ) of the features etched in quartz with fluences from the intermediate and high fluence ranges (shown in Figure 3-41) are different compared to the IR spectra obtained from the non-structured areas.

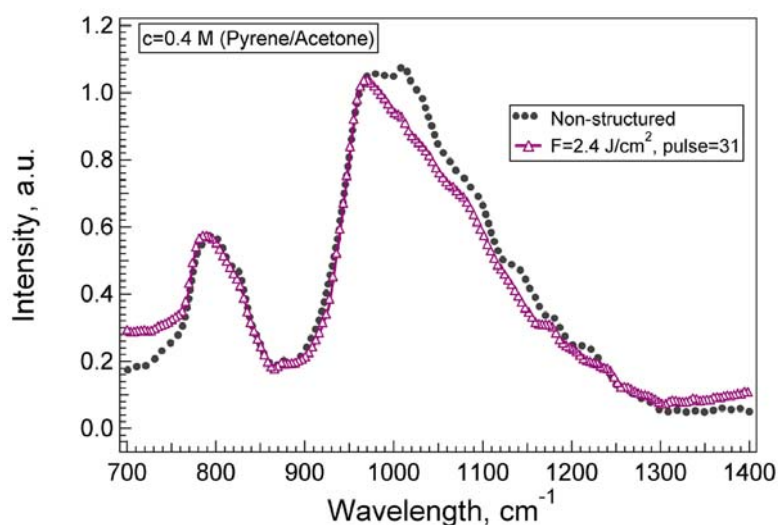


**Fig. 3-41 ATR IR spectra of the etched areas in quartz by LIBWE at the intermediate and high laser fluences.**

The differences in the shape of the main IR peak (at  $1000\text{ cm}^{-1}$ ) between the areas structured with the fluences of  $1.5\text{ J/cm}^2$  (do not shown) and  $2.4\text{ J/cm}^2$ , and the non-structured areas suggest the existence of chemical modification in the quartz bulk. This difference can be assigned to changes in quartz phases, i.e. from  $\alpha$ -quartz to tridymite. The latter phase of quartz can be created during fast melting and solidifying processes, which take place in LIBWE process.

The main difference between the non-structured  $\text{SiO}_2$  and etched areas with the intermediate and high fluences is the absence of the features around the main peak (marked in the Figure 3-41). Similar differences at the  $1100\text{ cm}^{-1}$  between  $\alpha$  quartz and tridymite is also clearly visible in the reference IR absorption spectra (shown in Figure 3-42) [78, 82].



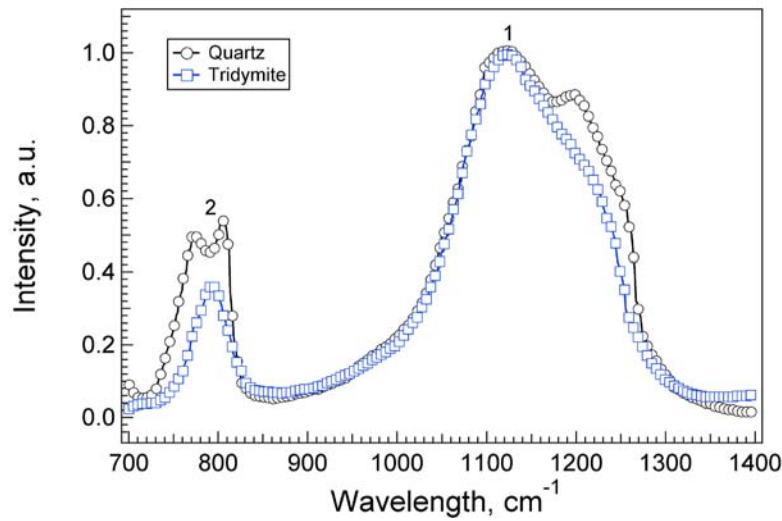


**Fig. 3-42. IR absorption reference spectra of  $\alpha$ -quartz and tridymite phases [78, 82].**

The spectra of the quartz and the tridymite reveals three major absorption bands (marked as 1 and 2 in Figure 3-42), which are assigned to the asymmetric Si-O stretching ( $\sim 1100\text{ cm}^{-1}$ ) band, the asymmetric distortion of the  $\text{SiO}_4$  tetrahedra ( $\sim 803\text{ cm}^{-1}$ ). The difference in the IR spectra between the  $\alpha$  quartz and tridymite is associated with the changes of asymmetric stretching of Si-O and asymmetric distortion of the tetrahedral. Similar differences are also detected in the ATR IR spectra of the non-etched and the samples etched at high fluences areas at  $1050\text{ cm}^{-1}$  and  $800\text{ cm}^{-1}$  (shown in Figure 3-41). The IR spectra obtained for our samples and reference spectra reveal a difference in the  $1100\text{ cm}^{-1}$  range. The shift of the fundamental Si-O absorption frequency from  $1100\text{ cm}^{-1}$  for the reference spectra (shown in Fig. 3-42) to  $1000\text{ cm}^{-1}$  (shown in Fig. 3-41) of our samples can be related to the different types of  $\alpha$ -quartz and a different number of intrinsic impurities (e.g. OH). Nevertheless, it is still possible to compare the shapes of the spectrum of tridymite (shown in Figure 3-42) with the IR spectrum of the etched areas at the high laser fluences (shown in Fig. 3-41). The similar shapes of the spectrum shown in Figure 3-41 and Figure 3-42 for tridymite, suggest that  $\alpha$ -quartz is changing to the tridymite quartz phase during the LIBWE process at laser fluences above  $1.5\text{ J/cm}^2$ .

### ***3.7 High fluence range: plasma assisted wet etching?***

The laser induced temperature at the quartz-liquid interface reaches  $4000\text{ K}$  and more at laser fluences above  $2\text{ J/cm}^2$ , as discussed in subchapter 3.1. This may result not only in

the boiling of the quartz surface, but also in the generation of a plasma in solution. This plasma consists of excited Si neutral atoms, which are generated from quartz, excited C and H ions which are created from the solution. A plasma in quartz without solution can also be created in the direct laser ablation process by a XeCl excimer laser at laser fluences of  $\geq 15 \text{ J/cm}^2$ . The spectrum of the plasma emission can be detected experimentally. An experimental setup for the creation and measuring the plasma emission is shown in Figure 3-43.

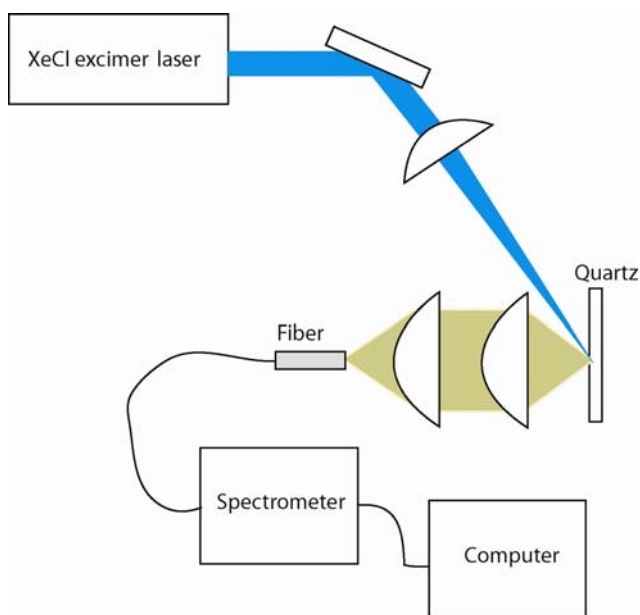


**Fig.3-43 The experimental setup for the generation of a plasma in quartz and measuring its emission features.**

A XeCl excimer laser was used as irradiation source. The beam of this laser is focused on the quartz surface using a 250 mm focal length lens. The plasma emission is collected into the optical fiber by using two quartz lenses with focal lengths of 100 mm. The spectrum of the plasma emission was analyzed with a time gated spectrometer. This spectrum is used as reference for the plasma emission spectra obtained in the LIBWE process at laser fluences above  $2 \text{ J/cm}^2$ .

The spectrum of plasma emission created by LIBWE at the quartz-liquid interface can also be measured using the same experimental setup with the difference that laser light is focused on the backside of the material which is in contact with the solution. The spectra of the plasma emission obtained by direct XeCl excimer laser ablation of quartz and by LIBWE are shown in Figure 3-44.

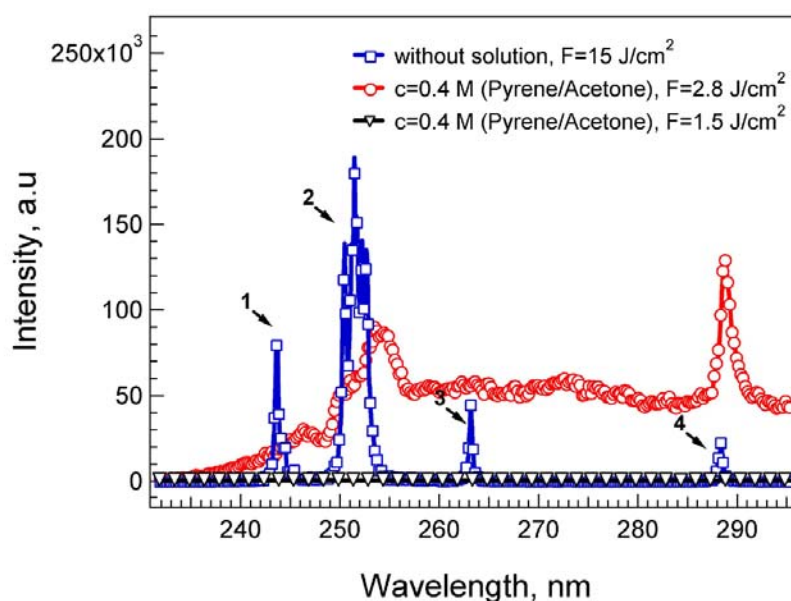


**Fig. 3-44 Plasma emission spectra of quartz ablated by XeCl excimer laser without and with solution at different laser fluences.**

The emission lines located at 244, 251, 263 and 288 nm (marked in Fig. 3-44 as 1-4) are assigned to excited neutral Si atoms [68, 83]. The plasma emission spectrum obtained by LIBWE at a fluence of  $2.8 \text{ J/cm}^2$  with 0.4 M pyrene in acetone solution is different to that observed for the dry etching of quartz. The very broad emission line starting from 240 nm can be assigned to Bremsstrahlung radiation in solution, which is due to the acceleration of the charged particles (electrons, ions and etc.). The Bremsstrahlung emission has a continuous spectrum [84]. Beside this broad emission line, the two emission peaks located at 255 nm and at 289 nm are clearly visible. The peak at 289 nm corresponds well with that obtained for the dry ablation of quartz and can be assigned to emission line of the excited neutral Si atoms. It is also important to notice, that the excited carbon or the hydrogen atom (major components of the plasma in the solution) provides no plasma emission at this wavelength range. This leads to the conclusion, that the peak obtained at 289 nm can be assigned to the excited neutral Si atom. No plasma emission is visible at the quartz-liquid interface irradiated with  $1.5 \text{ J/cm}^2$  (shown in Figure 3-44).

The threshold of the plasma emission of the excited neutral Si atom in quartz by LIBWE was obtained experimentally by measuring the intensity of the peak at 289 nm as shown in Figure 3-45.

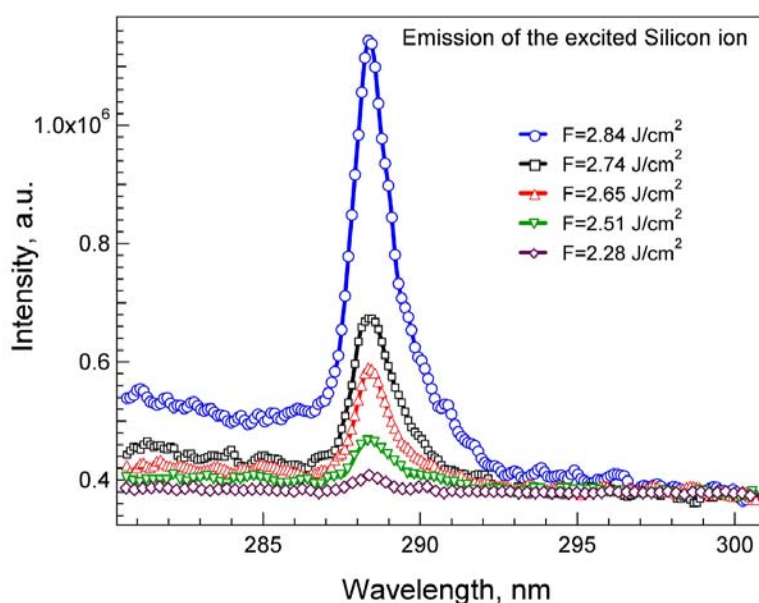


**Fig. 3-45. Emission of the excited neutral Si atom of quartz by LIBWE at various laser fluences.**

The intensity of the plasma emission peak at 289 nm strongly depends on the laser fluences (shown in Figure 3-45). The enhancement of the laser fluence results in the increase of the plasma emission peak intensity. The lowest laser fluence below which no plasma emission in solution is obtained is assigned to the plasma emission threshold fluence. This threshold is obtained at  $2.1 \text{ J/cm}^2$ . The value of this threshold fluence coincides quite well with the change of the etch rates behavior, assigned as high laser fluence range and is marked in Figure 3-32 as *C*. This observation suggests, that the plasma process assists the etching mechanism at laser fluences above  $2.1 \text{ J/cm}^2$ . The increase of the etch rate at the high laser fluence can be related to the increase of the temperature at the thin interface between the liquid and quartz. This results in an increase of the molten layer of the quartz surface. The creation of plasma in solution process results in a number of effects, such as an enhancement of the pressure jump, generation of the optical defects inside the material, which can increase the absorption of UV light of quartz. These effects may result in increase of the etch rates and etch roughness and also may explain the breaking of quartz when more than 200 repetitive laser pulses are applied at this fluence range.

### ***3.8 Influence of organic solvents on the LIBWE process.***

The quality of the etched features in quartz depends on many different parameters. In this subchapter studies on the etch rates, etch roughness and number of incubation pulses are presented for various etching solutions. This is important for the fabrication of micro-optical elements in quartz by LIBWE. However, in all of the studied solutions pyrene was utilized as absorber. The 0.4 M pyrene in acetone solution, which was applied in the previous experiments, was suggested by the developers of the LIBWE technique. However, this is the maximum amount of pyrene which could be dissolved in acetone. In order to increase the concentration of pyrene in solution tetrahydrofuran (THF) was selected as solvent. The physical properties, i.e. density, molar heat capacity, boiling temperature of THF are similar to that of acetone (are summarized in Table 3). However, the solubility of pyrene in THF as solvent is much higher.

**Table 3.** Thermodynamic properties of acetone and THF [68]

	Density, kg/m <sup>3</sup>	Molar heat capacity, J/mol·K	Boiling temperature, °C
Acetone	789	123.8	60
THF	880	123.5	70

The etch rate, etch roughness and number of incubation pulses of quartz using a 0.4 M pyrene in THF solution are measured using the same procedures as described in subchapter 3.4. The experimental results for pyrene in acetone and pyrene in THF with equal concentrations are shown in Fig. 3-46 A, B and C.

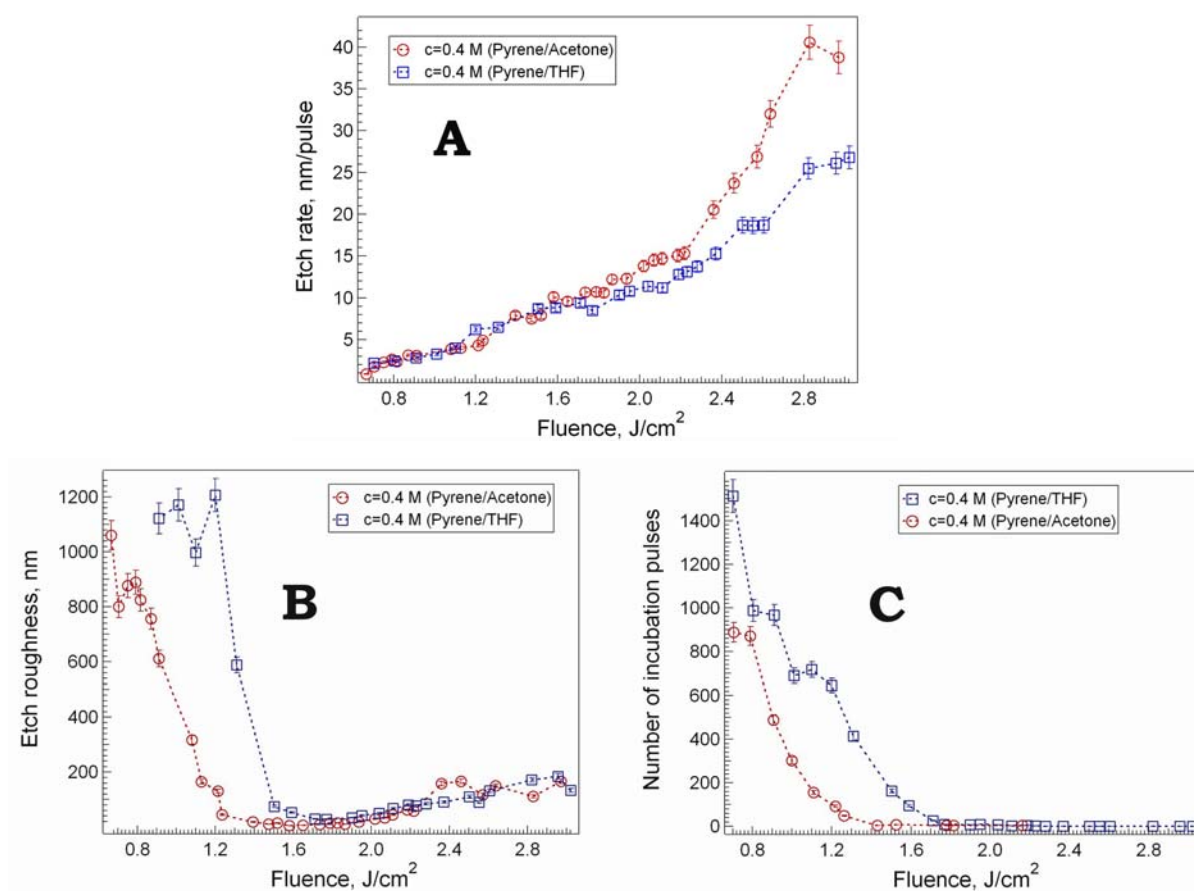


**Fig. 3-46 Etch rate (A), etch roughness (B) and number of incubation pulses (C) of quartz by LIBWE at 0.4 M pyrene in acetone and in THF.**

The etch rates of quartz obtained for both solutions are similar within the fluence range of 0.7 J/cm<sup>2</sup> to 2 J/cm<sup>2</sup> (low and intermediate fluence ranges). However, at the higher laser fluences (above 2 J/cm<sup>2</sup>) the etch rate of quartz obtained with the 0.4 M pyrene in THF solution is lower compared to the results observed for the pyrene in acetone solution. This could be explained by the different plasma formation mechanisms which assists the etching process at these fluences and enhancement of the direct laser light absorption by the acetone. Although the etch rate at the fluences below 1.6 J/cm<sup>2</sup> are similar for both solvents, the roughness of the etched areas in quartz (shown in Figure 3-46 B) and number of incubation pulses (shown in Figure 3-46 C) are different. The etch roughness of quartz by LIBWE using 0.4 M pyrene in THF solution are increasing at laser fluences which are below 1.5 J/cm<sup>2</sup>. At this fluence range (named for 0.4 M pyrene in acetone solution as intermediate fluence range) the roughness of the etched areas in quartz using 0.4 M pyrene

in acetone solution are  $\leq 20$  nm and start to increase when the laser fluences are below  $1.2 \text{ J/cm}^2$ . A similar behavior is obtained for the incubation effect: the number of the laser pulses required to start the etching process increases above a fluence of  $1.6 \text{ J/cm}^2$  when THF is used as solvent, while for the acetone solution an increase of the incubation pulses is obtained for fluences  $\leq 1.2 \text{ J/cm}^2$ .

An increase of the etch roughness and number of incubation pulses is associated, as discussed above, with the decomposition of the solution and generation of carbon deposits which influence the etching process. The low etch roughness and number of incubation pulses may suggest that the light is also absorbed by the acetone and therefore enhances the temperature and pressure jump required for smooth structuring of the quartz plate.

The low etch roughness and number of incubation pulses obtained for 0.4 M pyrene in acetone solution makes it more useful for the production of high quality structures in quartz by LIBWE, as compared to 0.4 M pyrene in THF solution.

Nevertheless higher concentrated pyrene in THF solutions may be advantage to use, as the higher concentration of the absorbers in solution will result in a thinner absorption layer. The temperature jump will increase linearly, according to the model described in the subchapter 3.1, with an increase of the pyrene concentration in solution. For instance the maximum evaluated temperature jump at  $1.5 \text{ J/cm}^2$  for 1 M pyrene in THF solution is 6000 K, which is 2.5 times higher than that obtained for 0.4 M pyrene in acetone solution. The higher absorption of the solution and the higher temperature jump at the quartz-liquid interface which are obtained with an increase of the concentration of pyrene should therefore result in an increase of the etch rates and a shift of the "best" etching behavior to lower laser fluences. Also a decrease of the threshold fluence and number of the incubation pulses may be observed. The etch rates, etch roughness and the number of incubation pulses of quartz by LIBWE using highly concentrated pyrene solutions at various laser fluences are shown in Figure 3-47 A, B, and C.

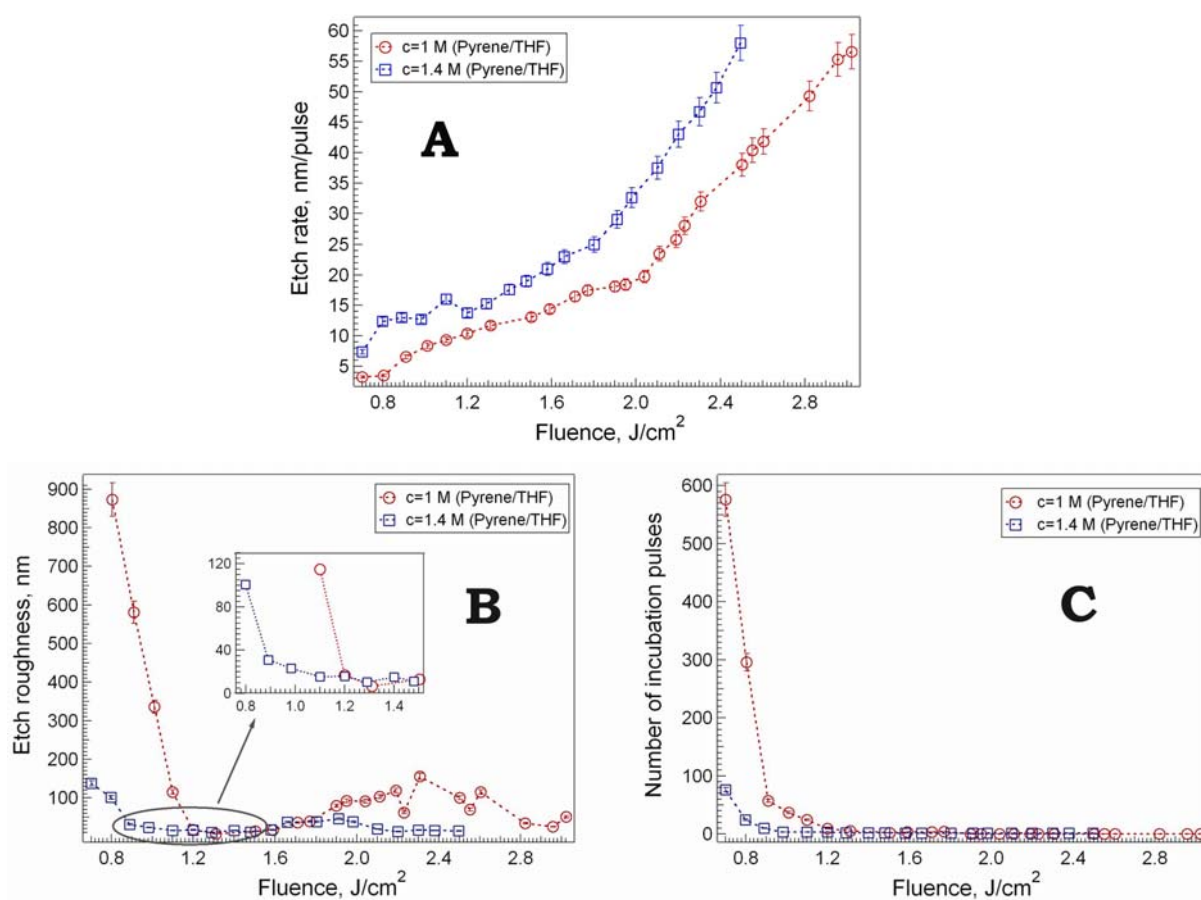


**Fig. 3-47 Etch rate (A), etch roughness (B) and number of incubation pulses (C) of quartz by LIBWE using 1 M and 1.4 M pyrene in THF solution.**

The etch rates of quartz increases with an increase of the pyrene concentration. This can be explained by the fact, that the laser energy is deposited in a thinner layer at the quartz-liquid interface compared to the 0.4 M solution, which leads to an increase of the volumetric temperature jump. An increase of the temperature jump causes melting of quartz occurring at much lower laser fluences compared to the 0.4 M pyrene in THF solution. The much lower etch roughness and number of incubation pulses obtained for higher concentrated solutions can also be related to the enhancement of the T-jump and P-jump.

The lowest etch roughness of quartz by LIBWE of  $\leq 40$  nm within the fluence range of 0.8-1.6 J/cm<sup>2</sup> is obtained for the 1.4 M pyrene in THF solution. *This is the best result achieved for quartz by LIBWE in these studies.* The number of the incubation pulses obtained for this solution and this fluence range is below 40 pulses. *The 1.4 M pyrene in*



*THF solution and the fluences from 0.8 to 1.6 J/cm<sup>2</sup> were therefore selected for the fabrication of complex structures with continuous profiles in quartz.*

### 3.9 Influence of the excitation wavelength on LIBWE processing.

A KrF excimer laser (248 nm, 25 ns) as irradiation source and a 0.4 M pyrene in acetone solution were used in the first experiments for structuring of quartz by LIBWE [31, 46]. The reasons for changing to the XeCl excimer laser in our studies are related to the better XeCl excimer laser beam profile and reduction of the operational cost.

It is nevertheless also interesting to investigate the etching of quartz by a KrF excimer laser and to compare the results with those obtained for the XeCl excimer laser. The etch rate, etch roughness and number of incubation pulses for quartz by LIBWE for XeCl and KrF excimer laser are shown in Figure 3-48 A, B and C.

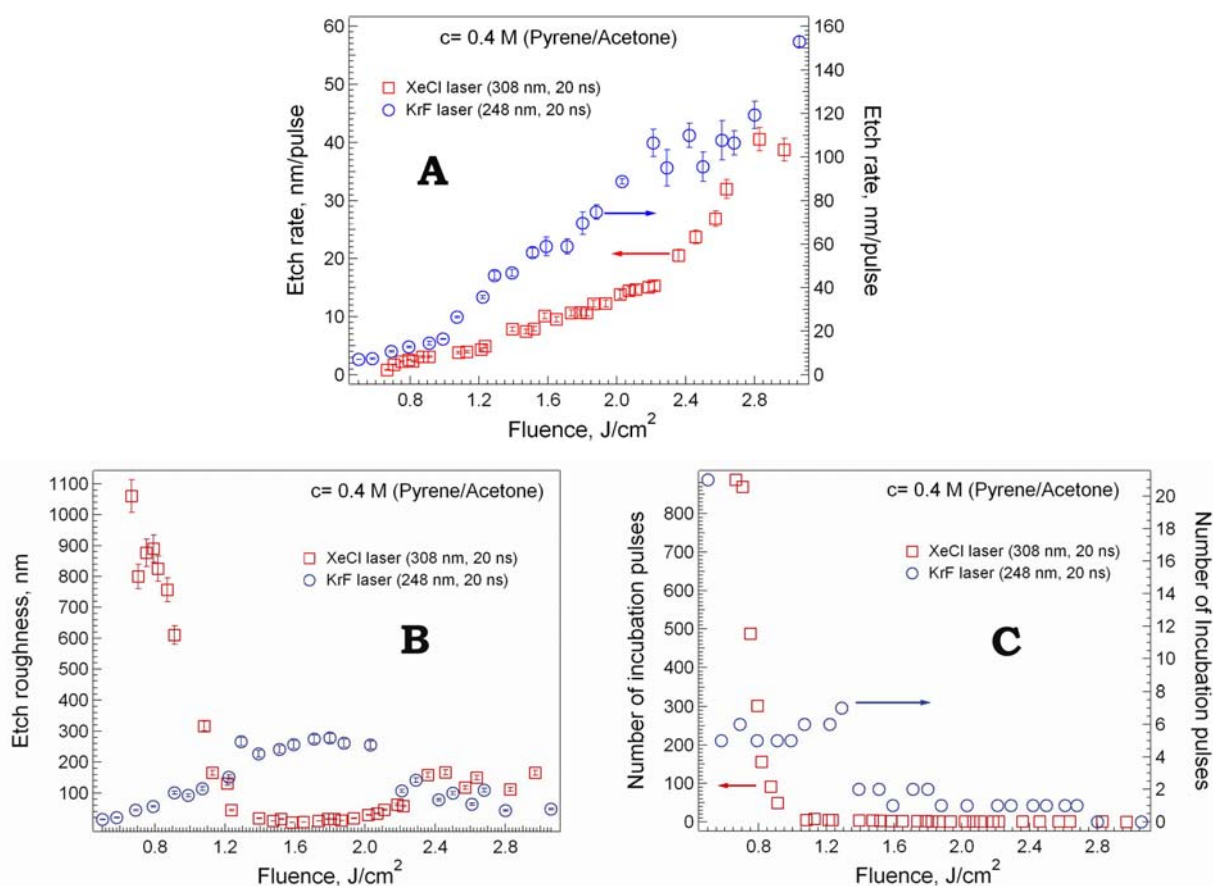


**Fig. 3-48** Etch rate (A), etch roughness (B) and number of incubation pulses (C) of quartz by LIBWE using KrF (248 nm) and XeCl (308 nm) excimer lasers.

The etch rates of quartz by LIBWE with the 248 nm laser pulse is 3 times higher compared to that obtained for the 308 nm laser, although the absorption coefficients of 0.4 M pyrene in acetone solution are comparable (as shown in Figure 3-2). The reasons why the etch rates and threshold fluence are lower for 248 nm compared to 308 nm are not yet clear. The theoretical modeling of the temperature jump, which is described in subchapter 3.1 gives similar temperature rises for both irradiation wavelengths. The increase of the etch rates by using the 248 nm irradiation may be related to the different photothermal mechanism of the solution or formation of plasma in solution at much lower laser fluences. These processes, however, were not investigated in detail in this work.

The etch rate slopes obtained for quartz by applying KrF excimer laser reveals only a two slope behavior, which is again different compared to the observation obtained with the XeCl excimer laser. The small plateau at the fluence range of 2.2-2.5 J/cm<sup>2</sup> (shown in the Figure 3-48 A at 248 nm) may be a sign for a change of the etching mechanisms, but more studies must be performed to confirm this possibility. The roughness of the etched areas (shown in Figure 3-48 B) using the KrF excimer laser reveals completely different features compared to those that are obtained by the application of the XeCl excimer laser. The etch roughness for 248 nm irradiation is increasing with an increase of the laser fluences, and is reaching a maximum value of 280 nm at a fluences of 1.6 J/cm<sup>2</sup>. At fluences above 2 J/cm<sup>2</sup> the roughness of the etched areas is decreasing again. The lowest etch roughness  $\leq 50$  nm of quartz structured by using the KrF excimer laser is obtained only for very small fluence ranges from 0.6 J/cm<sup>2</sup> to 0.8 J/cm<sup>2</sup> and for 2.5 J/cm<sup>2</sup> to 3 J/cm<sup>2</sup>. At the intermediate fluence range (1.4 to 2.1 J/cm<sup>2</sup>), where the lowest etch roughness with 308 nm irradiation is obtained, the maximum roughness is observed for 248 nm irradiation. The number of incubation pulses required for etching at 248 nm is much lower compared to 308 nm. Furthermore, the formation of carbon deposits which are deposited at the quartz surface during the etching is less pronounced in the case of 248 nm. Higher etch rates and very low number of incubation pulses suggests the KrF excimer laser as an alternative laser source for the structuring of quartz at the fixed laser fluences, however, for the fabrication of 3D structures in quartz a XeCl excimer laser is more applicable.

### ***3.10 Influence of the laser pulse length on LIBWE processing.***

The increase of the temperature at the quartz-liquid interface is related, as discussed in the subchapter 3.1, to the multi-photonic absorption and the fast relaxation processes. The cyclic absorption process will depend on the laser pulse length. The longer laser pulses can generate more cycles of absorption and non-radiative relaxation processes in solution, which should lead to an enhancement of the temperature jump. On the other hand, the photon flux (number of the photons per area and per unit time) is higher for the short laser pulses which will also result in the excitation of a higher number of pyrene molecules.

There are two important reasons to study the LIBWE processes at different laser pulse length: for a better understanding of the LIBWE process and for the possible applications of other lasers for structuring of UV transparent materials by LIBWE.

A XeCl excimer laser developed by SOPRA, which provides 12 J per pulse at 308 nm, was used as irradiation source. This laser was tested because of the high energy per pulse and a very homogeneous beam profile. This laser was checked as an alternative source for the possible fabrication of large scale micro-lenses with the diameters of up to several millimeters. The pulse length of this laser is 200 ns. The etching parameters of quartz by LIBWE using XeCl excimer lasers with two different pulse lengths (30 ns (FWHM of the first laser peak intensity) and 200 ns) and 1.4 M pyrene in THF solution are shown in Figure 3-49. The area of the structures etched in quartz was kept the same for both XeCl excimer lasers and was 1.2x1.2 mm.

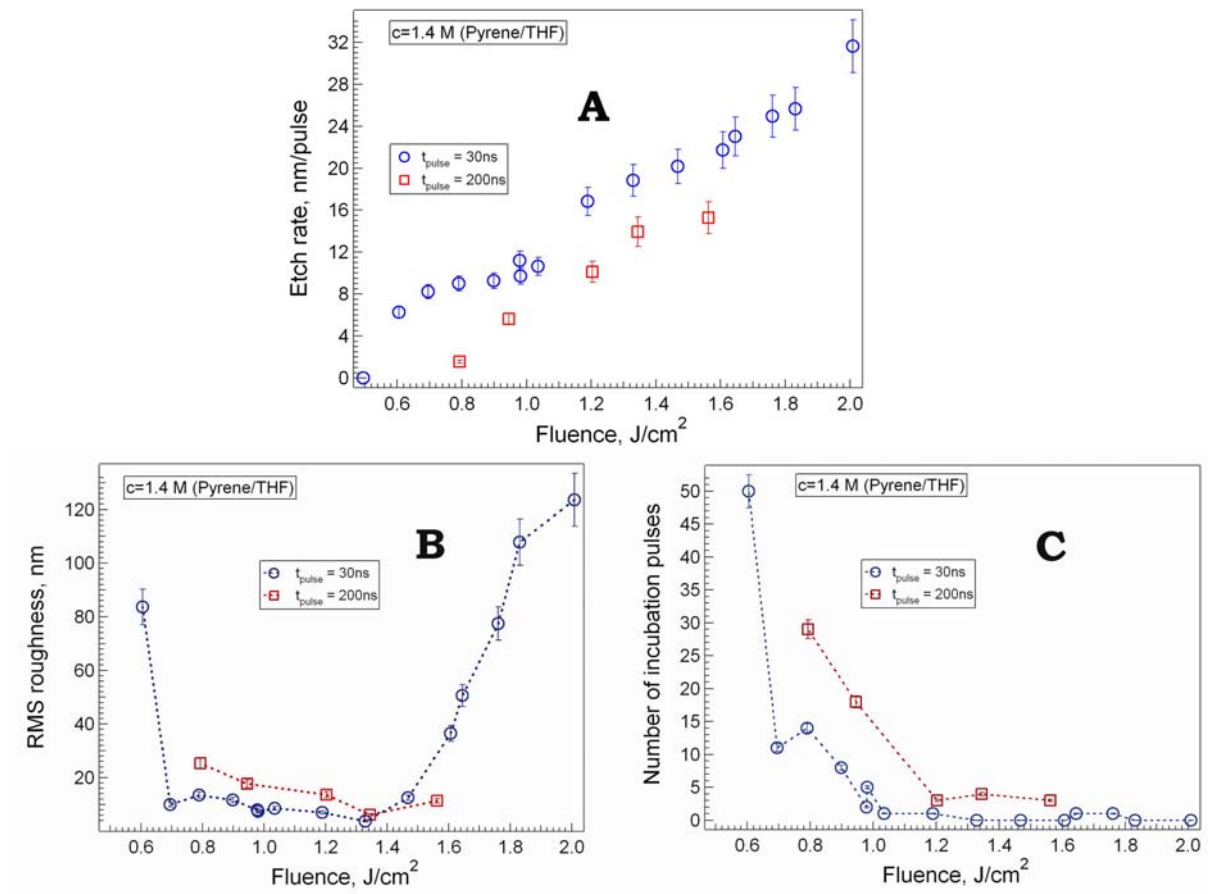


**Fig. 3-49 Etch rate (A), etch roughness (B) and number of incubation pulses (C) of quartz by LIBWE using XeCl (308 nm) excimer laser with different pulse length.**

The threshold fluence obtained for the 200 ns pulse is  $0.8 \text{ J/cm}^2$  and is much higher than that measured for the 30 ns laser pulse ( $0.5 \text{ J/cm}^2$ ). The etch rates of quartz using the longer laser pulse is clearly lower compared to those obtained for the shorter laser pulses. The number of incubation pulses (shown in Fig. 3-49 C) for the longer laser pulse is also higher. These observations suggest that a lower temperature jump at the quartz -liquid interface is created for long laser pulses. The temperature rise at the interface between the quartz and liquid evaluated by the theoretical model, suggests that the decrease of the laser pulse duration causes an increase of the laser induced temperature rise. The peak temperature at the quartz-liquid interface evaluated for a 30 ns laser pulse at  $1.2 \text{ J/cm}^2$  laser fluence is slightly above the melting point of quartz [ $\sim 2000 \text{ K}$ ], while the T-jump calculated for 200 ns pulse is 500 K lower. The etching mechanism at the high laser

fluences for 200 ns laser pulses may be different, however more experimental data are necessary to confirm the etch rate behavior with the long laser pulse.

The surface of the features etched with the 30 ns and 200 ns XeCl excimer laser pulses and a laser fluence of  $1.6 \text{ J/cm}^2$  were examined with confocal Raman microscopy (shown in Figure 3-50).

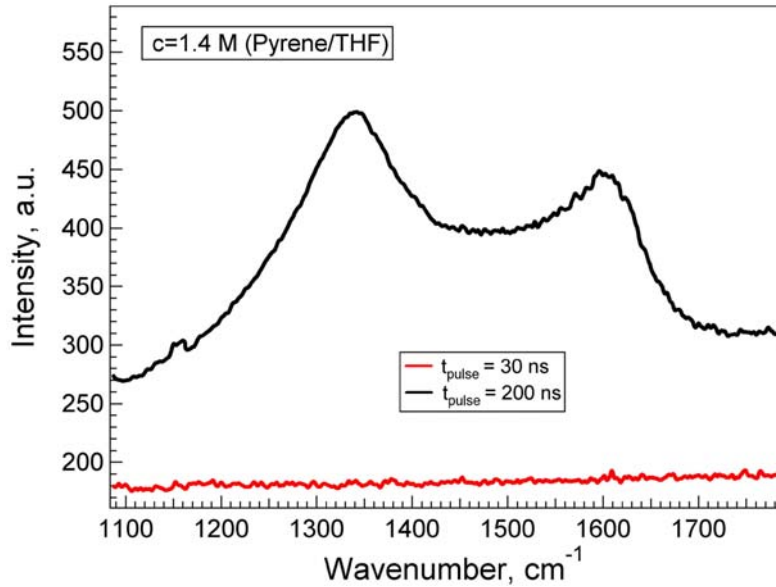


**Fig. 3-50. Raman spectra of quartz etched by LIBWE for 30 ns and 200 ns laser pulse ( $F=1.6 \text{ J/cm}^2$ , 20 pulse) illustrating the carbon-associated D and G peaks at  $1340 \text{ cm}^{-1}$  and  $1580 \text{ cm}^{-1}$  respectively [76]**

The G and D bands of the amorphous carbon are clearly visible in the Raman spectrum for quartz structured with the 200 ns laser pulses, while no carbon deposits can be detected for the 30 ns laser pulse. This indicates, that the etching mechanism for 200 ns laser pulse is strongly influenced by the formation of carbon deposits. This observation suggests, that the etching mechanism of quartz structured with the long laser pulses for laser fluences from  $0.8$  to  $1.6 \text{ J/cm}^2$  is similar to that obtained for the 30 ns laser pulse at laser fluences from  $0.6 \text{ J/cm}^2$  to  $1.2 \text{ J/cm}^2$ . This leads to the conclusion that the XeCl excimer laser with long laser pulses  $\geq 200 \text{ ns}$  is not optimal for the fabrication of three dimension optical components.

### ***3.11 Dependence of the etch rates and etch roughness on the etch area***

The dependence of the etching rates of quartz on the size of the structured areas in quartz by LIBWE were investigated by Wang et al. [85]. A KrF excimer laser (248 nm) and 0.4 M pyrene in acetone solution were used in these experiments. The investigations suggest that the etch rates are decreasing with a decrease of the irradiation areas. The etch rates obtained for features with a diameter of 100  $\mu\text{m}$  in quartz is 5 nm per pulse, while 10 times larger structures can be etched with rates of 9 nm per pulse. Two explanations of this phenomenon were suggested by the authors. A different temperature gradient in the depth and along the etched craters of the quartz sample is created. This results in faster distribution of the temperature around the perimeter of the etched area than in the depth for small structures. The second reason may be related to the cooling process by the surrounding liquids. Smaller irradiation areas generate smaller volumetric temperature jumps which results in the generation of the smaller laser induced bubbles. The pressure jump generated by the shock wave and growth/collapse of the laser induced bubbles can be also weaker for the smaller etch areas. This effect is also important in our work, especially for the fabrication of the small dimension micro-optical components, such as random phase plates with sizes of the features below 250  $\mu\text{m}$ . The dependency of the etching parameters (etch rate, etch roughness, number of incubation pulses) on the irradiated areas of quartz by LIBWE using a XeCl excimer are shown in Fig. 3-51 A, B and C.

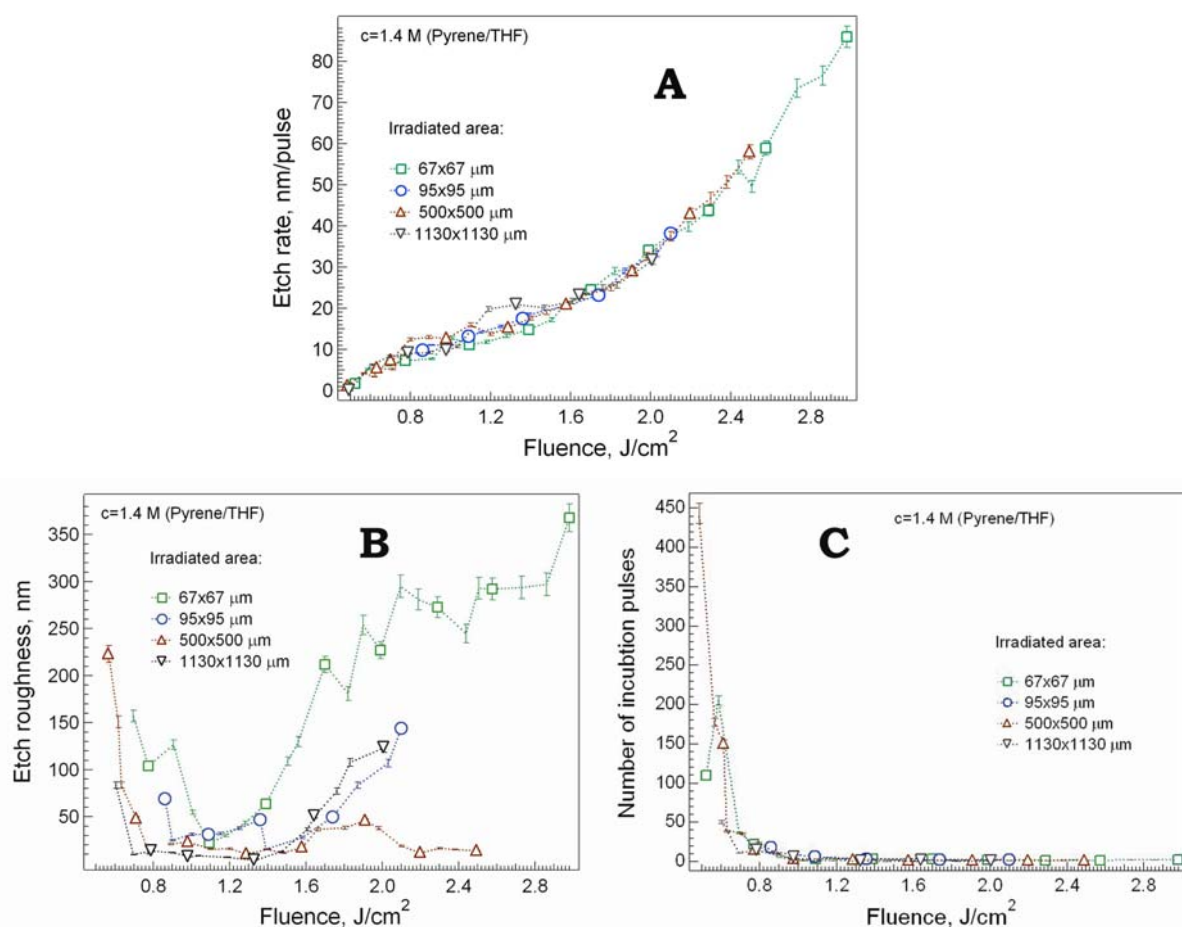


**Fig. 3-51** Dependency of the etch rate (A), etch roughness (B) and number of incubation pulses (C) of quartz by LIBWE using XeCl excimer laser on the etch area.

The etch rates of quartz by LIBWE for 308 nm are similar for all irradiated areas. This suggests that the etch rates are not dependent on the thermal properties of the material. The most plausible reason of the etch rate dependency on the size of the irradiated area, measured by Wang et al. [85] but not observed in our case, may be related to the different etching mechanisms of LIBWE with 308nm laser compared to the 248 nm laser. The similar number of the incubation pulses (shown in Figure 3-51 C), obtained for the all irradiated areas suggest that there is no change of the etching mechanism when the irradiated areas are decreasing. However, the etch roughness (shown in Figure 3-51 B) suggests a clear dependence on the size of the etched features. The lowest etch roughness  $>50$  nm is obtained for  $60 \times 60 \mu m$  square areas only within a very narrow laser fluence range ( $1.1-1.3 J/cm^2$ ), while  $1 \times 1$  mm square areas can be precisely structured with fluences from  $0.7-1.6 J/cm^2$ . An increase of the etch roughness with a decreasing size of the

irradiation areas can be due to differences in the removal of the molten material and requires further investigations. The studies suggest that there are some limitations of the LIBWE process in terms of fabrication of very small features with very low etch roughness in quartz using XeCl excimer laser as irradiation source.

### ***3.12 Etching of different UV transparent materials by LIBWE***

The Laser Induced Backside Wet Etching is a unique method which can be utilized for the precise structuring not only of quartz samples but also for other UV transparent materials, such as BaF<sub>2</sub>, CaF<sub>2</sub> and sapphire. The etching of fluorides (CaF<sub>2</sub> or BaF<sub>2</sub>) is very difficult to achieve with any method due to the properties of these materials. The etch rates of CaF<sub>2</sub> by RIE is very low, only several tens of nm/hour and is rather tedious and expensive. The etching process of sapphire is even more complex, because of the very high melting point and excellent mechanical characteristics of sapphire. LIBWE may be an alternative method for structuring of these UV transparent materials. The experimental results of the etch rates, etch roughness and number of incubation pulses of quartz, BaF<sub>2</sub> and sapphire by LIBWE using 1.4 M pyrene in THF solution as etching media and a XeCl excimer laser as irradiation source are summarized in Figure 3-52.



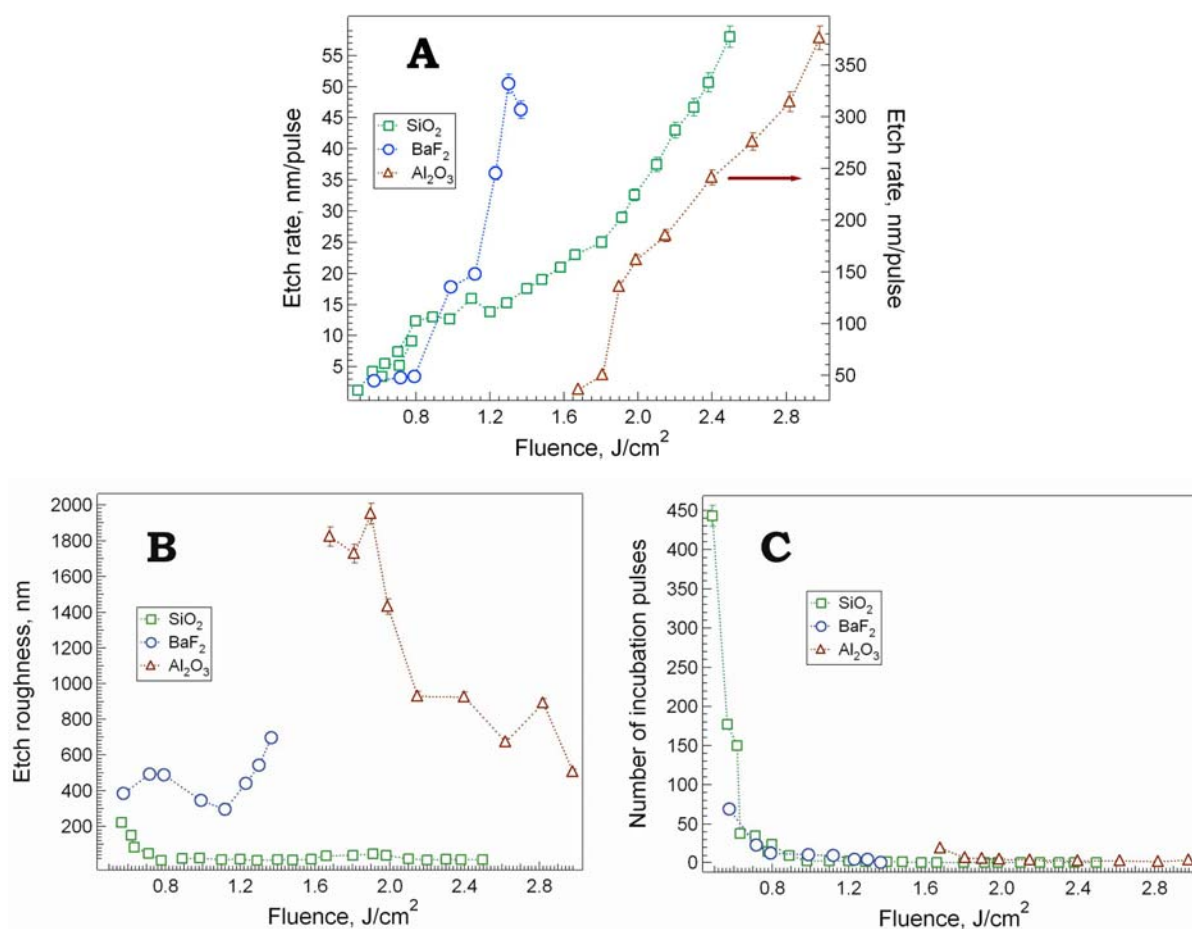


**Fig. 3-52 Etch rate (A), etch roughness (B) and number of incubation pulses (C) of silica, BaF<sub>2</sub> and sapphire by LIBWE using XeCl excimer laser and 1.4 M pyrene in THF solution**

The threshold fluences for BaF<sub>2</sub> and sapphire are difficult to determine precisely due to the low etch rates and high etch roughness. Therefore the threshold fluences for BaF<sub>2</sub> and sapphire are defined as the lowest laser fluence, for which etching can be quantified. Modification of the BaF<sub>2</sub> and sapphire surface can be achieved at fluences below this defined threshold value, but it is impossible, however, to determine the etch rates. The experimentally obtained threshold fluences for silica, BaF<sub>2</sub> and sapphire by LIBWE using 308 nm excitation and 1.4 M pyrene in THF solution are summarized in Table 4 together with the thermodynamic and mechanical properties of these materials [86].

Table4. Threshold fluence by LIBWE, mechanical and physical properties of UV transparent materials

	SiO <sub>2</sub>	BaF <sub>2</sub>	Al <sub>2</sub> O <sub>3</sub>
Threshold fluence, J/cm <sup>2</sup>	0.5	0.57	1.6
Melting temperature, °C	1600	1280	2040
Rupture modulus, MPa	50	26	350-690
Thermal diffusivity, m <sup>2</sup> /s	$8.4 \cdot 10^{-7}$	$5.8 \cdot 10^{-6}$	$6.56 \cdot 10^{-6}$

The melting temperature and modulus of rupture is in the case of BaF<sub>2</sub> much lower compared to quartz. This would suggest, if we consider simple thermal model, that the threshold fluence for BaF<sub>2</sub> should be lower compared to quartz. However, the experimental results show a different behavior. The reason for this observation may be due to the difficulties to determine the threshold fluence for BaF<sub>2</sub>. The high threshold fluence for sapphire could be due to the high melting point and strong mechanical properties of this material. The lowest etch rates for BaF<sub>2</sub> and for Al<sub>2</sub>O<sub>3</sub> are obtained, as expected, at the lowest laser fluence ranges ( $\leq 0.8$  J/cm<sup>2</sup> for BaF<sub>2</sub> and  $\leq 1.8$  J/cm<sup>2</sup> for sapphire). With an increase of the laser fluences above 0.8 J/cm<sup>2</sup> for BaF<sub>2</sub> and 1.8 J/cm<sup>2</sup> for sapphire the etch rates increases drastically. The increase of the etch rates is most probably associated with the generation of a plasma in solution (similar to the case for quartz at the laser fluences  $> 2$  J/cm<sup>2</sup>). Etching of BaF<sub>2</sub> at fluences higher than 1.3 J/cm<sup>2</sup> is not possible due to breaking of the material. This may be associated with the pressure jump which may exceed the rupture modulus of the material. The highest etch rates of all tested materials are obtained for sapphire. The reason of this observation could be associated with the 8 times higher thermal diffusivity obtained for this material as compared to silica. This suggests that the same temperature rise in the case of sapphire melts a much thicker layer compared to quartz. However this reason can not be used for explaining the relatively low etch rates of BaF<sub>2</sub>, because the thermal diffusivity of this material is also much higher than for quartz. Another explanation for the high etch rates obtained for sapphire can be associated with the plasma process.

The roughness of the etched features in quartz and sapphire strongly depend on the laser fluences (shown in Fig.3-40 B). The slope of the etch roughness obtained for quartz and Al<sub>2</sub>O<sub>3</sub> is similar: the highest etch roughness is obtained at the fluences just above the

threshold. But the roughness of the etched features in BaF<sub>2</sub> reveals a complete different behavior. The lowest roughness of the etched features ( $\approx 360$  nm) is in the case of BaF<sub>2</sub> at least 20 times higher than the lowest etch roughness obtained for silica ( $\approx 15$  nm). This is, most probably, associated with the lower mechanical stability and lower resistance to the temperature and pressure jumps of BaF<sub>2</sub> as compared to quartz. The mechanical stability of the material is expressed by the modulus of rupture, which is defined as the load which is required to break a bar of one inch square. The values of the modulus of rupture for the different UV transparent materials are shown in Table 4. An increase of the laser induced pressure above the modulus of rupture results in the generation of cracks and damaging of the material. The values of this critical load pressure obtained for quartz are much higher than the values for BaF<sub>2</sub>. The lower mechanical stability of BaF<sub>2</sub> may be the reason for the high etch roughness. The pressure generated at the sapphire-liquid interface may be slightly too weak to remove all molten material from the surface. Therefore the etch roughness due to fast resolidification in the case of sapphire are very high and are in the range of 0.6-1.8  $\mu\text{m}$ . Nevertheless, the etch rates of the sapphire by LIBWE show the highest values among all studied UV transparent materials. The number of the incubation pulses has a similar behavior for all tested materials, which suggest that the etching mechanism just above the threshold is similar for BaF<sub>2</sub>, quartz and sapphire i.e. dominated by the formation of a carbon layer. Although the etching of BaF<sub>2</sub> and sapphire provides relatively high etch roughness, the LIBWE process still can be useful technique for the fabrication of binary and more complex patterns in these materials.

In summary, these data reveal that the etching by LIBWE is not only influenced by the laser (wavelength and pulse length), the etching media and the thermal properties of material, but also other material properties, i.e. mechanical, are important. These features are extremely difficult to include in our temperature model, which is described in subchapter 3.1

## 4 Fabrication of micro-optics in quartz

Arrays of micro-optical components fabricated in UV transparent materials are utilized in many different applications, e.g. optical telecommunication, high quality imaging systems, beam wave front measurements, multiple beam shaping and homogenizing [1, 6, 8, 87, 88]. The last approach involves shaping and homogenizing of high power excimer and Nd:YAG laser beams. These lasers are key elements in laser micromachining and high quality imaging applications. However, the high quality images and ablation craters are achieved only with homogeneously distributed laser beams. For this reason a lot of attention was focused in this work on the fabrication of micro-optical components which can be used as beam homogenizers for the above mentioned lasers. The concept of beam homogenizing relies on a splitting of the laser beam into many beamlets [88, 89]. This is achieved either by a Random Phase Plate (RPP) or by using a micro-lens array (MLA). The detail description of beam homogenizing with RPP and MLA will be given in subchapter 4.1. A random phase plate consists of a number of randomly distributed binary structures which are fabricated in quartz. The evaluation of a RPP and the fabrication steps or LIBWE will be described in detail in subchapter 4.2. Micro-lens arrays (MLA's) consist of three dimensional structures with continuous profiles. For this reason the fabrication of MLA is more complex and requires additional optical element, i.e. a *Diffractive Gray Tone Phase Mask* (DGTPM). The concept for the fabrication of micro-lenses will be described in subchapter 4.3. The DGTPM is a key element which is utilized in the creation of the three dimensional structures in UV transparent materials. A detail description of the fabrication of DGTPM will be given in subchapter 4.4. The fabrication of the micro-lenses in quartz and in other UV transparent materials will be discussed in subchapter 4.5. The characterization of the MLA's fabricated in quartz will be described in subchapter 4.6. The beam shaping results of the nanosecond Nd:YAG and femtosecond Ti:Sapphire lasers by using the RPP will be discussed in subchapter 4.7. The improvement of the beam profile of nanosecond Nd:YAG and XeCl excimer lasers by using the quartz MLA's will be shown in subchapter 4.8.

#### 4.1 Concept of beam shaping with MLA and RPP

If we believe our ancient history, then the earliest reported beam shaping technique was developed by Archimedes, who developed a mirror system to collect the sun light to focus it on Roman ships. If this legend is correct, then this was the first use of a multi-faceted beam shaping technique, where a beam was broken into many beamlets which were directed onto a target. Modern beam shapers, which consist of micro-lens arrays, however, had to wait for the development of micro-fabrication technology and lasers. The key element in beam homogenizing is based on splitting of an incoming laser beam into many beamlets, as illustrated in Figure 4-1 [90, 91]. This is achieved for example, by using a micro-lens array.

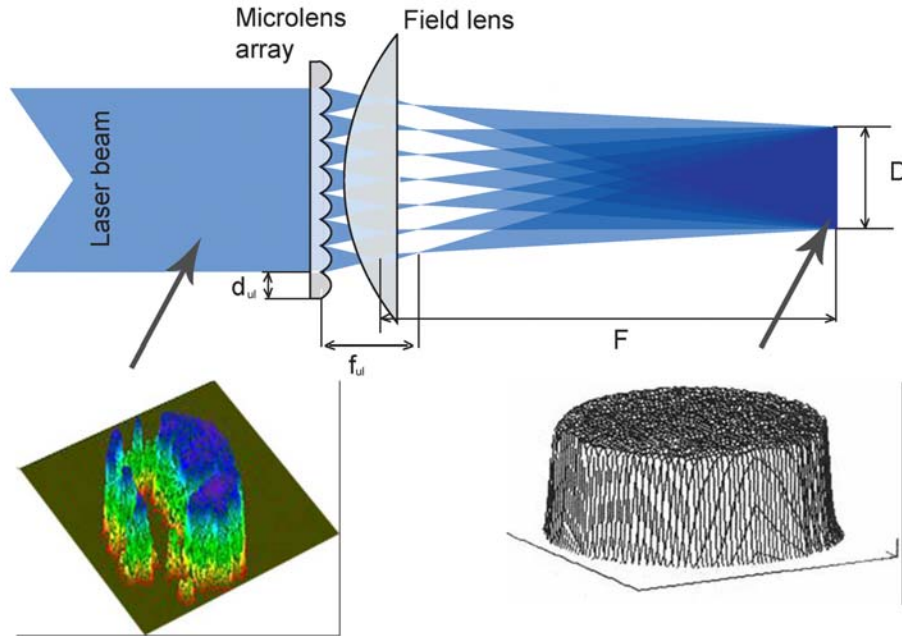


**Fig. 4-1. Diffractive beam integrator setup**

A field lens, located before the focal length of the micro-lens array (marked as  $f_{ML}$  in Figure 4-1) collects all beamlets and directs them towards the target. Each beamlet expands homogeneously just after the focal plane of the MLA. The intensity of each beamlets is distributed over the complete area at the focal plane of the collecting (field) lens resulting in an equivalent energy distribution over the area  $D$ . An incoming laser beam with the uneven intensity distribution is therefore converted into a beam with a homogenous energy

distribution, as shown in Figure 4-1. The beam homogenizer which is shown in Figure 4-1 is mainly applied for the coherent laser beams, produced e.g. by Nd:YAG. This is due to the fact, that the beam at the target plane must be the sum of defocused diffraction limited spots, which can be produced only with coherent lasers. This type of the beam homogenizer is, therefore, also known as diffracting beam integrator. The beam size (marked as  $D$  in Figure 4-1) at the homogenizing plane depends on the focal length and diameter of the micro-lenses, and on the focal length of the collecting lens which is described by equation (29):

$$D = \frac{F \cdot d_{ul}}{f_{ul}} \quad (29),$$

where  $D$  is the beam size at the focal plane of the collecting lens,  $d_{ul}$  and  $f_{ul}$  are focal length and diameter of the micro-lens.

For the beam homogenizer which consists of a MLA with a diameter and focal length of each micro-lens of 500  $\mu\text{m}$  and 60 mm, respectively, and a focal length of the collecting lens of 250 mm it is possible to achieve a 2 mm homogenously distributed Nd:YAG beam. The problems of Nd:YAG beam shaping with a diffractive beam integrator are related to strong coherence effects, which will be discussed in detail later.

Another type of beam shaper, which can be used for the non coherent lasers, such as excimers, is shown in Figure 4-2. This type of beam homogenizer is called an imaging beam integrator.

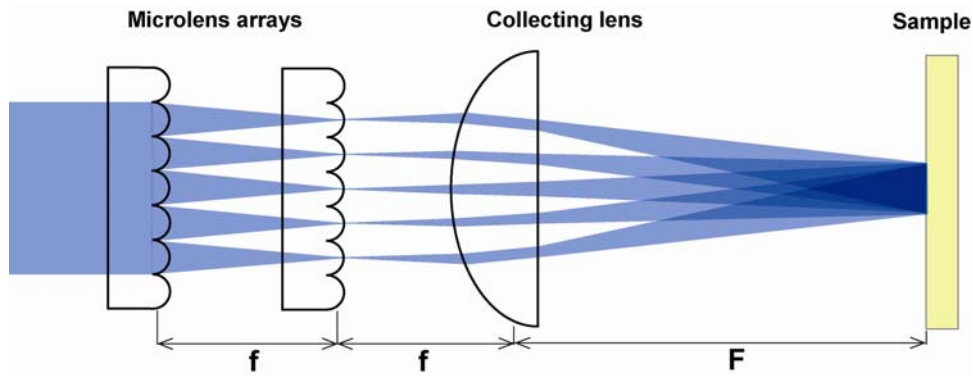


**Fig. 4-2 Imaging beam integrator setup**

It consists of two micro-lens arrays and one collecting lens, and is more expensive as the previously described system. The MLA segments the beam and focuses the beamlets onto the second micro-lens array which images the patterns on the target plane. The collecting

lens overlaps all the imaged sub-apertures at the target plane, which corresponds also to the focal plane of the collecting lens. The drawbacks of the beam integrators with the MLA's are the high production cost and the difficult fabrication. Therefore an alternative beam shaping technique was suggested by Y Kato et al [92]. This technique utilizes specially designed phase plates, which consist of a two dimensional array of transmitting areas. Each of the patterns applies a phase shift of either 0 or  $\pi$ .

This phase plate is called a random phase plate (RPP) and is placed close to the collecting lens, as shown in Figure 4-3.

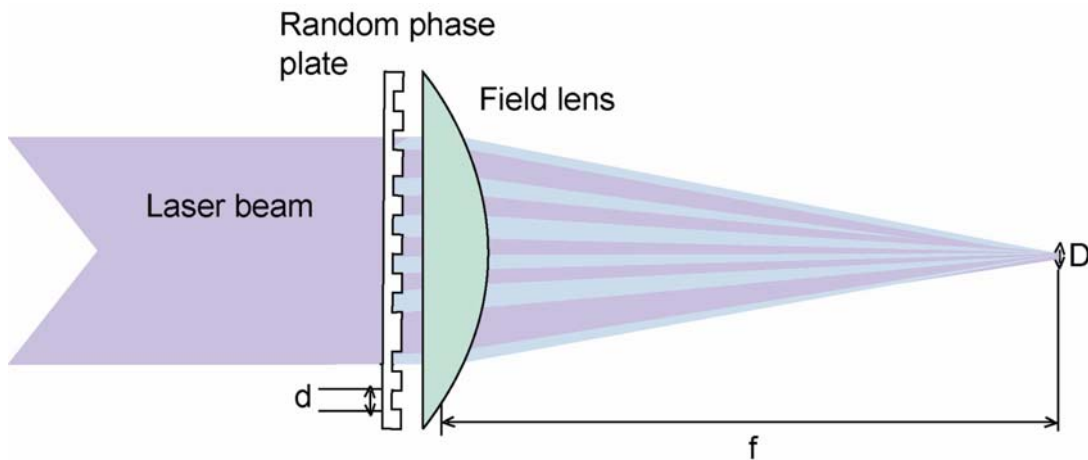


**Fig. 4-3 Beam homogenizing with random phase plate setup**

The equal numbers of 0 and  $\pi$  phase shifted beamlets destructively interfere at the focal plane of the collecting lens, resulting in a smooth profile [93, 94]. Such beam shaper has an advantage compared to the MLA which is easy to fabricate, but the disadvantage that the RPP can be applied only for a single laser wavelength.

In order to test and compare the above described beam homogenizing techniques, RPP and MLA are fabricated in quartz by LIBWE.

## ***4.2 Fabrication of the Random Phase Plates***

The fabrication of a Random Phase Plate starts with its design. The phase plate must have an equal number of structured and non structured areas which result in the same number of patterns which produces equal number of 0 and  $\pi$  phase shifted beamlets. The first step is an evaluation of the number of speckles in x and y direction, which is achieved with a home made PC program developed in IGOR. The program randomly generates positions of

the speckles in x and y direction. The design of a RPP is successful, when the ratio, between the numbers of the features which produce  $\pi$  phase shifts to the number of the non structured areas is in the range of 0.49-0.51. The program saves the evaluated speckle position in the micrometers and transforms them into the number of steps required to move the motorized xyz stage. The program also evaluates how deep the speckles must be etched in order to produce a  $\pi$  phase shift. This is evaluated by equation 30:

$$d = \frac{\lambda}{2 \cdot (n - 1)} \quad (30),$$

where  $\lambda$  is wavelength for which the RPP is designed,  $n$  is the refractive index of quartz at the operating wavelength.

An example of a RPP, designed for 9x9 mm irradiation area is shown in Figure 4-4.



**Fig. 4-4 Computer aided design (CAD) of RPP for 9x9 mm irradiated area. Speckle size 250  $\mu\text{m}$**

The RPP (shown in Figure 4-4) is designed for the 4<sup>th</sup> harmonic of a Nd:YAG laser ( $\lambda=266$  nm) and consists of 659 green patterns, which will be etched to a depth of 250 nm. The size of each speckle is 250x250  $\mu\text{m}$ .

After the CAD of the RPP, the areas marked green in Figure 4-4 must be etched into the quartz to a depth described by equation 30. The etch depth is controlled by the number of cumulative laser pulses. The fabrication of a RPP is achieved by LIBWE using an experimental setup, which is shown in Figure 4-5.



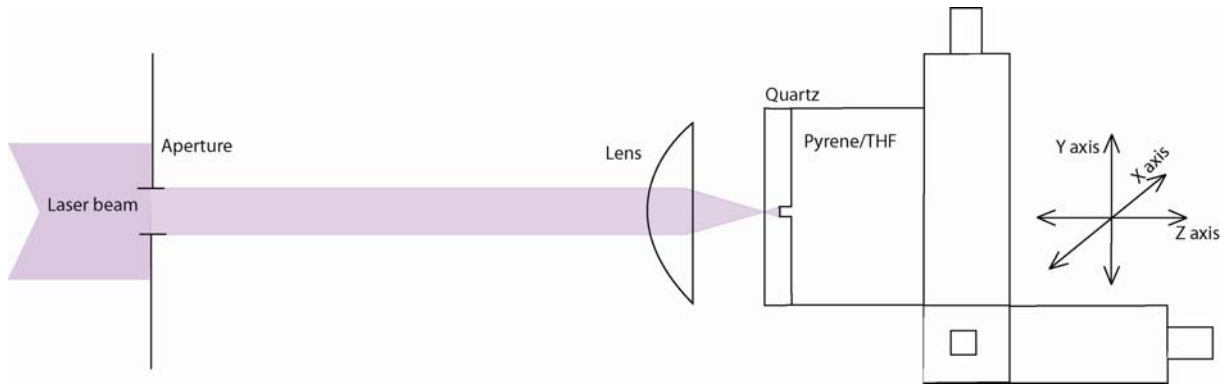


**Fig.4-5 Experimental setup for fabrication of RPP in quartz by LIBWE**

A XeCl excimer laser beam passes through the 2.5x2.5 mm square aperture and is imaged onto the backside of quartz using an achromatic lens with a focal length of 100 mm. The size of the imaged spot depends on the distances between the aperture and imaging lens, as well as on the distance between the lens and quartz plate which is in contact with solution. These distances are evaluated using equation 31:

$$a = f \cdot (M + 1)$$

$$b = \frac{f \cdot (M + 1)}{M} \quad (31),$$

where  $a$  is the distance between the aperture and lens,  $b$  is the distance between the lens and quartz,  $f$  is the focal length of the lens and  $M$  is the demagnification.

The distance between the aperture and lens must be 1100 mm, while the distance between lens and quartz is 110 mm in order to produce 250  $\mu\text{m}$  square patterns by using 2.5 mm square aperture and a  $f=100$  mm focal length lens. A part of a RPP etched in quartz by LIBWE using a 1 M pyrene in THF solution as etchant, 1.4  $\text{J}/\text{cm}^2$  laser fluence and 23 laser pulses each speckle, is shown in Figure 4-6.

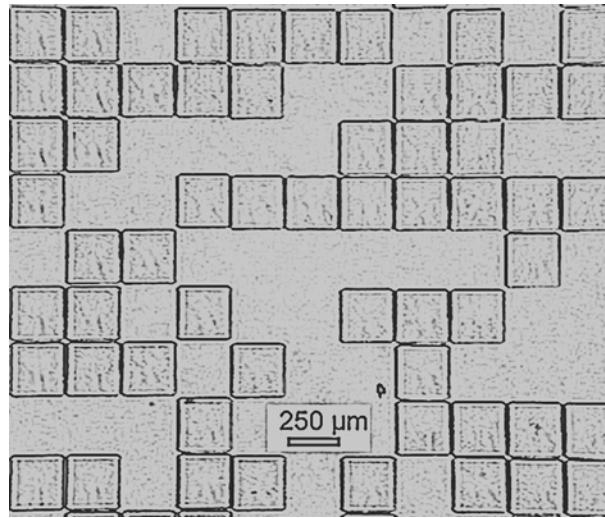


**Fig. 4-6** Fragment of RPP etched in quartz by LIBWE with 1 M pyrene/THF solution, 1.4 J/cm<sup>2</sup> laser fluence and 23 laser pulses.

This RPP was tested as beam homogenizer for a high power quadrupled Nd:YAG laser. The results of these tests will be shown later.

### ***4.3 Fabrication of quartz micro-lens arrays***

An alternative method for the fabrication of 3 dimensional microstructures in UV transparent materials is the combination of LIBWE and projection of a Diffractive Gray Tone Phase

Mask. A DGTPM encodes the shape of two or three dimensional structure, e.g. Siemens star, Fresnel lens, plano convex lens and etc. into the laser intensity beam profile.

The DGTPM was invented by Smith et al [95, 96]. The authors claimed that there is an easy way for the modulation of laser beams by the application of simple periodical structures with different line widths which are fabricated in quartz. These masks do not absorb the laser radiation and can therefore not be damaged. For this reason they have much higher damage thresholds compared to the absorbing/reflecting metal masks. Further developments of the DGTPM were performed by David et al. [47], who also applied a DGTPM for the fabrication of the three dimensional structures, i.e. arrays of Fresnel micro-lenses in photopolymers. A DGTPM is the key element in the fabrication of quartz micro-lenses. It is therefore important to understand the working principle of DGTPM and the fabrication process. A DGTPM is a binary structure which consists of periodical line

patterns etched into quartz. The mask consists of many line structures with different widths, which modulate the incoming laser beam intensity into a spherical shape or even more complex shapes as shown in Figure 4-7.

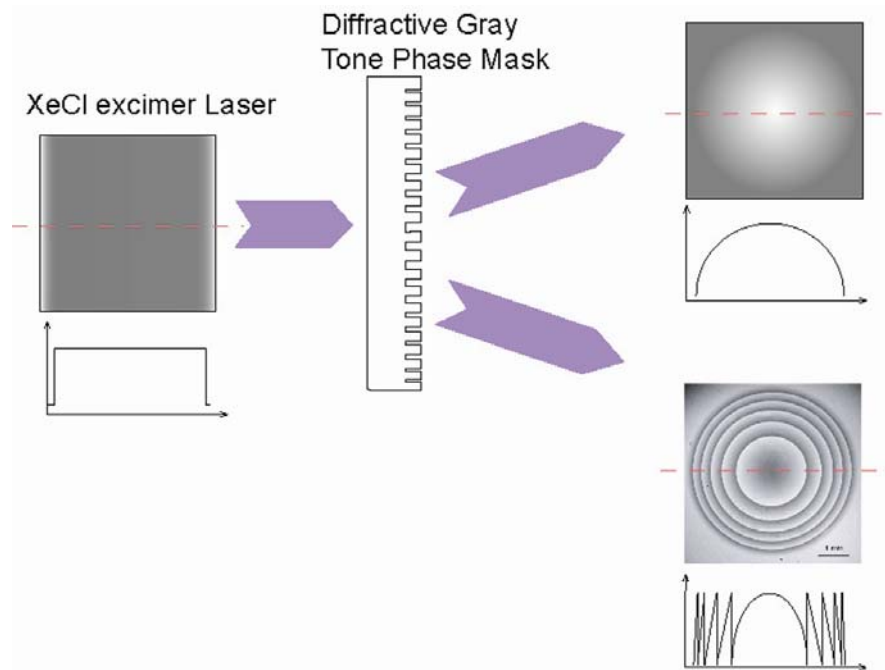


**Fig. 4-7 Modulation of the laser beam by DGTPM**

The DGTPM does not absorb the incoming laser beam intensity but diffracts it in to many angles, known as diffractive orders. Diffraction is the phenomenon, when the light goes not in the straight direction (shown as dashed lines in Figure 4-8), when it passes through an aperture or periodical structure, as shown in Figure 4-8.

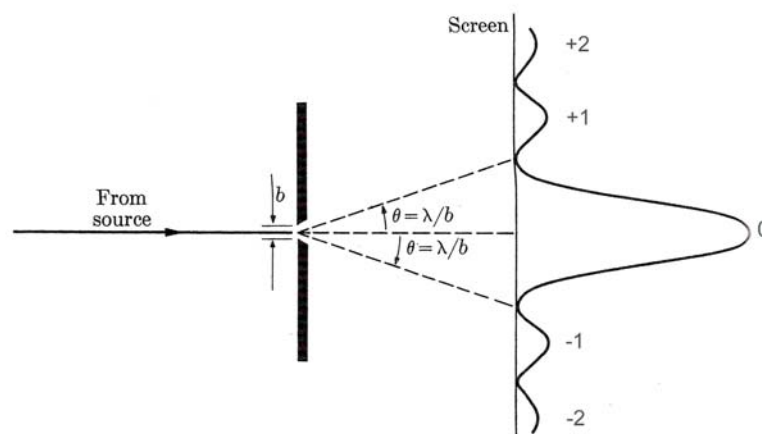


**Fig. 4-8 Diffraction of light through an aperture**

What happens when a beam passes through an aperture? The beam loses intensity and produces a sharp intensity peak at the center. The width of this beam depends on the size of the aperture. This is correct for very large apertures, which are much larger than the irradiation wavelength. The intensity profile of the beam which passes through an aperture with a diameter below 1 millimeter reveals a broad peak in the center and several small peaks on the sides, as is illustrated in Figure 4-8. Huygens and Fresnel suggested following explanation for this phenomenon: the light which passes through the aperture can be described as a sum of spherical light waves, generated at each point over the aperture diameter. The intensity distribution of the diffracted wave is obtained by adding the intensities of these spherical waves. The maxima and minima of the diffracted beam intensity are due to the interference effect between these spherical waves. Fraunhofer came to the conclusion [97] that the angle between the diffracted beams (marked as  $\theta$  in Figure 4-8) is proportional to the aperture width and the irradiation wavelength and can be described by equation 32. This equation is very similar to the equation of constructive interference, suggested by Bragg [5].

$$\Theta = \arcsin(m \cdot \lambda / b) \quad (32),$$

where  $\lambda$  is the wavelength of the light,  $b$  is the width of an aperture and  $m$  is an integer (shown in Figure 4-7 as 0,  $\pm 1$ ,  $\pm 2$ ) which is also known as the diffraction order.

The diffraction of the laser beam is enhanced if arrays of the periodically spaced apertures (known as diffractive gratings) are used. The intensity of the main peak (also known as 0 order diffraction intensity) and side peak intensity (named as higher orders) strongly depends on the ratio between the aperture diameter (known as the line width) and space between the apertures (known as the grating period). The 0<sup>th</sup> order intensity can be smoothly varied between the 0% and 100 % just by varying the ratio between the line width and the grating period. Different types of gratings exist, and most commonly used are either amplitude gratings, which alter the amplitude of the incoming monochromatic irradiation, or phase gratings, which modulate the incoming beam phase. Gratings can be either transmission, which transmit diffractive radiation, or reflective, where the diffractive beam is reflected. Transmission gratings consist of either three dimensional structures, such as triangular shape features (amplitude gratings) or of binary structures (phase gratings) etched into quartz. The amplitude gratings are difficult to fabricate because of the

complex 3D structures. For this reason only transmission phase gratings were used in this work. These gratings consist of periodic line structures etched in quartz. The 0<sup>th</sup> order transmission ( $T$ ) of the phase grating depends, according to scalar diffraction theory, on the ratio between the line width and the grating period, which is called duty cycle ( $DC$ ) and is described by equation 33:

$$T = 1 - 2 \cdot DC \cdot (1 - DC) \cdot (1 - \cos\varphi) \quad (33),$$

where  $\varphi$  is the phase shift of the diffracted beam, which is proportional to the depth of the binary structures, that is described by equation 34:

$$\varphi = \frac{h \cdot 2 \cdot [n(\lambda) - 1] \cdot \pi}{\lambda} \quad (34),$$

where  $\lambda$  is the irradiation wavelength,  $n(\lambda)$  is the refractive index of quartz at the laser wavelength  $\lambda$ , and  $h$  is the depth of the structure.

According to equation 33, the transmission of the grating is equal 0 at a  $DC=0.5$ , when the phase shift is  $\pi$ . The 0<sup>th</sup> order transmission of the phase grating at various  $DC$  for 308 nm irradiation wavelength and a phase shift of  $\pi$  (or structure depth of 310 nm) is shown in Figure 4-9.

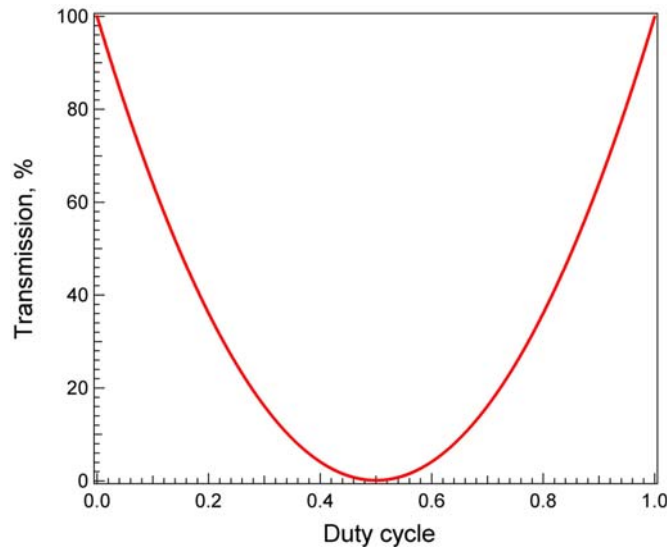


**Fig. 4-9 DGTPM efficiency at various DC for 308 nm irradiation**

The modulation depth of the mask can be easily adjusted by changing the depth of the structure. This is an important observation for the fabrication of micro-optical elements in quartz by LIBWE and will be explained in detail later. For the fabrication of micro-optical elements in quartz by LIBWE, a DGTPM which consists of many periodical lines with

various line widths and with a constant period between the lines is required. These masks are fabricated in quartz by electron beam lithography and Reactive Ion Etching. In principle for the encoding of micro-optics by DGTPM both DC ranges- between 0 and 0.5 and/or between 0.5 and 1-can be used. The second DC region (0.5-1) requires much thicker line widths of the structures and is therefore slow to fabricate and expensive. On the other hand the structures with the line width smaller than 150 nm are difficult to fabricate. The widths of the structures width in the DGTPM was therefore limited between 150 nm and 2.5  $\mu\text{m}$ .

#### ***4.4 Fabrication of DGTPM***

The DGTPM in quartz is fabricated by a combination of e-beam lithography and reactive ion etching techniques. The first step for the fabrication of a DGTPM is the evolution of the line widths and their spatial positions, which encodes the desired structure. An example of a calculated DGTPM, which encodes a plano convex lens shape structure is shown in Figure 4-10.

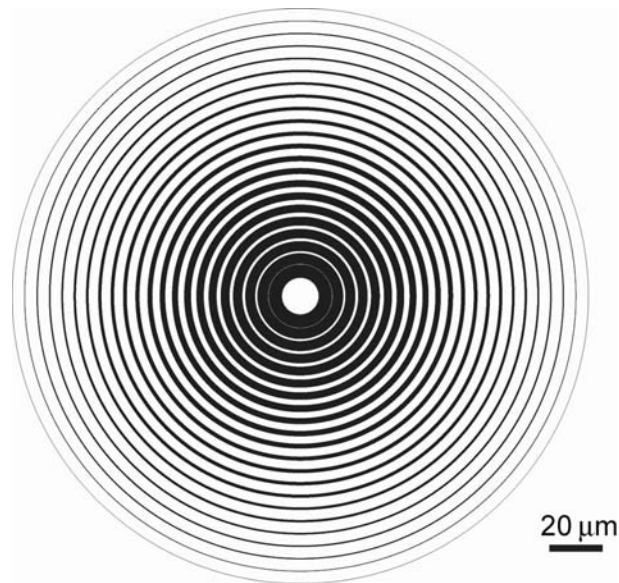


**Fig.4-10 Evaluated DGTPM which encodes plano-convex lens shape**

The diameter of the DGTPM is 5 mm. This mask consists of 1000 lines with various widths (from 150 nm to 2.5  $\mu\text{m}$ ), which are spaced with a period of 5  $\mu\text{m}$ . The second step consists of etching of the different line width structures into quartz. This is achieved by several production steps, which are summarized in Figure 4-11.

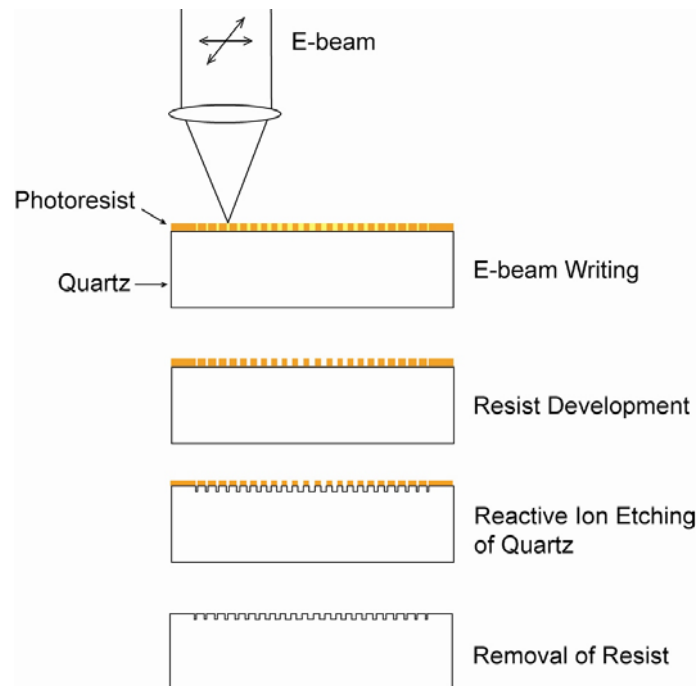


**Fig. 4-11 Fabrication steps of DGTPM in quartz.**

The first step is sputtering of 80 nm chromium layer on the surface of the quartz or using the commercial mask blanks. This chromium film acts as a stop layer for the e-beam. On top of the chromium film a 120 nm thick resist layer, i.e. polymethyl methacrylate (PMMA) is spin coated. The round shape lines with various line widths are structured into the resist by using LION-LVI electron beam lithography system from Leica Lithographiesysteme Jena. This machine has some special features such as continuous path control for the exposure of straight or curved lines, which allows continuous writing of any shape of line structures. For this reason this e-beam system is much more advanced compared to the standard vector scan e-beam lithography machines, in which exposed lines are controlled by choosing a number of the equidistant pixels. Second advantage of the LION-LVI electron beam system is the description of the curved lines by a Bezier polynomial function. This simplifies the data format and reduces the total exposure time. For every curved line with a different line width it is necessary to adjust the e-beam dose, in order to achieve the critical dose required to modify the resist. This is possible by simply adjusting the speed of the translation stage on which the sample is attached. A new approach for the structuring of lines with the continuous widths was suggested by David et

al. [97], where the line width of the structures are varied by simply adjusting the defocus of the electron beam, as shown in Figure 4-12.

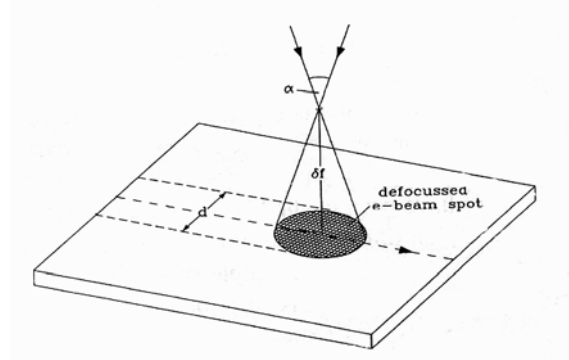


**Fig. 4-12 Idea of the e-beam writing of line structures with continuous line widths**

The width of the structures  $w$  depends on the aperture angle  $\alpha$  ( $\alpha=0.0133$ ), on the defocus  $\delta f$  and on the line dose  $D_l$  and can be described by equation 35:

$$w = \alpha \cdot \delta f \cdot \sqrt{1 - \left( \frac{\pi}{2} \cdot \frac{D_0}{D_l} \cdot \alpha \cdot \delta f \right)^2} \quad (35),$$

where  $D_0=15 \mu\text{C}/\text{cm}^2$  is the critical exposure dose of the resist per unit area.

The defocus  $\delta f$ , according to David et al. [97], can be described by equation 36:

$$\delta f = \frac{w}{(k \cdot \alpha)} \quad (36),$$

where  $k$  is a parameter ( $k=0.9-0.95$ ) which is obtained experimentally.

The line dose is described by equation 37 which is derived from 35 and 36:

$$D_l = \frac{\pi \cdot D_0 \cdot w}{2 \cdot k \cdot \sqrt{1 - k^2}} \quad (37).$$

The line doses evaluated by equation 37 agree well with the experimental results for the line widths structured in PMMA by e-beam, which are above 400 nm [97]. For lines thinner than 400 nm the defocus is assumed to be zero. The experimental results of the line widths at various exposure doses are fitted by an asymptotical function [97]. The doses which are required for the structuring of line widths below 400 nm are obtained from this function. The data of the doses and the defocus values for DGTPM lines are converted to a special data file, which is send to the board computer of the LION-VI e-beam machine. Typical exposure time for a DGTPM with a diameter of 5 mm is 12-20 hours, depending on the complexity of the structures.



The second step is the development of the exposed areas in the resist. This is achieved with 4-methylpentan-2-one (MIBK) and isopropanol (IPA) solution with a ratio of 1:3. The etching is completed within 120 seconds. The development of the resist results in removing the PMMA from the areas which are exposed with e-beam, while the unexposed resist stays unchanged. After this step the grating structure is examined with an optical microscope. The next step is etching of the chromium film, which is achieved by RIE using a  $\text{Cl}_2/\text{CO}_2$  plasma. This plasma effectively reacts with chromium, but almost does not etch the resist and quartz plate. This removal process takes about 120 seconds. After this procedure the DGTPM is inspected again. The next step is removal of the PMMA resist. This is achieved by RIE using oxygen. The  $\text{O}_2$  ions remove PMMA without etching the underlying chromium film. The next procedure is transferring the DGTPM lines from the chromium film into the quartz. This is achieved with a Oxford RIE machine using a fluoroform ( $\text{CHF}_3$ ) and oxygen ( $\text{O}_2$ ) gas mixture with a ratio 1:1. The etch rates of quartz with RIE is approximately 20 nm/min. The depth of the structures in quartz is frequently examined with a profilometer during the whole etching process. After etching the quartz plate is cleaned with a mixture of  $\text{HNO}_3$  and  $\text{HCl}$  with a ratio of 1:3. This cleaning procedure removes the thin chromium film.

The DGTPM's fabricated in quartz which encode 3 dimensional Fresnel lens shape and a binary Siemens star structures are shown in Figure 4-13.

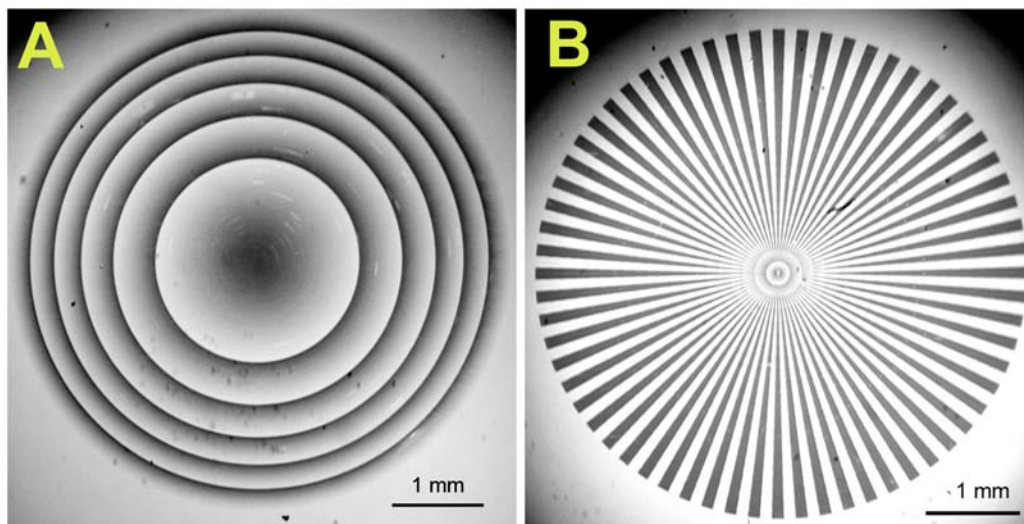


**Fig.4-13 DGTPM fabricated in quartz, which encode: Fresnel lens shape structure (A), Siemens Star structure (B).**

The diameter of each mask is 5 mm. Each mask consists of 1400 lines with different widths, spaced by  $3.5\ \mu\text{m}$ . The DGTPM which encodes a Fresnel lens shape is used for the production of Fresnel micro-lenses in quartz and in other UV transparent materials. The Siemens star structures is used to test and optimize the micro-lens fabrication process.

#### 4.5 Fabrication of micro-lens arrays by LIBWE and DGTPM

An experimental setup for the fabrication by LIBWE of the complex micro-structures in UV transparent materials consists of imaging of the beam modulated by the DGTPM and is shown in Figure 4-14.

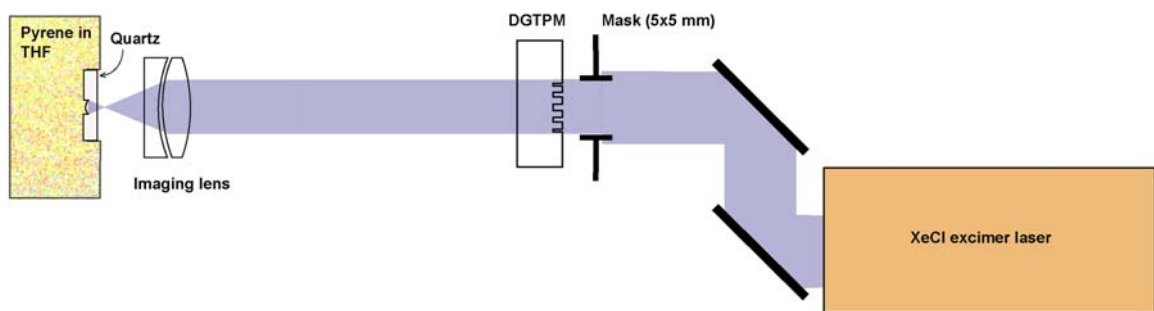


**Fig. 4-14 Experimental setup for fabrication of complex 3 dimensional structures in UV transparent materials**

The first step in the fabrication of high quality optical components in quartz is a careful optimization of the imaging setup. The distances between the DGTPM and imaging lens and from the lens to the sample must be set very carefully. These distances are evaluated by equation 31. The demagnification  $M$  is either 5 or 10 and depends on the desired diameter of the micro-lenses. The evaluated distances could not be simple adjusted manually with the hope to get high quality micro-lens, due to the fact, that the depth of the image plane is only 0.5 mm! Therefore a Siemens star mask was applied to find the exact distance between the lens and the sample, which corresponds to the imaging plane. The chamber with the quartz window is filled with a pyrene in acetone (or THF) solution and is fasten on the motorized x-y-z stage with a spatial resolution of  $0.1\ \mu\text{m}$ . An array of Siemens star micro-structures with diameters of  $500\ \mu\text{m}$  is etched in quartz using different positions between the imaging lens and the sample. After this step the Siemens star array in quartz is carefully inspected with the optical microscope and the distance between the

imaging lens and sample is determined, where the lines of the Siemens star structure are sharp and well defined. An example of the Siemens star structure etched in quartz by LIBWE using 0.4 M pyrene in acetone solution and a KrF excimer laser (248 nm, 20 ns) as irradiation source is shown in Figure 4-15.

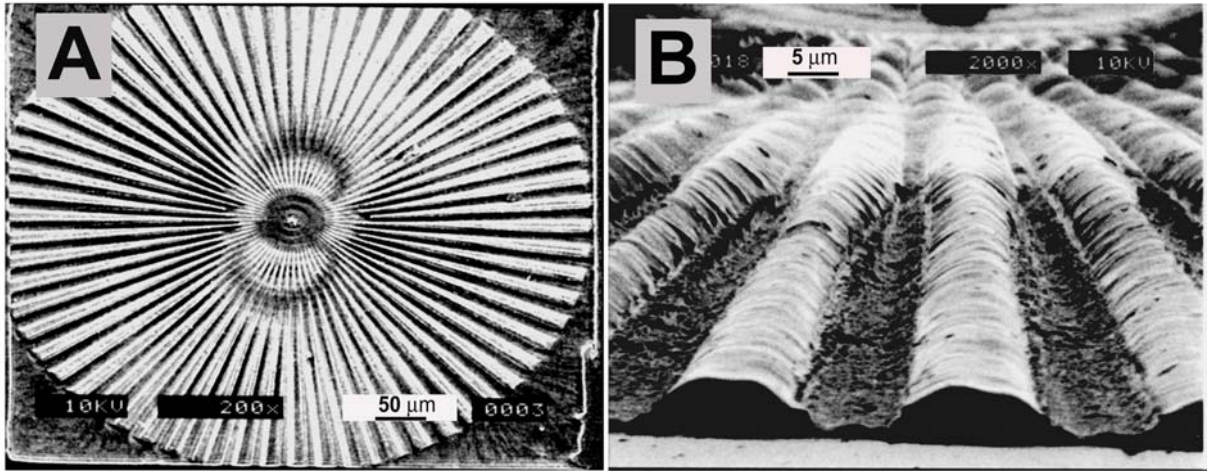


**Fig. 4-15 SEM picture of Siemens star etched in quartz by LIBWE using KrF excimer laser (248 nm, 20 ns) as irradiation source, 0.4 M pyrene in acetone solution as etchant and 700 laser pulses**

The SEM picture of the Siemens star reveals a clear etching without any pronounced cracking of the quartz. From the analysis of the SEM images (Figure 4-15 B) it is possible to resolve lines with a width of  $\leq 2 \mu\text{m}$ , which is up to now the best experimentally obtained result of the combination of LIBWE with projection of a DGTPM. The present limitation is most probably due to the simple optical imaging setup rather than with the etching of quartz by LIBWE. The distance between the imaging lens and the sample, which corresponds to the sharp image of the Siemens star, is also used for the fabrication of Fresnel micro-lenses.

A first example of a Fresnel micro-lens fabricated in quartz by LIBWE and projection of a DGTPM and its line scan are shown in Figure 4-16.

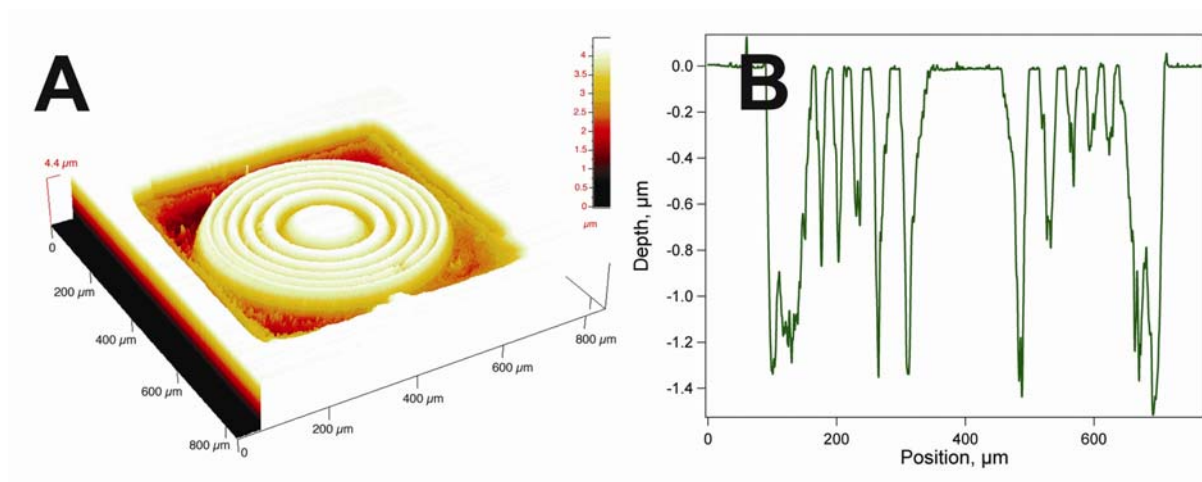


**Fig. 4-16 3D profilometer image of a Fresnel micro-lens etched in quartz by LIBWE (A) and its line scan (B)**

The quartz Fresnel micro-lens with a diameter of 500  $\mu\text{m}$  was fabricated with a XeCl excimer laser fluence of  $1.1 \text{ J/cm}^2$  and by using the 0.4 M pyrene in acetone solution. The line scan of the Fresnel lens (shown in Fig 4-16 B) reveals a plateau in the center which is not etched. This is due to the fact, that the modulated laser fluence in this area is well below the threshold fluence of quartz for this solution. It is also necessary to remember, that the DGTPM which encodes the Fresnel and Siemens star structures were utilized for the fabrication of the complex structures in polyimide and were not optimized for LIBWE. Nevertheless, it is still possible to fabricate high quality micro-Fresnel lens in quartz by this technique and this DGTPM if a 2 M pyrene in THF solution as etchant is used and average laser fluence of  $1.5 \text{ J/cm}^2$  and 50 laser pulses were applied. The 3 D image of the Fresnel lens in quartz and the line scan are shown in Figure 4-17.

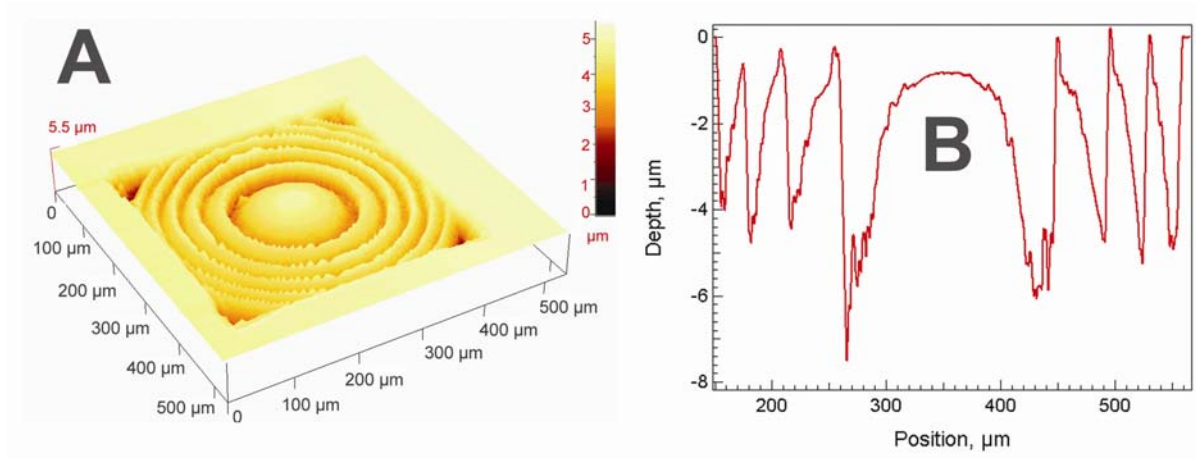


**Fig. 4-17 3D image (A) and horizontal scan (B) of the quartz Fresnel micro-lens fabricated by LBWE and projection of DGTPM**

The diameter of the quartz Fresnel micro-lens is 450 μm. The line scan of a Fresnel micro-lens (shown in Figure 4-17 B) presents the typical Fresnel lens features: i.e. parabolic depth profile in the center and triangular shapes on the lens sides. As already mentioned above, the combination of LIBWE and projection of a DGTPM allows us to fabricate complex structures not only in quartz, but also in other UV transparent materials. The profilometer scan of a Fresnel micro-lens fabricated in BaF<sub>2</sub> and its line scan are shown in Figure 4-18.

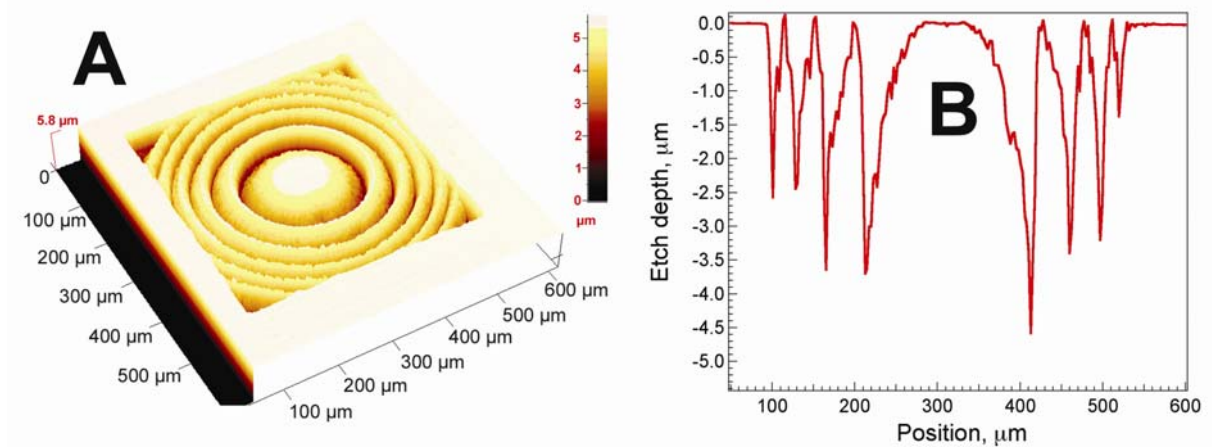


**Fig. 4-18 3D image (A) and the line scan (B) of Fresnel micro-lens in BaF<sub>2</sub>.**

The BaF<sub>2</sub> micro-lens (shown in Figure 4-18) is fabricated with an average XeCl excimer laser fluence of 1 J/cm<sup>2</sup> and 100 laser pulses using a 0.4 M pyrene in acetone solution as an etching media. Although the etch roughness is higher compared to quartz, which suggests



that this micro-lens may not be suitable for the focusing of UV laser light. Nevertheless, this lens could be utilized as a diffractive optical component in the near Infrared wavelength range. This is a first demonstration, that the combination of LIBWE and projection of a DGTPM can be applied for the fabrication of complex three dimensional components in brittle materials such as  $\text{BaF}_2$ , which is extremely difficult to achieve by other commercial techniques.

The goal of this work was, as discussed above, to fabricate arrays of micro-lenses in quartz which can be utilized for UV laser beam shaping and homogenizing applications. For this reason arrays of micro-lenses in quartz are fabricated using the step and repeat technique. The fill factor (ratio between area filled with the micro-lenses to the area without) in micro-lens array must be as high as possible. One way to achieve this requirement is the utilization of a hexagonal packing of micro-lenses, as shown in Figure 4-19 B.

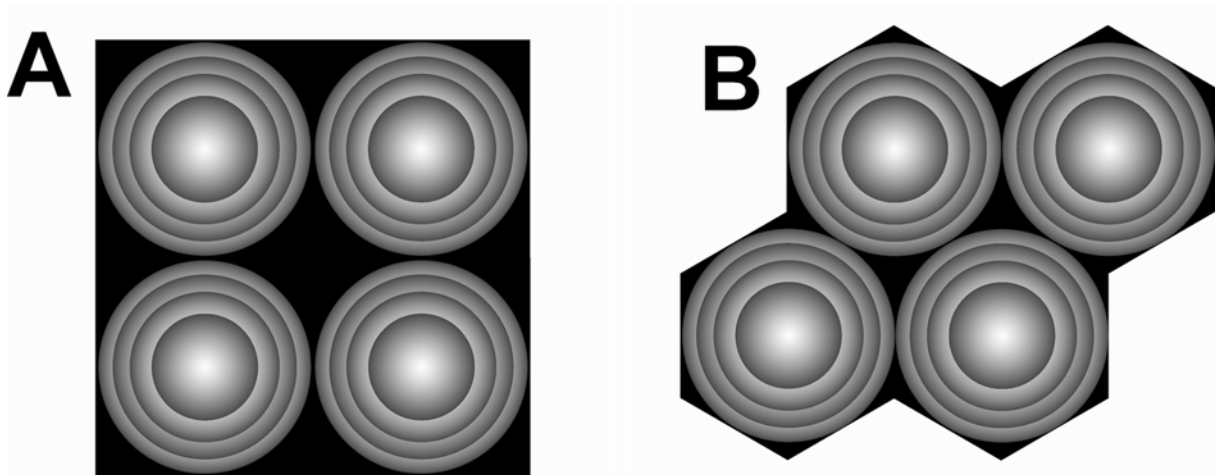


**Fig.4-19 Rectangular (A) and hexagonal (B) packing of Fresnel micro-lenses in array**

The fill factor in a orthogonal lens array (shown in Figure 4-19 A) is 75 %, while the hexagonal packing of the micro-lenses (shown in Figure 4-19 B) increases this factor up to 91 %. A 100% fill factor of the hexagonally packed micro-lens arrays in photoresist was demonstrated by Lin et al [98]. In principle, this can be also achieved with the projection of DGTPM and LIBWE technique, but this task was out of the scope of this work.

The hexagonal mask was cut from white paper and was placed in at a distance of 1 mm behind the DGTPM. This mask is aligned is such way, that the round shape of the DGTPM fits exactly in the hexagonal shape of this mask. The adjustment of both masks is achieved

---

with a mechanical micrometer x-y-z stage, by carefully inspecting the ablated images of the Fresnel micro-lens on polyimide which is placed instead of quartz in the process chamber.

A fragment of 20x22 Fresnel lens array in quartz fabricated by LIBWE and projection of DGTPM is shown in Figure 4-20.

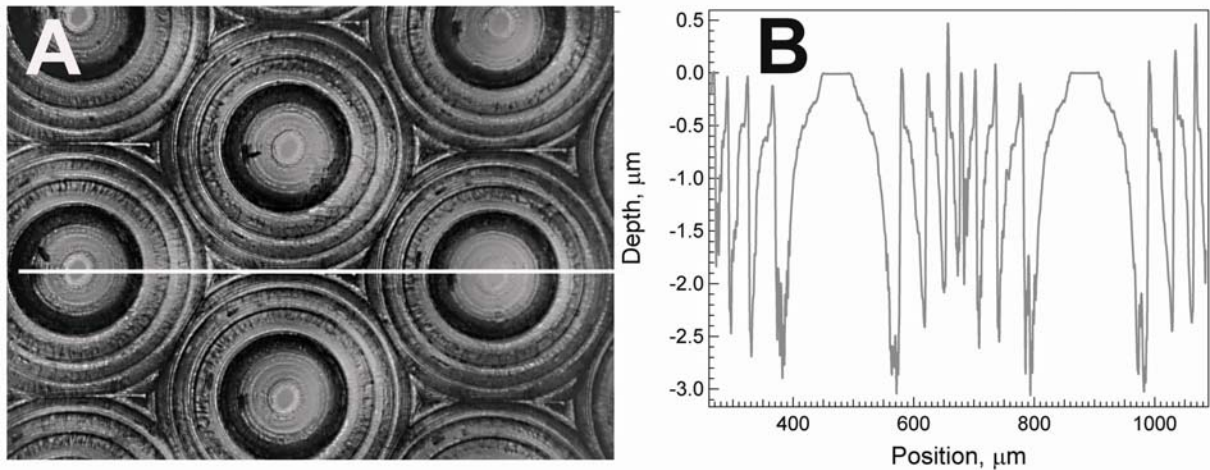


**Fig. 4-20 Optical image (A) and the line scan (B) of Fresnel micro-lens array in quartz**

Each Fresnel micro-lens in the array (shown in Figure 4-20) is fabricated using a 1M pyrene in THF solution. The average XeCl excimer laser fluence was  $2.9 \text{ J/cm}^2$ , while the number of the laser pulses for each lens was 80. Although Fresnel micro-lens arrays fabricated in quartz (shown in Figure 4-20) are suitable for beam homogenizing of UV lasers, the line scan of the micro-lens has still underdeveloped areas at the lens pupil center. This plateau is due to the fact, that the DGTPM was not optimized for LIBWE.

The etch rates, roughness of the etched features and number of the incubation pulses are very important for the fabrication of high quality micro-lenses. For this reason careful studies of the etching of quartz by LIBWE were performed (chapter 3). The results of these studies are included in the design of the DGTPM which encodes the lens shape considering all above mentioned factors. With these DGTPM a high quality micro-lenses in quartz can be fabricated.

A new DGTPM was designed for the fabrication of high quality micro-lenses, which includes the etch threshold and etch rates in the design, of a plano convex lens shape. The diffraction efficiency of the mask was selected from 50 to 90 %, in order to fit the requirements for the etching threshold and the etch rate of quartz by LIBWE. The

reduction of the modulation depth is achieved by simple decrease the depth of the DGTPM structures. The depth of the DGTPM in this case is 175 nm for using 308 nm, instead of 300 nm. This allows us to encode a fluence range from 1.2 to 1.8 J/cm<sup>2</sup>, where the lowest etch roughness and a linear etch rate behavior is obtained for 1.4 M pyrene in THF solution (see chapter 2). A 3 D image of the quartz plano convex micro-lens array is shown in Figure 4-21 A.

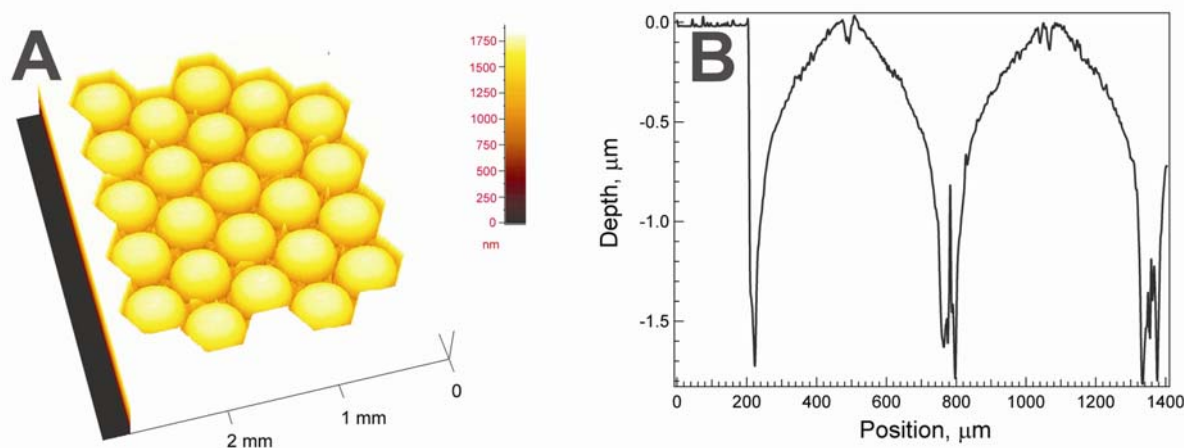


**Fig. 4-20 3D image (A) and the line scan (B) of plano convex micro-lens array in quartz.**

Each of the plano-convex micro-lenses is fabricated by using an average modulated XeCl excimer laser fluence of 1.8 J/cm<sup>2</sup> and by applying 40 laser pulses at each position. The diameter of each micro-lens in the array is 560 μm. The line scan of the micro-lens (shown in Figure 4-21 B) represents a parabolic lens shape. The top of the micro-lenses are slightly rough. This can be due to the imperfection of the laser beam profile and contributions of the incubation effect. The etch roughness is relatively low  $\leq 50$  nm, except the roughness at the bottom of the structures, where sharp re-solidified quartz features are visible. This suggests, that the DGTPM can be further optimized in order to fit the etching requirements.

#### ***4.6 Micro-lens test: measuring of the focal length***

The first test of the micro-lens arrays was the measurements of the focal length of the MLA's. The focal length is a very important parameter for the application of the MLA's as beam homogenizers. The focal length can be evaluated from the micro-lens depth profile (shown in Figure 4-20B for the Fresnel micro-lens array and Figure 4-21B for the plano convex micro-lens array) using following equation 38 [8]:



$$f = \frac{\frac{h}{2} + \frac{D^2}{8 \cdot h}}{(n-1)} \quad (38),$$

where  $h$  is the distance from the midpoint of an arc to the midpoint of its cord, also known as lens sagitta,  $D$  is the diameter of the micro-lens and  $n$  is the refractive index of quartz ( $n=1.458$  @308 nm).

The lens sagitta and pupil diameter of the Fresnel micro-lenses are  $h=2.5 \mu\text{m}$  and  $D=180 \mu\text{m}$  (shown in Figure 4-20). This corresponds to a focal length of each micro-lens in the Fresnel lens array of **f=3.9 mm**. The lens sagitta and diameter of the plano convex micro-lenses (shown in Figure 4-21B) are  $h=1.5 \mu\text{m}$  and  $D=560 \mu\text{m}$ , respectively, which suggest, according to equation 38 a focal length of **f=57 mm**. Another approach is to measure the focal length experimentally, using a setup illustrated in Figure 4-22.

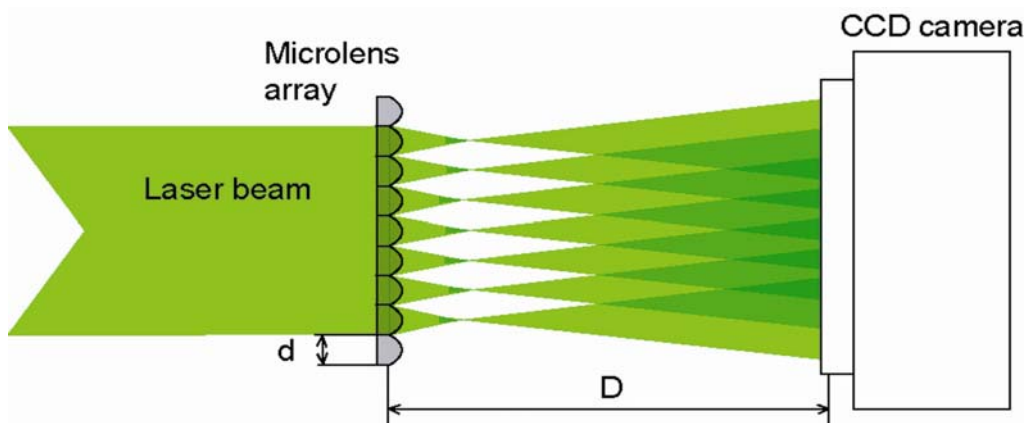


**Fig. 4-22 Experimental setup for measuring of the focal length of the micro-lens array**

The focal length of the micro-lens array is measured in two steps: firstly the images of the laser beam profile which passes through the MLA at different distances between the micro-lens array and a CCD camera (shown in Figure 4-23) were obtained.

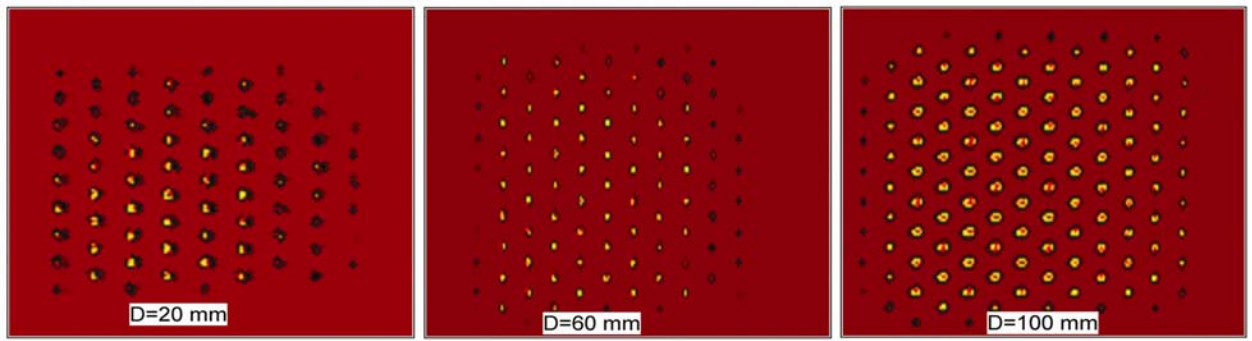


**Fig. 4-23** CCD images of the XeCl excimer laser beam with quartz plano-convex micro-lens array at various distances  $D$ .

The images which, shown in Figure 4-23, were analyzed by a home made PC program developed with IGOR. The line scan of the speckle is fitted by a Gaussian function. From this fit the width of each speckle is evaluated. The averaged width of the speckles (shown in Figure 4-24) at each distance  $D$  is obtained by averaging the width of 5 randomly chosen speckles.

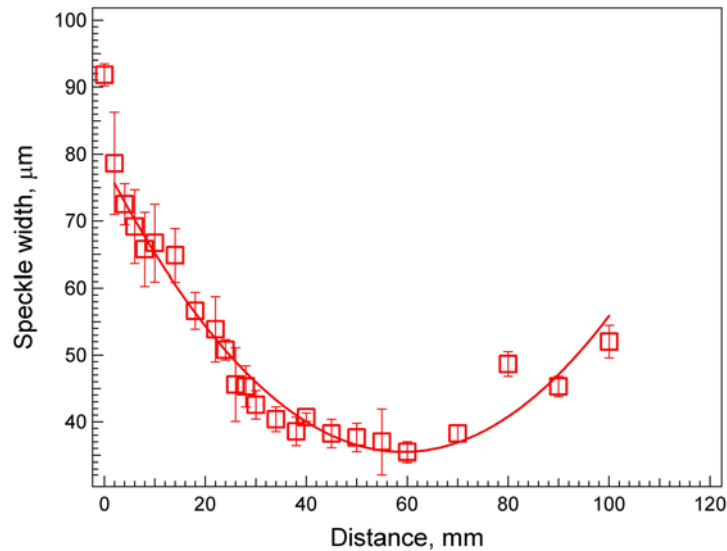


**Fig. 4-24** The width of the features of the focused laser beam with a plano-convex micro-lens array at various distances  $D$ .

The behavior of the width of the speckles at various distances  $D$  can be fitted by the parabolic function:

$$y = y_0 + a \cdot (x - x_0)^2 \quad (39),$$

where  $y$  represents the width of the features obtained at the distance  $D$ ,  $y_0$  is equal to the minimum width obtained at the focal plane ( $y_0=35\text{ }\mu\text{m}$ ),  $a$  is fitting constant and  $x_0$  is the focal length of the micro-lens array.

The value of the measured focal length for the quartz plano convex micro-lens array is **60 mm**, which agrees quite well with the result obtained from the its line scan (shown in Figure 4-21 B). The experimentally measured focal length of the Fresnel micro-lens array is **5 mm**, which corresponds also well with the values observed from its line scan (shown in Figure 4-20 B). The combination of LIBWE and projection of a DGTPM allows us to fabricate micro-lenses with a diameters ranging from **250 micrometer** up to a **few millimeters** by simple adjusting the distances between the DGTPM and the imaging lens and between the imaging lens and the sample. The focal lengths of the micro-lenses fabricated in quartz can be varied from **5 mm** (Fresnel lens) to **150 mm** (plano convex lens) and depend on the number of applied laser pulses [42, 99, 100].

#### ***4.7 Laser beam shaping with Random Phase Plate: results***

The Random Phase Plates and arrays of micro-lenses are tested as beam homogenizers for high power Nd:YAG and excimer laser beams. The RPP introduce, as discussed above, randomness in the phase of the incoming beam. This creates an effectively smoother intensity distribution by overlapping many 0 or  $\pi$  phase shifted beamlets at the focal plane of the collecting lens, as shown in Figure 4-3. The intensity loss with a RPP is typical in the range of 15% and is due to the diffraction effects of the RPP and reflections from the quartz plate. An intensity profile of a Raman shifted Nd:YAG laser (1900 nm, 5 ns) without RPP and at different distances ( $D$ ) behind the RPP is shown in Figure 4-25. The focal length of the collecting lens was 230 mm.

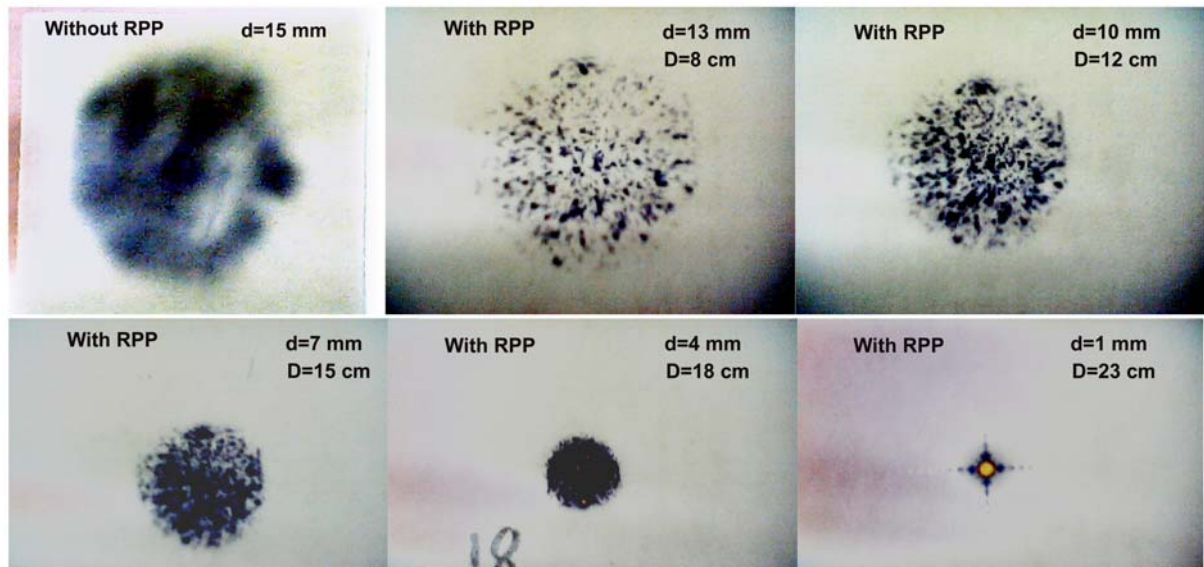


**Fig. 4-25 Raman shifted Nd:YAG intensity profile without and with RPP at different distances behind the collecting lens of focal length of 23 cm.**

The distance behind the collecting lens is marked as  $D$ , and the diameter of the focused laser beam is lettered as  $d$ . The RPP was set in front of the collecting lens with a distance of 5 cm. The beam is split into many beamlets at a distance of 8 cm behind the collecting lens, as shown in Figure 4-25. These beamlets are superimposed behind the collecting lens. A homogeneous laser beam profile is obtained at the distance of 18 cm behind the collecting lens. The homogeneous beam is detectable at the focal plane of the collecting lens ( $D=23$  cm). The weak diffraction patterns are also visible at the focal plane of the collecting lens. Nevertheless, the beam profile is much more homogeneous with the RPP compared to that obtained without RPP. A new RPP for a quadrupled Nd:YAG laser (266 nm) is fabricated. This laser is very important for the structuring of UV transparent materials and photopolymers. The depth of the structures in this RPP is 250 nm, which corresponds to the  $\pi$  phase shift for 266 nm as irradiation wavelength. The beam profile of a quadrupled Nd:YAG without and with the RPP is shown in Figure 4-26 for an ablation pattern in polyimide.

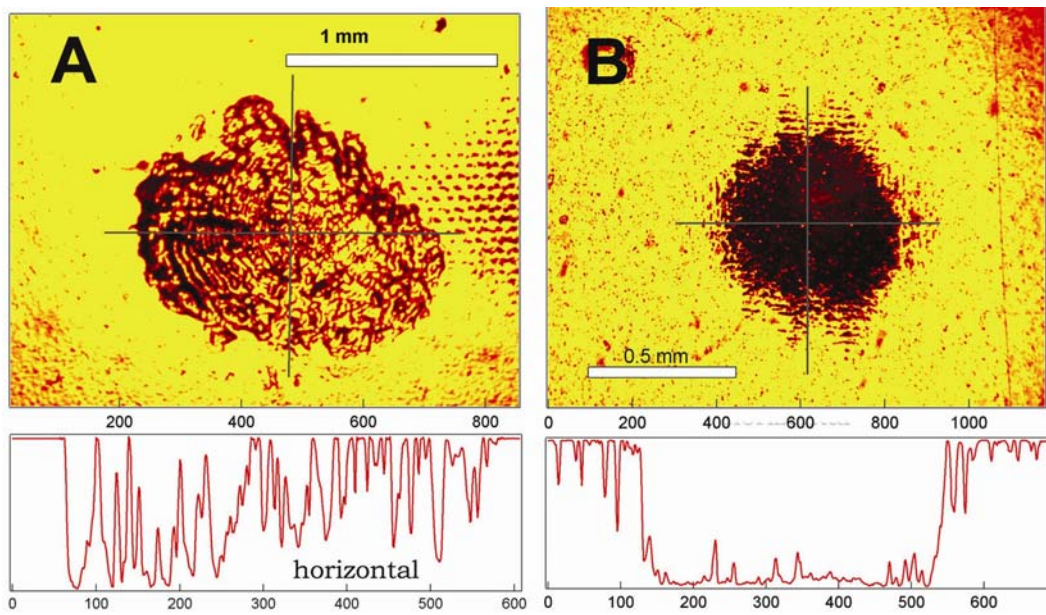


**Fig. 4-26 Beam profile of 4 th harmonic Nd:YAG laser without (A) and with (B) RPP.**

The beam profile shown in Figure 4-26 is the transfer of the beam intensity profile to the polymer through laser ablation. The beam profile close to the focal plane of the collecting lens (shown in Figure 4-26 as B) is more homogeneous compared to the beam without RPP. The RPP, however, introduces small periodical features, which are most probably due to interference effects, which will be explained in details later.

The Random Phase Plate is, as discussed above, a binary plate which produces either 0 or  $\pi$  phase jumps and depends, therefore, on the applied laser wavelength. For instance, a RPP fabricated for 1064 nm laser wavelength does not work with the doubled Nd:YAG laser which emits in the visible region (532 nm). The dependence of the RPP on the irradiation wavelength and pulse length, was tested with a femtosecond Ti:Sapphire laser, which emits over a broad spectral range. The craters of the ablated silica without and with RPP are shown in Figure 4-27.

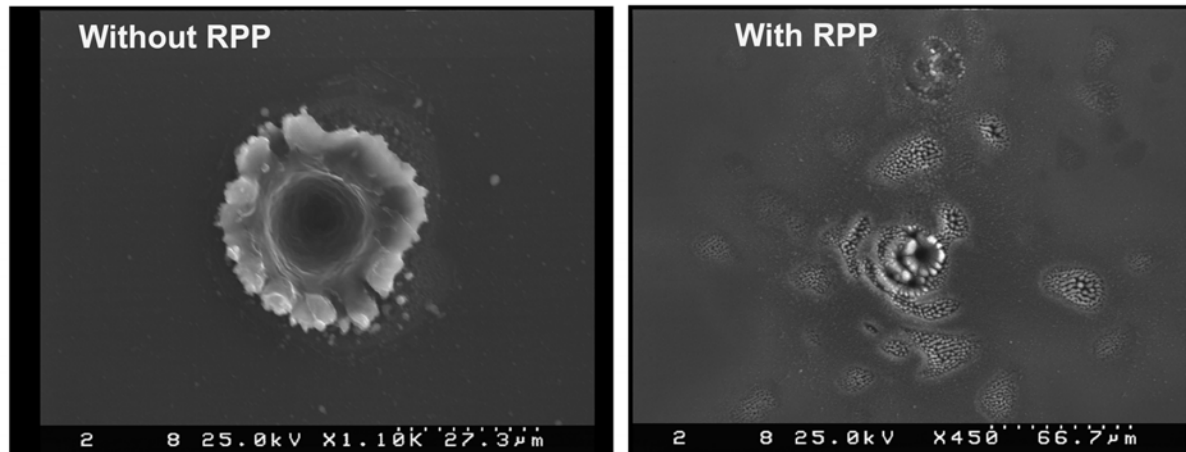


**Fig. 4-27 SEM images of ablated craters in silica by femtosecond Ti:Sapphire laser without and with RPP**

The beam profile of the Ti:Sapphire laser with a RPP at the focal plane of the collecting lens is reshaped non-homogeneously (shown in Figure 4-27): a sharp peak is visible in the center surrounded by small satellite features around the crater. The area of silica structured without RPP shows nicely ablated crater. The bad beam profile of the femtosecond laser with the RPP may be due to the very broad wavelength range ( $\Delta\lambda \geq 200$  nm) of the laser, for which the RPP is not working properly. The values of the phase shift produced by the RPP are altering continuously between 0 and  $1.5\pi$  for femtosecond lasers. For this reason it can be concluded, that a RPP is a bad alternative for homogenizing of Ti:Sapphire fs lasers, but they can be used for homogenizing other lasers such as Nd:YAG or excimers, which emit a single wavelength.

#### ***4.8 Laser beam shaping with micro-lens arrays: results***

Quartz micro-lens arrays can be utilized independently on the applied wavelength and over broad wavelength range from UV to the near IR (250-1100 nm), where quartz is transparent. They are effectively working with quadrupled Nd:YAG laser, which emit at 266 nm, as well as with the fundamental of a Nd:YAG laser at 1064 nm. The transmission of a single quartz micro-lens array is in the range of 80 % and does almost not depend on the laser wavelength, for which it used. The losses of 20% are due to the roughness of the fabricated micro-lenses and the reflection of the quartz plate. These MLA's can be used, as discussed above for homogenizing Nd:YAG and excimer lasers, which are applied in our

laboratory. An experimental setup for a homogenizing a quadrupled Nd:YAG laser, is shown in Figure 4-1.

This technique requires a quartz micro-lens array and a collecting lens. For the first tests a micro-lens array which consists of 22x22 micro-lenses with a diameter of 500  $\mu\text{m}$  and focal length of 60 mm was used. The collecting lens with a diameter of 50 mm and focal length of 150 mm was applied. The beam diameter at the homogenizing plane must be equal to 2 mm, according to equation 26, when the beam diameter of the laser is 7 mm. The beam profile at the focal plane of the collecting lens and before the micro-lens array (shown in Figure 4-28) is measured with a CCD camera which consists of a special fluorescence screen placed in front of the camera. This fluorescence screen converts the incoming UV laser light into visible radiation.

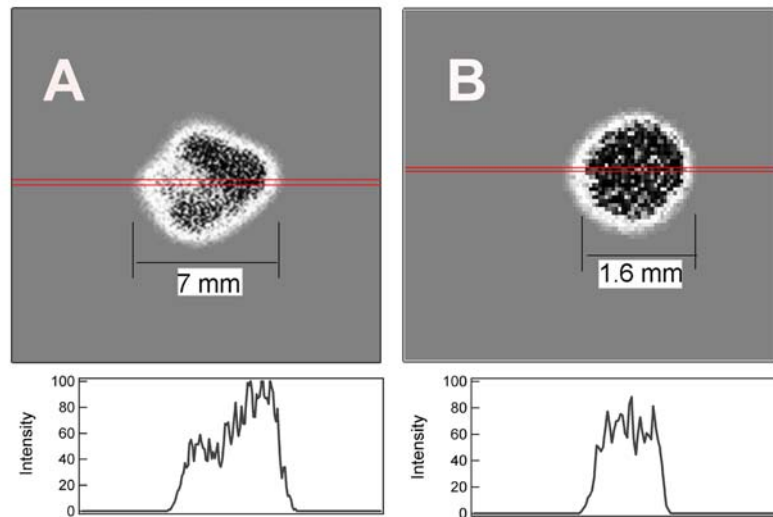


**Fig 4-28 CCD images of quadrupled Nd:YAG beam profile without (A) and with (B) quartz micro-lens beam homogenizer and its line scans.**

A clear improvement of the Nd:YAG laser beam profile is obtained with the quartz micro-lenses (as shown in Figure 4-28). However, the line scan profile suggest the existence of the energy fluctuations in the intensity profile of the homogenized beam (shown in Figure 4-28 B), which are in the range of 10% (RMS). These energy fluctuations are most probably due to interference, which results from the division of the laser beam into a number of beamlets. The fluorescence screen which is used in our experiments limits the resolution of the image and therefore the interference patterns can not be clearly detected. Therefore a polyimide sample was used, which is placed in the focal plane of the collecting



lens, where a homogeneous beam profile is expected. An image of the ablated crater in polyimide using the plano convex micro-lens arrays with a diameter of each lens of 500  $\mu\text{m}$  is shown in Figure 4-29.

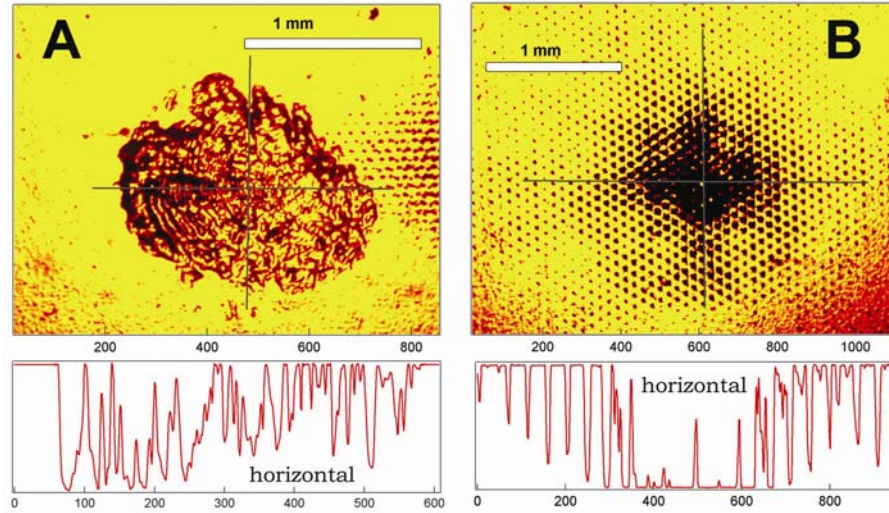


**Fig. 4-29 Picture of ablated area in polyimide without (A) and with (B) beam homogenizer**

The ablated area in polyimide clearly reveals periodically spaced patterns in the homogenized laser beam profile. Similar interference effects with MLA are also obtained with excimer lasers [89]. This effect is described in detail in the book of F. Dickey and S. Holswade [88]. The interference in the homogenized plane is, according to the authors, the result of the splitting of an incoming beam intensity into many beamlets. This effect depends on the spatial coherence of the laser: a spatially incoherent laser will not produce interference patterns, and the laser with high spatial coherent will produce strong interference effect. The beamlets which are slightly different in phase due to imperfection of the micro-optics and diffraction through the micro-lens pupil will interfere with each other at their superposition plane, which is the focal plane of the collecting lens (and also coincidences with the homogenizing plane). Thus, an interference effect in the case of homogenizing strongly coherent lasers such as Nd:YAG lasers can not be avoided, but it can be minimized. The period of the interference patterns ( $P$ ) depends on the applied laser wavelength ( $\lambda$ ), the focal length of the collecting length ( $F$ ) and is directly proportional to the diameter of the micro-lenses ( $d$ ) which is described by equation 40 [88]:

$$P = \frac{\lambda \cdot F}{d} \quad (40).$$



The expected period between the interference patterns for the previously described beam homogenizer and for a laser wavelength of 266 nm is **79  $\mu\text{m}$** . The measured pattern period is  **$P=78 \mu\text{m}$**  which is obtained from the analysis of the depth profile of the etched features in polyimide. This agrees very well with the values utilized from equation 40. The period of the interference patterns can be reduced with an increase of the micro-lenses diameter or with a decrease of the focal length of the collecting lens. However, the short focal length lens has some drawbacks: firstly the area of the homogenized beam will decrease with decreasing focal length of the collecting lens (as it is suggested by equation 29). Secondly, the homogenized beam will have a large divergence behind the homogenizing plane which will cause a serious problem in case of imaging objects placed at the homogenizing plane. Better results will therefore be obtained by an increase of the micro-lens diameter with the same focal length of the collecting lens. An increase of the diameter of the micro-lens will result in a decrease of the period of the interference patterns and an enhancement of the diameter of the beam at homogenizing plane. The largest diameter of the micro-lenses which can be currently fabricated by LIBWE and projection of DGTPM is 1 mm for an experimental set up, which is shown in Figure 4-11. An array of 10x10 plano convex micro-lenses fabricated in quartz with a 1.4 M pyrene in THF solution as etchant and with a XeCl excimer laser fluences of  $1.3 \text{ J/cm}^2$  is shown in Figure 4-30.

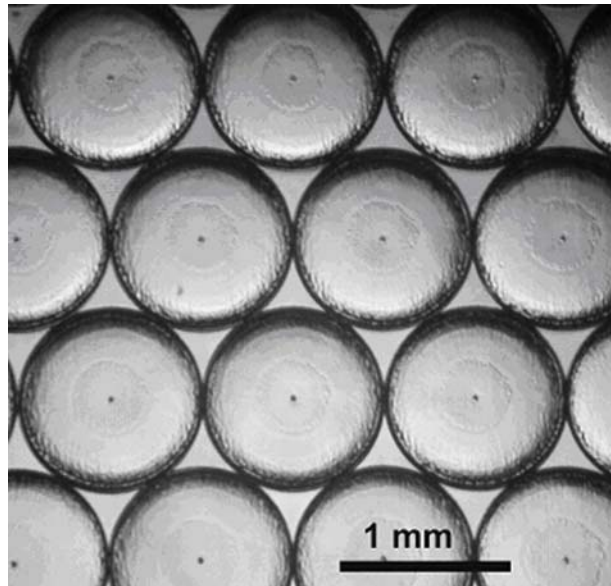


**Fig. 4-30 Optical image of fragment of 10x10 quartz micro-lens array with a diameter of 1 mm.**

The diameter of each micro-lens is 1 mm, while the focal length of the micro-lenses is 70 mm. A beam profile of a quadrupled Nd:YAG laser with this micro-lens array and a collecting lens of 150 mm focal length is shown in Figure 4-31.

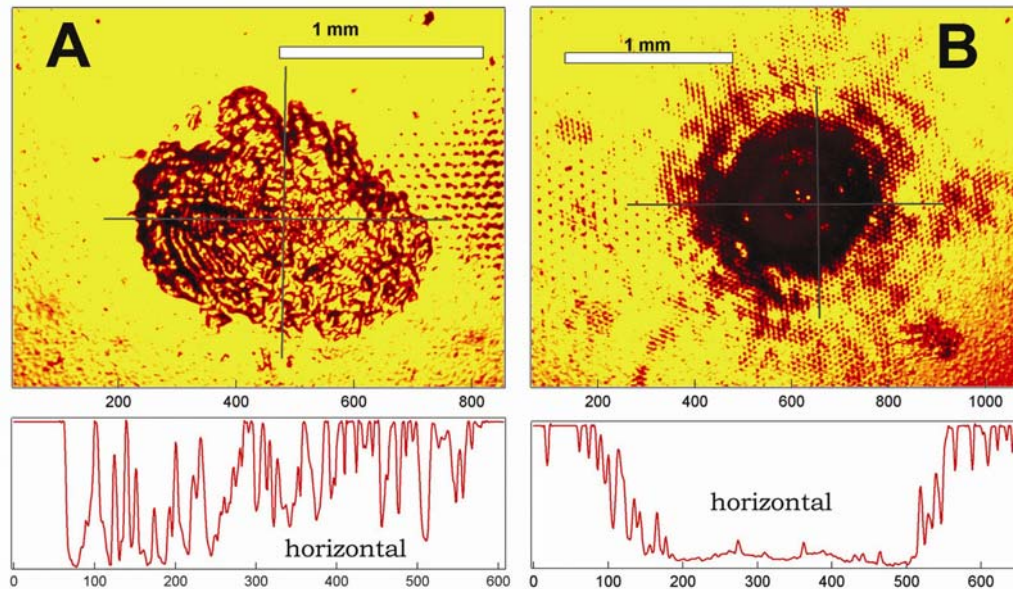


**Fig. 4-31 Quadrupled Nd:YAG beam profile at homogenized plane using 10x10 micro-lens array with a diameter of 1 mm**

The beam profile of the quadrupled Nd:YAG laser is clearly better when the MLA with the large diameter of the micro-lenses as beam homogenizer is applied. The period of the interference patterns in the case of large diameter micro-lenses decreases to **25  $\mu\text{m}$** . However, the expected effect of an increase of the spot size with an increase of the diameter of micro-lenses was not obtained. The reasons for this observation are not clear at the moment.

The beam homogenizer, which consists of a single micro-lens array and a collecting lens can be used not only for homogenizing of Nd:YAG lasers, but also for improving the quality of excimer lasers beams. The beam profile of a XeCl excimer laser with and without homogenizer is transferred into polyimide. The homogenizer consists of a 10x10 micro-lens array with the diameter of each micro-lens of 1 mm, focal length of 70 mm and a collecting lens with a focal length of 150 mm. The results are shown in Figure 4-32.

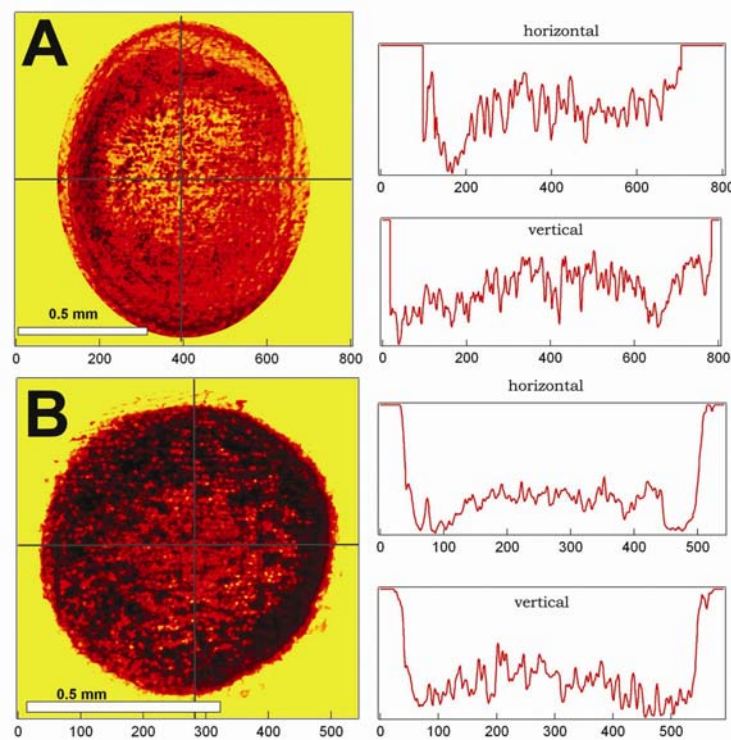


**Fig. 4-32 Beam profile of the XeCl excimer laser without (A) and with (B) beam homogenizer**

The XeCl excimer laser beam profile at the homogenizing plane reveals a more homogenous intensity distribution and has a round shape (shown in Figure 4-31) compared to that obtained without homogenizer.

A better improvement of Nd:YAG and excimer laser beam profiles can be expected with the setup described in Figure 4-2. Here, a second micro-lens array is placed in the focal plane of the first micro-lens array and the collecting lens is placed on the focal plane of the second micro-lens array. An image of the beam profile on polyimide at the homogenized plane of 150 mm collecting lens obtained by using this approach is shown in Figure 4-33.

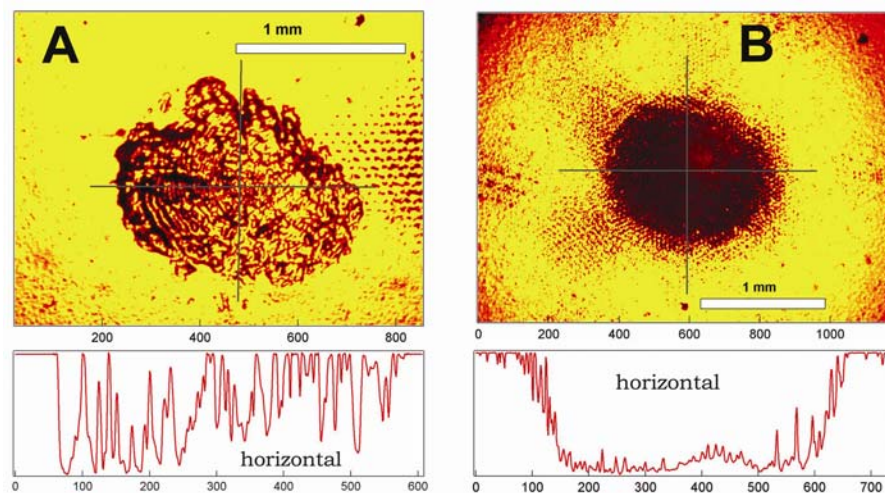


**Fig. 4-33 Quadrupled Nd:YAG beam profile at a homogenized plane using two 10x10 micro-lens array with a diameter of 1 mm and a focal length of 50 mm and  $f=150$  mm collecting lens**

This approach results in the best results for homogenizing the laser beam profile of all tested homogenizing approaches. However, the loss in the laser intensity using this approach is 40%. This is mainly due to the reflection of the micro-lens arrays and imperfection from the fabrication. These losses can be reduced by adding antireflective coating on the MLA's and by improving the DGTPM and LIBWE fabrication process.

All three beam shaping and homogenizing approaches reveals clear improvement of the laser beam profile. The improvement of the beam shapers and homogenizers is an ongoing project.

## Outlook

The combination of LIBWE and projection of a DGTPM open a new way for the fabrication of the complex structures in quartz and other UV transparent materials.

One of the newest ongoing project is the fabrication an array of the micro-pyramid (micro-prisms) structures in quartz as is shown in Figure 5-1.

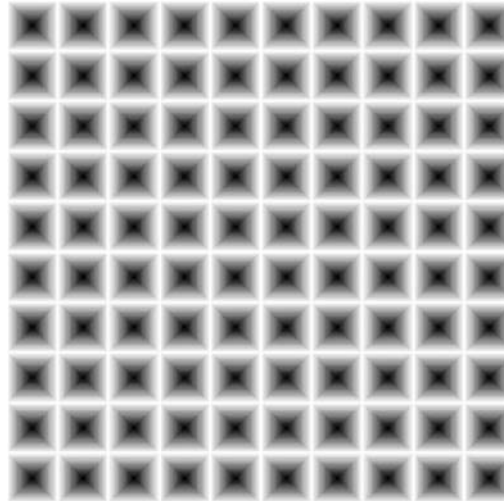


**Fig. 5-1 The design of the pyramid array.**

Such structures are very difficult to fabricate by other techniques. The micro-pyramid array in quartz can be used as a master for the fabrication of the pyramid structures in plastics by replication techniques. Such pyramid shaped micro-structures are very interesting for the car lighting industry. But for these structures a new DGTPM masks must be fabricated. This is also an ongoing project.

The second very interesting application of the LIBWE process is the fabrication of diffractive optical elements (DOE) in quartz. The DOE's are binary complex structures which are very attractive in the modulation of the incoming laser beam in three spatial dimensions. The DOE's can be applied as beam shapers or beam homogenizers. They can also encode complex structures, which can only be visible in the far field when the light passes through the DOE structures. The idea of the light modulation by a DOE is illustrated in Figure 5-2.

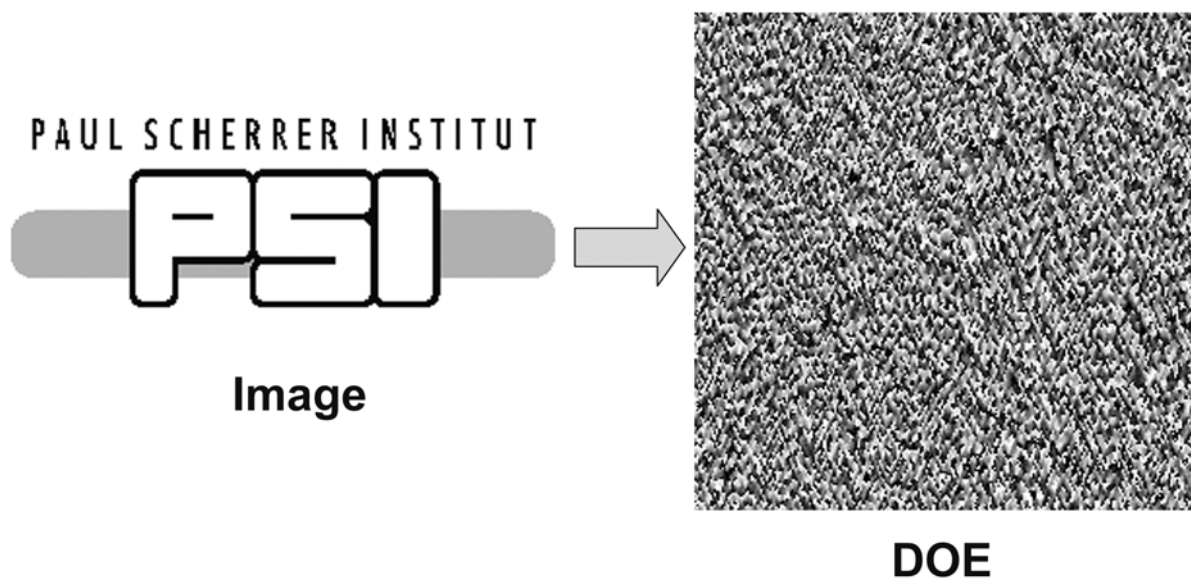


**Fig. 5-2 An example of the image encoded in the DOE.**

The fabrication of a DOE which encodes the images is rather complex process. The gray scale level of each image pixel is encoded by the phase shift of the light which passes through the DOE. This is achieved by encoding the depth of the features which are etched in quartz. The DOE's consists of many features with a typical size of  $7\text{ }\mu\text{m}$ , which depths vary continuously between 0 and 600 nm in order to produce a phase shift between 0 and  $\pi$  for a 632 nm irradiation wavelength. The depth of the etched features must be precisely fabricated and the etch roughness must be as low as possible. For example the roughness of the etched features for a DOE's which encodes an image with 16 colors must be better than 30 nm!

The first quartz DOE was fabricated by  $\text{F}_2$  excimer laser ablation [101]. However, this technique requires an additional cleaning process. An alternative method for the fabrication of the DOE's can be the combination of LIBWE and projection of a square mask. But for the fabrication of the DOE's is it necessary to design a new program which controls the movement of the high precision xyz stage and the number of the laser pulses. This is a very interesting project which allows also us to design and fabricate a DOE in quartz which can be used as a novel beam homogenizer.

## Summary

Laser Induced Backside Wet Etching is a promising *one step* micromachining process, which allows us to create simple and complex structures in *quartz, CaF<sub>2</sub>, BaF<sub>2</sub> and sapphire*.

The etch rates of UV transparent materials varies from *5 nm to 1 μm* for quartz, and from *400 nm to 3 μm* for BaF<sub>2</sub>, CaF<sub>2</sub> and sapphire. The lowest roughness of the etched features in quartz is  $\leq 20\text{ nm}$ , while in the case of CaF<sub>2</sub>, BaF<sub>2</sub> and sapphire the etch roughness is the range of *400 nm*.

The lowest energy density for which etching can be detected using a 1.4 M pyrene in THF solution as an "etchant" is: *0.5 J/cm<sup>2</sup>* for quartz, *0.6 J/cm<sup>2</sup>* for BaF<sub>2</sub>, *1 J/cm<sup>2</sup>* for CaF<sub>2</sub> and *1.6 J/cm<sup>2</sup>* for sapphire.

The mechanism of LIBWE is very complex and consists of several steps:

*a) Strong absorption of the laser light.*

The incoming laser light is absorbed by the solution, which is in contact with the transparent material. The intensity of the laser light is absorbed with a  $\leq 1\mu\text{m}$  layer of the liquid.

*b) Conversion of the light to temperature.*

The excited molecules in the solution create a high temperature jump at the material-liquid interface due to the fast non-radiative vibrational-rotational relaxation processes.

The temperature rise at the material-liquid interface results in a number of effects:

- 1) Heating/melting/boiling of the UV transparent material surface.*
- 2) Rapid explosive evaporation of the solution, which results in the formation of high pressure shock waves and laser induced bubbles.*
- 3) Thermal decomposition of the solution and formation of a carbon film on the surface of the hot material.*
- 4) Plasma formation in solution.*

All these effects play a very important role in the LIBWE process.

The value of the temperature rise at the material-liquid interface strongly depends on the applied laser fluence. The T-jump increases linearly with the laser fluence, *according to a theoretical model developed in this work.*



Three different fluence ranges can be determined, while structuring of the UV transparent materials by LIBWE with a XeCl excimer laser (308 nm).

### **Low Fluence Range**

1. The temperatures, generated at the material-liquid interface *are below* the melting point of the material.
2. The etching starts after a certain amount of the repetitive laser pulses, typically *>100 (incubation effect)*.
3. The etching of quartz is strongly *influenced by the creation of carbon deposits* which strongly adhere to the surface of the hot material.
4. *Low etch rates and a high etch roughness* are obtained.
5. Chemical modification of the etched surface (*carbonization*) *without modification in the bulk material is obtained in this fluence range*.

### **Intermediate Fluence Range**

1. Laser Induced temperatures *reach* the melting point of the material.
2. Etching starts after  $\leq 5$  repetitive laser pulses.
3. The removal of the molten material is associated with a *pressure jump* generated from the rapid expansion of the shock wave which removes the *molten* material mechanically.
4. Higher etch rates compared to the low laser fluences are detected.
5. *The lowest etch roughness of  $\leq 20$  nm for quartz is obtained*.
6. *Less carbonization* of the etched surface is detected, but a *chemical modification of a thicker layer of material* (changes from the  $\alpha$ -quartz to the tridymite phase of quartz) is obtained.

### **High Fluence Range**

1. The temperature at the material-liquid interface is very high.
2. The material may evaporate directly.
3. Generation of plasma in solution.
4. The etching is associated with *high pressure jumps* generated by the shock waves and the *plasma* process.



5. The etch rates are *much higher* but also *higher etch roughness* are detected as compared to the intermediate fluences.
6. *Less carbonization* of the etched surface, but *chemical modification of the material* (changes from the  $\alpha$ -quartz to the tridymite phase of quartz) is obtained.

The range of fluences where the lowest etch roughness are obtained decrease with a decrease of the etching area. However, no effects on the etch rate and number of incubation pulses with an increase of the etching areas are visible.

Longer XeCl excimer laser pulses >30 ns produce a smaller temperature jump which may not be sufficient to melt the material even in the intermediate laser fluence range. This results in an increase of the threshold fluence and a strong carbon layer formation which influences the etching process.

Only two etch rate slopes are obtained for the KrF (248 nm, 20 ns) excimer laser as irradiation source. The etch rates obtained with this laser are much higher, but the roughness at the intermediate fluence range is higher too. The XeCl excimer laser was therefore selected for the fabrication of micro-optical components.

Two types of laser beam homogenizing methods have been evaluated. The first approach is based on applying a simple binary diffractive optical element, i.e. a Random Phase Plate in combination with a plano convex lens. The second technique requires one or two micro-lens arrays and a plano convex lens. The RPP is easy to fabricate by LIBWE, since this is a binary structures, while the fabrication of micro-lenses requires an additional expensive optical element, i.e. a Diffractive Gray Tone Phase Mask. The necessary time for the fabrication of a RPP and a micro-lens array is approximately the same, if the time for the fabrication of DGTPM is not taken into account. The fabrication time depends mainly on the number of elements, their sizes and laser repetition rate. For example, structuring of an RPP for 266 nm which consists of 32x32 patterns with a size of 250  $\mu\text{m}$  takes approximately 3 hours working with a of laser repetition rate of 8 Hz, which is similar to the fabrication time of 22x22 micro-lens arrays with a diameter of each lens of 500  $\mu\text{m}$  and a focal length of 60 mm. High repetition lasers have been applied for LIBWE and it appears that the maximum possible repetition rate is in the range of 10 kHz, which would allow a very fast fabrication of these elements [102]. The RPP compared to the MLA has one major disadvantage: the RPP works only for a single or very narrow wavelength range,

while micro-lenses can be applied for a different laser wavelengths ranging from 250 nm to 1100 nm. As beam homogenizers both elements show a clear improvement of the beam profile at the homogenizing plane. However, the homogenized beam diameter with the RPP strongly depends on the focal length of the collecting lens and is typically below 1 mm. The diameter of the beam at homogenizing plane obtained by applying the micro-lens arrays depends on the focal length of the collecting lens, the focal length and diameter of the micro-lenses, which can be varied from 0.25 mm up to 1 mm (in our case). The beam profile of the Nd:YAG lasers at homogeneous plane with a MLA consists of the interference patterns with periods depending on the parameters of the micro-lenses. This effect can be strongly reduced with an increase of the diameter of micro-lenses (several mm or bigger). This approach, however, could not be applied for the RPP, where also some interference features in the homogenized plane are visible.

In summary, LIBWE is a very complex process with the aspects which are not completely understood. Nevertheless, it allows the fabrication of three dimensional structures such as micro-optical elements which *work* as beam homogenizer.

---

## References

- [1] S. Sinzinger and J. Jahns: Microoptics (WILEY-VCH GmbH & Co. KGaA, Weinheim, Germany, 2003).
- [2] Wikipedia: History of optics, [http://en.wikipedia.org/wiki/History\\_of\\_optics](http://en.wikipedia.org/wiki/History_of_optics).
- [3] Wikipedia: Lens (optics), [http://en.wikipedia.org/wiki/Lens\\_\(optics\)](http://en.wikipedia.org/wiki/Lens_(optics)).
- [4] Web Science Resources: A brief history of Optics, <http://members.aol.com/WSRNet/D1/hist.htm>.
- [5] W. J. Blaker and P. Schaeffer: Optics. An introduction for Technicians and Technologists (Prentice-Hall, Inc., New Jersey, US, 2000).
- [6] H. P. Herzig: Micro-optics elements, systems and applications (Taylor & Francis Ltd, London, UK, 1997).
- [7] H. Sankur, E. Motamedi, R. Hall, W. Gunning and M. Khoshnevisan: Proc. SPIE **2383**, 179-183 (1995).
- [8] P. Nussbaum, R. Volkel, H. P. Herzig, M. Eisner and S. Haselbeck: Pure Appl. Opt. (UK) **6**, 617-636 (1997).
- [9] P. E. Dyer, A. M. Johnson, H. V. Snelling and C. D. Walton: Appl. Surf. Sci. **186**, 583-587 (2002).
- [10] P. E. Dyer, S. M. Maswadi and C. D. Walton: Appl. Phys. A-Mater. Sci. Process. **76**, 817-822 (2003).
- [11] P. E. Dyer and C. D. Walton: Appl. Phys. A-Mater. Sci. Process. **79**, 721-727 (2004).
- [12] M. Henyk, F. Costache and J. Reif: Appl. Surf. Sci. **186**, 381-384 (2002).
- [13] K. Nagashima, M. Hashida, M. Katto, M. Tsukamoto, M. Fujita and Y. Izawa: Trans. Inst. Electr. Eng. Jpn. C (Japan) **124**, 388-392 (2004).
- [14] H. Varel, D. Ashkenasi, A. Rosenfeld, R. Herrmann, F. Noack and E. E. B. Campbell: Appl. Phys. A-Mater. Sci. Process. **62**, 293-294 (1996).
- [15] J. Ihlemann, B. Wolff and P. Simon: Appl. Phys. A-Mater. Sci. Process. **54**, 363-368 (1992).
- [16] H. Varel, D. Ashkenasi, A. Rosenfeld, M. Wahmer and E. E. B. Campbell: Appl. Phys. A-Mater. Sci. Process. **65**, 367-373 (1997).

- 
- [17] K. Sugioka: Rev. Laser Eng. (Japan) **30**, 226-232 (2002).
- [18] J. Ihlemann and D. Schafer: Appl. Surf. Sci. **197**, 856-861 (2002).
- [19] D. Ashkenasi, M. Lorenz, R. Stoian and A. Rosenfeld: Appl. Surf. Sci. **150**, 101-106 (1999).
- [20] A. Rosenfeld, M. Lorenz, R. Stoian and D. Ashkenasi: Appl. Phys. A-Mater. Sci. Process. **69**, 373-376 (1999).
- [21] B. C. Stuart, M. D. Feit, S. Herman, A. M. Rubenchik, B. W. Shore and M. D. Perry: Phys. Rev. B **53**, 1749-1761 (1996).
- [22] A. Marcinkevicius, S. Juodkasis, M. Watanabe, M. Miwa, S. Matsuo, H. Misawa and J. Nishii: Opt. Lett. (USA) **26**, 277-279 (2001).
- [23] M. Will, S. Nolte, B. Chichkov and A. Tünnermann: Applied Optics **41**, 4360-4364 (2002).
- [24] J. Li, P. R. Herman, X. M. Wei, K. P. Chen, J. Ihlemann, G. Marowsky, P. Oesterlin and B. Burghardt: Proc. SPIE **4637**, 228-234 (2002).
- [25] R. Matz: J. Lightwave Technol. **4**, 726-729 (1986).
- [26] J. Zhang, K. Sugioka and K. Midorikawa: Appl. Phys. A, Mater. Sci. Process. (Germany) **67**, 499-501 (1998).
- [27] J. Zhang, K. Sugioka and K. Midorikawa: Appl. Phys. A, Mater. Sci. Process. (Germany) **67**, 545-549 (1998).
- [28] S. I. Dolgaev, A. A. Lyalin, A. V. Simakin and G. A. Shafeev: Kvantovaya Elektron. **23**, 67-70 (1996).
- [29] S. I. Dolgaev, A. A. Lyalin, A. V. Simakin and G. A. Shafeev: Appl. Surf. Sci. **96-8**, 491-495 (1996).
- [30] J. Wang, H. Niino and A. Yabe: Appl. Surf. Sci. **154**, 571-576 (2000).
- [31] J. Wang, H. Niino and A. Yabe: Appl. Phys. A-Mater. Sci. Process. **68**, 111-113 (1999).
- [32] X. M. Ding, Y. Kawaguchi, T. Sato, A. Narazaki and H. Niino: Langmuir **20**, 9769-9774 (2004).
- [33] R. Böhme, A. Braun and K. Zimmer: Appl. Surf. Sci. **186**, 276-281 (2002).
- [34] R. Böhme, J. Zajadacz, K. Zimmer and B. Rauschenbach: Appl. Phys. A-Mater. Sci. Process. **80**, 433-438 (2005).
-

- 
- [35] X. Ding, Y. Kawaguchi, H. Niino and A. Yabe: Appl. Phys. A-Mater. Sci. Process. **75**, 641-645 (2002).
- [36] X. M. Ding, Y. Kawaguchi, T. Sato, A. Narazaki, R. Kurosaki and H. Niino: J. Photochem. Photobiol. A-Chem. **166**, 129-133 (2004).
- [37] X. M. Ding, T. Sato, Y. Kawaguchi and H. Niino: Jpn. J. Appl. Phys. Part 2 - Lett. **42**, L176-L178 (2003).
- [38] Y. Kawaguchi, X. Ding, A. Narazaki, T. Sato and H. Niino: Appl. Phys. A-Mater. Sci. Process. **79**, 883-885 (2004).
- [39] H. Niino, X. Ding, R. Kurosaki, A. Narazaki, T. Sato and Y. Kawaguchi, 742-742 (2003).
- [40] Y. Yasui, H. Niino, Y. Kawaguchi and A. Yabe: Appl. Surf. Sci. **186**, 552-555 (2002).
- [41] K. Zimmer, R. Böhme and B. Rauschenbach: Appl. Phys. A-Mater. Sci. Process. **79**, 1883-1885 (2004).
- [42] G. Kopitkovas, T. Lippert, C. David, A. Wokaun and J. Gobrecht: Thin Solid Films **453-54**, 31-35 (2004).
- [43] K. Zimmer, R. Böhme, A. Braun, B. Rauschenbach and F. Bigl: Appl. Phys. A-Mater. Sci. Process. **74**, 453-456 (2002).
- [44] C. Vass, B. Hopp, T. Smausz and F. Ignacz: Thin Solid Films **453-54**, 121-126 (2004).
- [45] R. Böhme and K. Zimmer: Appl. Surf. Sci. **239**, 109-116 (2004).
- [46] J. Wang, H. Niino and A. Yabe: Appl. Phys. A-Mater. Sci. Process. **69**, 271-273 (1999).
- [47] C. David, J. Wei, T. Lippert and A. Wokaun: Microelectron. Eng. **57-8**, 453-460 (2001).
- [48] H. Fukumura and H. Masuhara: Chem.Phys.Lett. **221**, 373-378 (1994).
- [49] Turo: Modern Molecular Photochemistry (The Benjamin/Cummings Publishing Company, Inc., Menlo Park, California, 1978).
- [50] J. B. Birks: Photophysics of Aromatic Molecules (Wiley-Interscience, London, UK, 1970).
- [51] S. D. Karpovic and J. G. Blanchard: J. Phys. Chem. **99**, 3951-3958 (1995).
-

- 
- [52] C. Bohne, E. B. Abuin and J. C. Scaiano: J. Am. Chem. Soc. **112**, 4226-4231 (1990).
- [53] P. Kubát and S. Civiš: Photolysis of pyrene by UV radiation, <http://www.photobiology.com/photobiology99/contrib/kubat/>.
- [54] H. Fujiwara, H. Fukumura and H. Masuhara: J. Phys. Chem. **99**, 11844-11853 (1995).
- [55] G. Kopitkovas, A. Chugreev, J. F. Nierengarten, Y. Rio, J. L. Rehspringer and B. Honerlage: Optical Materials **27**, 285-291 (2004).
- [56] A. Takamizawa, S. Kajimoto, J. Hobley, K. Hatanaka, K. Ohta and H. Fukumura: Phys. Chem. Chem. Phys. **5**, 888-895 (2003).
- [57] I. Ueno and M. Shoji: Journal of Heat Transfer **123**, 1123-1132 (2001).
- [58] D. Kim, M. Ye and C. P. Grigoropoulos: Appl. Phys. A **67**, 169-181 (1998).
- [59] J. M. Dowden: The Mathematics of Thermal Modeling (Chapman&Hall/CRC, Florida, US, 2001).
- [60] C. Vass, T. Smausz and B. Hopp: J. Phys. D-Appl. Phys. **37**, 2449-2454 (2004).
- [61] R. Böhme, D. Spemann and K. Zimmer: Thin Solid Films **453-54**, 127-132 (2004).
- [62] J. C. Isselin, A. P. Alloncle and M. Autric: J. Appl. Phys. **84**, 5766-5771 (1998).
- [63] W. P. Schiffers, S. J. Shaw and D. C. Emmony: Ultrasonics **36**, 559-563 (1998).
- [64] S. Siano, R. Pini, R. Salimbeni and M. Vannini: Appl. Phys. B **62**, 503-510 (1996).
- [65] W. O. Wray, T. Aida and R. B. Dyer: Appl. Phys. B **74**, 57-66 (2002).
- [66] A. Vogel, R. Engelhardt, U. Behnle and U. Parlitz: Appl. Phys. B **62**, 173-182 (1996).
- [67] Y. Kawaguchi, X. Ding, A. Narazaki, T. Sato and H. Niino: Appl. Phys. A-Mater. Sci. Process. **80**, 275-281 (2005).
- [68] R. C. Weast: CRC Handbook of Chemistry and Physics (CRC press, Washington DC, US, 1987).
- [69] I. Quest Consultants: Thermodynamic Properties Results, [http://quest1.questconsult.com/cgi-bin/parse\\_thermt](http://quest1.questconsult.com/cgi-bin/parse_thermt).
- [70] M. Hauer: Laser ablation of polymers studied by time resolved methods, Swiss Federal Institut of Technology Zürich, **PhD thesis** (2004).
-

- 
- [71] M. Hauer, D. J. Funk, T. Lippert and A. Wokaun: Optics and Laser Engineering **43**, 545-556 (2005).
- [72] X. Zhang, S. S. Chu, J. R. Ho and C. P. Grigoropoulos: Appl. Phys. A **64**, 545-552 (1997).
- [73] M. Lenzner, J. Kruger, W. Kautek and F. Krausz: Appl. Phys. A-Mater. Sci. Process. **69**, 465-466 (1999).
- [74] W. W. Duley: UV lasers: effects and applications in materials science (Press Syndicate of the University of Cambridge, Cambridge, UK, 1996).
- [75] A. V. Simakin, E. N. Lubnin and G. A. Shafeev: Quantum Electronics **30**, 263-267 (2000).
- [76] F. Raimondi, S. Abolhassani, R. Brutsch, F. Geiger, T. Lippert, J. Wambach, J. Wei and A. Wokaun: J. Appl. Phys. **88**, 3659-3666 (2000).
- [77] S. W. North, D. A. Blank, J. D. Gezelter, C. A. Longfellow and Y. T. Lee: J. Chem. Phys. **102**, 4447-4460 (1995).
- [78] P. J. Heaney, C. T. Prewitt and G. V. Gibbs: Silica: Physical Behavior, Geochemistry and Materials Applications (Department of Geological Sciences Virginia Polytechnic Institute & State University, Blacksburg, Virginia, US, 1994).
- [79] J. Finster, D. Schulze and A. Meisel: Surface Science **162**, 671-679 (1985).
- [80] F. J. Grunthaner, P. J. Grunthaner, R. P. Vasquez, B. F. Lewis, J. Maserjian and A. Madhukar: Phys. Rev. Lett **43**, 1683-1686 (1979).
- [81] M. H. Heise, L. Küpper, W. Pittermann and N. L. Butvina: Fresenius J Anal Chem **371**, 753-757 (2001).
- [82] J. Wong and A. C. Angell: Glass. Structure by Spectroscopy (Marcel Dekker, Inc., New York, US, 1976).
- [83] Y. Kawaguchi, A. Narazaki, T. Sato, H. Niino, A. Yabe, C. S. Langford and T. J. Dickinson: Appl. Surf. Scie. **197-198**, 50-55 (2002).
- [84] Wikipedia: Bremsstrahlung, <http://en.wikipedia.org/wiki/Bremsstrahlung>.
- [85] J. Wang, H. Niino and A. Yabe: Proc. SPIE **3933**, 64-69 (2000).
- [86] K. K. GmbH: Material Properties, <http://www.korth.de/eng/503728952d091450d/index.htm>.
- [87] M. T. Gale, M. Rossi, R. E. Kunz and G. L. Bona, 267-270 (1995).
-

- 
- [88] F. M. Dickey and S. C. Holswade: Laser beam shaping theory and techniques (Marcel Dekker, Inc., New York, USA, 2000).
- [89] S. W. Williams, P. J. Marsden, N. C. Roberts, J. Sidhu and M. A. Venables: Proc. SPIE **3343**, 205-211 (1998).
- [90] D. M. Brown: Proc. SPIE **4443**, 159-165 (2001).
- [91] M. W. Trott, E. R. Setchell, N. J. Castaneda and M. D. Berry: Proc. SPIE **4443**, 166-177 (2001).
- [92] Y. Kato, K. Mima, N. Miyanaga, S. Arinaga, Y. Kitagawa, M. Nakatsuka and C. Yamanaka: Phys. Rev. Lett. **53**, 1057-1060 (1984).
- [93] N. S. Dixit, M. I. Thomas, W. B. Woods, J. A. Morgan, A. M. Henesian, J. P. Wegner and T. H. Powell: Applied Optics **32**, 2543-2554 (1993).
- [94] C. L. S. Lewis, I. Weaver, L. A. Doyle, G. W. Martin, T. Morrow, D. A. Pepler, C. N. Danson and I. N. Ross: Rev. Sci. Instrum. **70**, 2116-2121 (1999).
- [95] A. H. Smith and R. O. Hunter: High power phase masks for imaging systems (1992).
- [96] A. H. Smith, R. O. Hunter and B. B. McArthur: High power masks and methods for manufacturing same (1994).
- [97] C. David and D. Hambach: Microelectron. Eng. **46**, 219-222 (1999).
- [98] C. Lin, Y. Hsiharng and C. Ching-Kong: J. Micromech. Microeng. **13**, 775-781 (2003).
- [99] G. Kopitkovas, T. Lippert, C. David, S. Canulescu, A. Wokaun and J. Gobrecht: J. Photochem. Photobiol. A-Chem. **166**, 135-140 (2004).
- [100] G. Kopitkovas, T. Lippert, C. David, R. Sulcas, J. Hobley, A. J. Wokaun and J. Gobrecht: Proc. SPIE **5662**, 515-525 (2004).
- [101] M. L. Ng, P. R. Herman, A. H. Nejadmalayeri and J. Li: Proc. SPIE **5339**, 127-133 (2004).
- [102] H. Niino, Y. Kawaguchi, T. Sato, A. Narazaki, T. Gumpenberger and R. Kurosaki: JLMN-Journal of Laser Micro/Nanoengineering **1**, 38-42 (2006).
-



## Curriculum Vitae

### Personal

Giedrius Kopitkovas,

born on the 7th of April, 1977 in Kaunas (Lithuania).

Citizen of Lithuania



### Education

2001-2005	<b>Paul Scherrer Institut Switzerland</b> <b>PhD. Student in the Materials Group at the Paul Scherrer Institut.</b> <b>Supervisors:</b> PD Dr. T. Lippert and Prof. A. Wokaun <b>Topics:</b> Fabrication and application of microoptical elements in UV-transparent materials, using UV-excimer and Nd:YAG lasers.
1999-2001	<b>Master degree in Physics at Vilnius University Faculty of Physics, Vilnius, Lithuania</b> <b>Studied subjects:</b> Solid state and semiconductors physics, Quantum electronics, Solid State lasers, Nonlinear effects in Semiconductors <b>Abroad Studies:</b> Student exchange program during 4 month at the Charles University in Prague, Czech Republic. Student exchange program (ERAZMUS) during 4 month in Material Research Institut in Strasbourg, France. <b>Master's Thesis:</b> "Study of Optical characteristics of Modified C <sub>60</sub> molecules inserted in porous SiO <sub>2</sub> glasses"
1995-1999	<b>Bachelor studies in Vilnius University Faculty of Physics, Vilnius, Lithuania</b> <b>Studied subjects:</b> Solid state and semiconductors physics, Basics in Inorganic and Organic Chemistry, basics in Law, courses of Teaching, Mathematic, Mechanical Physics, Electrodynamics, Physics of Particles, Nuclear Physics,

	Biophysics and Biochemistry. <b>Bachelor Diploma:</b> "Solar Elements with porous silicon: Study of surface recombination effect"
1983-1995	<b>Primary and Secondary School in Kaunas, Lithuania</b>

## List of Publications

2002	T. Lippert, J. T. Dickinson, M. Hauer, <u>G. Kopitkovas</u> , S. C. Langford, H. Masuhara, O. Nuyken, J. Robert, H. Salmio, T. Tada, K. Tomita, A. Wokaun, Polymers Designed for Laser Ablation-Influence of Photochemical Properties, invited paper, Appl. Surf. Sci. 197-198, 746 (2002).
2003	<u>G. Kopitkovas</u> , T. Lippert, C. David, A. Wokaun, J. Gobrecht, Fabrication of Microoptical Elements in Quartz by Laser Induced Backside Wet Etching, Microelectron. Eng. 67-68, 438 (2003).
2004	<u>G. Kopitkovas</u> , T. Lippert, C. David, A. Wokaun, J. Gobrecht, Surface Micromachining UV-transparent Materials, Thin Solid Films, 453-454, 31 (2004).
2004	<u>G. Kopitkovas</u> , S. Canulescu, C. David, J. Gobrecht, T. Lippert, A. Wokaun, Fabrication of micro-optical elements in UV-transparent materials, J. Photochem. Photobiol. A Chem. 166,

2005	<p>135 (2004).</p> <p><u>G. Kopitkovas</u>, T. Lippert, C. David, R. Sulcas, J. Hobley, A. Wokaun, J. Gobrecht, Laser micromachining of optical devices, SPIE Proceedings Vol. 5662, 515 (2004).</p> <p><u>G. Kopitkovas</u>, A. Chugreev, J.F. Nierengarten, Y. Rio, J.L. Rehspringer, B. Hönerlage, Reverse saturable absorption of fullerodendrimers in porous SiO<sub>2</sub> sol-gel matrices, Opt. Mat. 27, 285-291 (2004).</p> <p><u>G. Kopitkovas</u>, L.Urech, T. Lippert, Fabrication of Micro-optics in Polymers and in UV Transparent Materials, Recent advances in Laser Processing of Materials, ed. J. Parriere, E. Millon, E. Fogarassy, 105-135 (2005) (book chapter).</p> <p><u>G. Kopitkovas</u>, T. Lippert, J. Venturini, C. David, A. Wokaun, Laser Induced Backside Wet Etching: Mechanisms and Fabrication of Micro-optical elements, Journal of Physics: Conference Series, in press (2005).</p> <p><u>G. Kopitkovas</u>, T. Lippert, C. David, A. Wokaun, J. Gobrecht, Fast laser micromachining of micro-optics in quartz and BaF<sub>2</sub>, JLMN-Journal of Laser Micro/Nanoengineering 1, 23-27 (2006).</p> <p>J. Hobley, T. Oori, S. Kajimoto, K. Hatanaka, <u>G. Kopitkovas</u>, T. Lippert, H. Fukumura, Development of a nanosecond time resolved Brewster angle microscope to observe phase change at an interface, Colloids and Surfaces A: Physicochem. Eng. Aspect 284-285, 514 (2006).</p>
------	--

## **Attended conferences:**

### **Talks:**

G. Kopitkovas, C. David, T. Lippert, A. Wokaun

Fabrication of Micro-optical Elements in Quartz by Laser-Induced Backside Wet Etching  
MNE, 2002, 16-19.09.2002, Lugano, Switzerland

G. Kopitkovas, T. Lippert, C. David, A. Wokaun, J. Gobrecht

Laser micromachining: fabrication of optical elements in quartz  
CLEO Europe, 22-27.06.2003, Munich, Germany

### **Posters**

G. Kopitkovas, T. Lippert, C. David, J. Gobrecht, A. Wokaun

New concepts for a fabrication of microoptical elements in UV transparent optical materials

E-MRS, 10-13.06.2003, Strasbourg, France